

CLIMATE CHANGE AND ECOHYDROLOGICAL PROCESSES IN DRYLANDS:  
THE EFFECTS OF CO<sub>2</sub> ENRICHMENT, PRECIPITATION REGIME CHANGE AND  
TEMPERATURE EXTREMES

Xuefei Lu

Submitted to the faculty of the University Graduate School  
in partial fulfillment of the requirements  
for the degree  
Doctor of Philosophy  
in the Department of Earth Sciences,  
Indiana University

July 2018

Accepted by the Graduate Faculty of, Indiana University, in partial fulfillment of the requirements for the degree of Doctor of Philosophy.

Doctoral Committee

---

Lixin Wang, Ph. D., Chair

---

William P Gilhooly, Ph. D.

---

Pierre-André Jacinthe, Ph.D.

---

Lin Li, Ph. D.

April 3, 2018

---

Jeffery Wilson, Ph.D.

## **ACKNOWLEDGEMENTS**

First and foremost, I want to express my sincere appreciation and thanks to my advisor Dr. Lixin Wang for all the support he has given me in the course of my Ph.D. pursuit. He has been a tremendous mentor for me. His guidance and encouragement helped me in all the time of my research work and writing of this dissertation. I am very grateful for his patience, motivation, enthusiasm and immense knowledge that, taken together, make him a great researcher and mentor. I have been extremely lucky to have an advisor who cared so much about my work, and who responded to my questions and queries so promptly, and supported me academically and emotionally through the rough road to finish this dissertation.

I would also like to thank my committee members, Dr. Lin Li, Dr. William P Gilhooly, Dr. Pierre-André Jacinthe, and Dr. Jeffery Wilson, and my former committee Dr. Daniel Johnson, for all of their guidance through my Ph.D. pursuit. I greatly thank all my committee, for their contribution of time and extreme patience, for their intellectual guidance on my research work, especially for their insightful comments and suggestions on writing of my dissertation.

My sincere thank goes to Department of Earth Sciences, to all the graduates, undergraduates, faculty and staff members in the Earth Sciences. I am especially grateful to all the group members from Dr. Lixin Wang's lab. The group has been a source of friendships as well as good advice and collaboration. I would especially like to thank Farai for his dedication on the field data collection in Namibia, and I have so enjoyed those valuable discussions with Farai in everyday life and academia.

I wish to thank all my collaborators, Dr. Matthew F. McCabe from King Abdullah University of Science and Technology, Dr. Xianzhong Wang from IUPUI, Dr. Ming Pan from Princeton University, Dr. Liyin Liang from University of Waikato, Dr. Darrel Jenerette and Dr. David A. Grantz from University of California, Riverside. This work was made possible thanks to U.S. National Science Foundation (IIA-1427642), Indiana University-Purdue University Indianapolis (IUPUI) iM2CS-GEIRE program, the National Science Foundation Division of Earth Sciences (EAR-1554894) and U.S. Department of Agriculture (USDA) National Institute of Food and Agriculture (NIFA) Agriculture and Food Research Initiative (AFRI) program (2017-67013-26191).

Special thanks go to my family. Words cannot express how grateful I am to my family members, my dear mom and dad, and especially my husband Xi Zhang, for being my biggest support over the years. Without their encouragement and support, I would not be able to complete my Ph.D. degree. To my beloved daughter Audrey, thank you for being such a great girl always cheering me up.

Xuefei Lu

CLIMATE CHANGE AND ECOHYDROLOGICAL PROCESSES IN DRYLANDS:  
THE EFFECTS OF CO<sub>2</sub> ENRICHMENT, PRECIPITATION REGIME CHANGE AND  
TEMPERATURE EXTREMES

Drylands are the largest terrestrial biome on the planet, and the critically important systems that produce approximately 40% of global net primary productivity to support nearly 2.5 billion of global population. Climate change, increasing populations and resulting anthropogenic effects are all expected to impact dryland regions over the coming decades. Considering that approximately 90% of the more than 2 billion people living in drylands are geographically located within developing countries, improved understanding of these systems is an international imperative. Although considerable progress has been made in recent years in understanding climate change impacts on hydrological cycles, there are still a large number of knowledge gaps in the field of dryland ecohydrology. These knowledge gaps largely hinder our capability to better understand and predict how climate change will affect the hydrological cycles and consequently the soil-vegetation interactions in drylands.

The present study used recent technical advances in remote sensing and stable isotopes, and filled some important knowledge gaps in the understanding of the dryland systems. My study presents a novel application of the combined use of customized chambers and a laser-based isotope analyzer to directly quantify isotopic signatures of

transpiration (T), evaporation (E) and evapotranspiration (ET) *in situ* and examine ET partitioning over a field of forage sorghum under extreme environmental conditions. We have developed a useful framework of using satellite data and trend analysis to facilitate the understanding of temporal and spatial rainfall variations in the areas of Africa where the *in situ* observations are scarce. By using a meta-analysis approach, we have also illustrated that higher concentrations of atmospheric CO<sub>2</sub> induce plant water saving and the consequent available soil water increases are a likely driver of the observed greening phenomena. We have further demonstrated that Leuning's modified Ball-Berry model and RuBP limited optimization model can generally provide a good estimate of stomatal conductance response to CO<sub>2</sub> enrichment under different environmental conditions. All these findings provide important insights into dryland water-soil-vegetation interactions.

Lixin Wang, Ph. D., Chair

## TABLE OF CONTENTS

<b>LIST OF TABLES</b> .....	xi
<b>LIST OF FIGURES</b> .....	xii
<b>CHAPTER 1: INTRODUCTION</b> .....	1
References.....	7
<b>CHAPTER 2: IS ELEVATED CO<sub>2</sub> A DRIVER OF GLOBAL DRYLAND GREENING?</b> .....	10
2.1 Abstract .....	10
2.2 Introduction .....	11
2.3 Methods.....	14
2.4 Results and discussion.....	17
2.5 Conclusions .....	21
References.....	28
<b>CHAPTER 3: EVALUATION AND DEVELOPMENT OF ECOHYDROLOGICAL MODELING FRAMEWORK TO LINK ATMOSPHERIC CO<sub>2</sub>, STOMATAL CONDUCTANCE RESPONSE, AND ROOT-ZONE SOIL MOISTURE DYNAMICS</b> .....	32
3.1 Abstract .....	32
3.2 Introduction .....	34
3.3 Methods.....	38
3.3.1 Model formulation.....	38

3.3.2 Testing data sets .....	41
3.3.3 Parameter sensitivity analysis .....	43
3.4 Results and discussion .....	44
3.4.1 Sensitivity analysis .....	44
3.4.2 Evaluation of model performance under different environmental conditions ...	45
3.4.3 Evaluation of model performance under environmental different conditions for dryland data .....	49
3.4.4 Development of a modeling framework to link $g_s$ and soil water content .....	50
3.5 Conclusions .....	52
References.....	63

**CHAPTER 4: A MULTI-SCALE ANALYSIS OF NAMIBIAN RAINFALL  
OVER THE RECENT DECADE – COMPARING TMPA SATELLITE**

<b>ESTIMATES AND GROUND OBSERVATIONS .....</b>	<b>69</b>
4.1 Abstract .....	69
4.2 Introduction .....	70
4.3 Methods.....	74
4.4 Results and discussion.....	77
4.4.1 TMPA data validation using two ground gauges .....	77
4.4.2 Mann-Kendall trend analysis .....	80
4.4.3 Rainfall seasonality and erratic rain pattern with extreme rainfall events and droughts .....	82



4.5 Conclusions .....	83
References.....	94
<b>CHAPTER 5: PARTITIONING OF EVAPOTRANSPIRATION USING A STABLE ISOTOPE TECHNIQUE IN AN ARID AND HIGH TEMPERATURE AGRICULTURAL PRODUCTION SYSTEM.....</b>	<b>98</b>
5.1 Abstract .....	98
5.2 Introduction .....	100
5.3 Materials and methods.....	103
5.3.1 Study site.....	103
5.3.2 Isotope-based partitioning.....	105
5.3.3 Total ET measurements.....	107
5.4 Results.....	107
5.5 Discussion .....	109
5.6 Conclusions .....	113
References.....	122
<b>CHAPTER 6: CONCLUSIONS AND FUTURE WORK.....</b>	<b>127</b>
6.1 Conclusions .....	127
6.2 Suggestions for Future Work .....	130
<b>APPENDICES.....</b>	<b>132</b>
Appendix A: Summary of soil water content data under CO <sub>2</sub> enhancement study .....	132
Appendix B: Summary of stomatal conductance data under environment	

different conditions .....	135
Appendix C: Stomatal conductance and soil water model framework .....	150
Appendix D: TMPA satellite rainfall estimates for the 4 locations across a rainfall gradient in Namibia .....	152
Appendix E: Deuterium and oxygen isotope signatures for transpiration (T), evaporation (E) and evapotranspiration (ET) over 3 irrigation cycles for Sorghum bicolor at the University of California’s Desert Research and Extension Center (DREC) .....	161

**CURRICULUM VITAE**

## LIST OF TABLES

**Table 3.1** Model sensitivity of key parameters for Leuning's modified Ball-Berry model, RuBP limited optimization model, and Rubisco limited optimization model. ....53

**Table 5.1** Evapotranspiration partitioning calculations at representative sampling dates. .... 115

## LIST OF FIGURES

<b>Figure 1.1</b> Conceptual framework for this dissertation .....	6
<b>Figure 2.1</b> Global climate map and a comparison of mean effect size and soil water response under elevated CO <sub>2</sub> . A. Site locations of the CO <sub>2</sub> enrichment experiments together with globally distributed climate zones based on a standard aridity index formulation (precipitation/potential evapotranspiration); B. Mean effect size of soil water content under elevated CO <sub>2</sub> for the entire data set, under dryland and non-dryland regimes. The effect size was calculated as the natural log of the magnitude of an experimental treatment mean (the soil water under elevated CO <sub>2</sub> ) relative to the control treatment mean (the soil water under ambient CO <sub>2</sub> ); C. Enhancement of soil water content under elevated CO <sub>2</sub> for dryland versus non-dryland regimes. The number of cases is shown in brackets. Error bars are bootstrapped confidence intervals (CI). All the statistics are significant at $P < 0.05$ . The map was generated using ArcGIS for Desktop 10.3.1 ( <a href="http://www.arcgis.com">http://www.arcgis.com</a> ). .....	24
<b>Figure 2.2</b> Structural equation modeling of direct and indirect effects of CO <sub>2</sub> enrichment on vegetation productivity for both drylands and non-drylands. The number of cases is shown in brackets. Arrow thickness is proportional to path coefficient. ....	25
<b>Figure 2.3</b> Enhancement of soil water content for elevated CO <sub>2</sub> levels (A) under different management systems; B) under different vegetation types; and (C) under different soil texture; and (D) using results from different soil water content (SWC) measurement methods (volumetric method, gravimetric method, etc. The number of cases is shown in brackets. Error bars are bootstrapped confidence intervals (CI). All the statistics are significant at $P < 0.05$ . ....	26
<b>Figure 2.4</b> Sensitivity of the soil water response to CO <sub>2</sub> enrichment for the entire data set. The response index was calculated as the soil water content under elevated CO <sub>2</sub> divided by the soil water content under ambient CO <sub>2</sub> . The closed circles are the observations, with the solid black line providing a linear regression. The red lines represent the 95% confidence intervals of the observations and the dashed grey lines represent the 95% confidence interval of the model. $m$ is the slope of the regression line. ....	27
<b>Figure 3.1</b> Instantaneous measurements of stomatal conductance $g_s$ as a function of $C_a$ , $A$ , and $D$ for the Leuning's modified Ball-Berry model (red open circles), RuBP limited optimization model (grey open squares), and Rubisco limited optimization model (blue open triangles), with $C_a$ ranging between 200 and 1000 ppm. ....	54

<b>Figure 3.2</b> Semi-controlled measurements of stomatal conductance $g_s$ as a function of $C_a$ , $A$ , and $D$ for the Leuning's modified Ball-Berry model (red open circles), RuBP limited optimization model (grey open squares), and Rubisco limited optimization model (blue open triangles).....	55
<b>Figure 3.3</b> The response of stomatal conductance $g_s$ as a function of $C_a$ , $A$ , and $D$ for two functional groups ( $C_3$ plant vs. $C_4$ plant), for the Leuning's modified Ball-Berry model (A), RuBP limited optimization model (B), and Rubisco limited optimization model (C). The data are from semi-controlled measurements. ....	56
<b>Figure 3.4</b> The responses of stomatal conductance $g_s$ as a function of $C_a$ , $A$ , and $D$ for different life forms (annual vs. perennial plant), for the Leuning's modified Ball-Berry model (A), RuBP limited optimization model (B), and Rubisco limited optimization model (C). The data are from semi-controlled measurements. ....	57
<b>Figure 3.5</b> The response of stomatal conductance $g_s$ as a function of $C_a$ and $A$ for the Leuning's modified Ball-Berry model (A), RuBP limited optimization model (B), and Rubisco limited optimization model (C). The data are from FACE measurements. ...	58
<b>Figure 3.6</b> The response of stomatal conductance $g_s$ as a function of $C_a$ and $A$ for different functional groups, for the Leuning's modified Ball-Berry model (A), RuBP limited optimization model (B), and Rubisco limited optimization model (C). The data are from FACE measurements.....	59
<b>Figure 3.7</b> The response of stomatal conductance $g_s$ as a function of $C_a$ and $A$ for different life forms (annual vs. perennial plant), for the Leuning's modified Ball-Berry model (A), RuBP limited optimization model (B), and Rubisco limited optimization model (C). The data are from FACE measurements .....	60
<b>Figure 3.8</b> Regression of stomatal conductance $g_s$ as a function of $C_a$ , $A$ , and $D$ for the Leuning's modified Ball-Berry model (red open circles), RuBP limited optimization model (grey open squares), and Rubisco limited optimization model (blue open triangles). The data are from semi-controlled measurements in drylands.....	61
<b>Figure 3.9</b> The responses of stomatal conductance $g_s$ as a function of $C_a$ , $A$ , and $D$ for different species and life form, for Leuning's modified Ball-Berry model (A), RuBP limited optimization model (B), and Rubisco limited optimization model (C). The data are from semi-controlled measurements in drylands.....	62
<b>Figure 4.1</b> Locations of the Weltevrede Farm (Farm 1 and Farm 2), Gobabeb Research and Training Center (GRTC), Windhoek (WDH) and the surface rain	

gauges. Black lines indicate the boundary of the Weltevrede Farm. The map was generated using ArcGIS for Desktop 10.3.1 (<http://www.arcgis.com>). .....85

**Figure 4.2** Data validation of Tropical Rainfall Measuring Mission Multi-satellite Precipitation Analysis (TMPA) data set. Scatter plots of daily (a) (n = 2192), monthly (b) (n = 72), and annual (c) (n = 6) rainfall from TMPA and gauged estimates at Farm 1 (Top Panel) and Farm 2 (Bottom Panel) for the period of January 1, 2008 to December 31, 2013.  $m$  is the slope coefficient. ....86

**Figure 4.3** Cumulative distribution functions (CDFs) of daily (a), monthly (b), and annual (c) rainfall from Tropical Rainfall Measuring Mission Multi-satellite Precipitation Analysis (TMPA) and gauged estimates at Farm 1 (Top Panel) and Farm 2 (Bottom Panel) for the period of January 1, 2008 to December 31, 2013. ....87

**Figure 4.4** Time series of annual rainfall (mm), average rain depth per storm (mm)  $\alpha$ , and the average storm arrival rate ( $\text{day}^{-1}$ )  $\lambda$  for (a) Windhoek (WDH), (b) Weltevrede Farm Location 1 (Farm 1), (c) Weltevrede Farm Location 2 (Farm 2), and (d) Gobabeb Research and Training Center (GRTC). Record length = 17 years, and  $m$  = Sen's slope. ....88

**Figure 4.5** Time series of seasonal precipitation (mm), the average rain depth per storm (mm)  $\alpha$ , and the average storm frequency ( $\text{day}^{-1}$ )  $\lambda$  for (a) Windhoek (WDH), (b) Weltevrede Farm Location 1 (Farm 1), (c) Weltevrede Farm Location 2 (Farm 2), and (d) Gobabeb Research and Training Center (GRTC). Rainy season is from October to April, record length = 17 years, and  $m$  = Sen's slope. ....89

**Figure 4.6** Time series of standard deviation, coefficient of variance (CV), and precipitation variability index (PVI) of annual rainfall (mm) for (a) Windhoek (WDH), (b) Weltevrede Farm Location 1 (Farm 1), (c) Weltevrede Farm Location 2 (Farm 2), and (d) Gobabeb Research and Training Center (GRTC). Record length = 17 years, and  $m$  = Sen's slope. ....90

**Figure 4.7** Seasonality of annual precipitation (mm) for (a) Windhoek (WDH), (b) Weltevrede Farm Location 1 (Farm 1), (c) Weltevrede Farm Location 2 (Farm 2), and (d) Gobabeb Research and Training Center (GRTC). Median represented by dark solid line, box represents the 1st and 3<sup>rd</sup> quartile range. The boxes are drawn with widths proportional to the square roots of the number of observations in the groups. The whiskers extend to the most extreme data point which is no more than two times the inter quartile range from the box. Circles represent outliers. ....91

<b>Figure 4.8</b> Time series of late summer (February-March-April) precipitation (mm) for (a) Windhoek (WDH), (b) Weltevrede Farm Location 1 (Farm 1), (c) Weltevrede Farm Location 2 (Farm 2), and (d) Gobabeb Research and Training Center (GRTC). Record length = 17 years, and $m$ = Sen's slope.....	92
<b>Figure 4.9</b> Cumulative Distribution Functions (CDFs) of daily (a), monthly (b), and annual (c) precipitation from gauged estimates at Farm 2 and TMPA data at Farm 1 for period of January 1, 2008 to December 31, 2013. ....	93
<b>Figure 5.1</b> Location of the University of California Desert Research and Extension Center (DREC). Monthly mean precipitation (mm), reference evapotranspiration ( $ET_o$ ) (mm), temperature and relative humidity over 1990 – 2015 for the Meloland station of the California Irrigation Management Information System (CIMIS), located within a few hundred meters of the experimental field. ....	116
<b>Figure 5.2</b> The $\delta D$ - $\delta^{18}O$ relationships of leaf transpiration ( $\delta_T$ , blue circles) and soil evaporation ( $\delta_E$ , red circles). Black circles depict the measured isotopic composition of the irrigation water. The dashed black line is the Local Meteoric Water Line, determined via least-squares fitting of the irrigated water isotope values. The solid gray line is the Global Meteoric Water Line (GMWL). VSMOW is Vienna Standard Mean Ocean Water.....	117
<b>Figure 5.3</b> Patterns of deuterium and oxygen isotope signatures for transpiration (T), evaporation (E) and evapotranspiration (ET) over the irrigation cycles. (a) observed pattern for deuterium ( $\delta D$ ), (b) observed pattern for oxygen ( $\delta^{18}O$ ). VSMOW stands for a standard of Vienna Standard Mean Ocean Water.....	118
<b>Figure 5.4</b> Daily variation of transpiration (T) and evapotranspiration (ET) during the vegetative stage, calculated by combing isotope partitioning and total ET results obtained from concurrent eddy covariance measurements. ....	119
<b>Figure 5.5</b> Variations of leaf area index (LAI) during crop development (a) and the relationship between T/ET and LAI (b). ....	120
<b>Figure 5.6</b> Comparison of deuterium isotope signature of leaf transpiration ( $\delta_T$ ) and soil evaporation ( $\delta_E$ ) over the measurement period. VSMOW stands for a standard of Vienna Standard Mean Ocean Water.....	121

## CHAPTER 1: INTRODUCTION

Drylands regions, defined broadly as zones where mean annual precipitation is less than two-third of potential evaporation, are critically important systems (D’Odorico et al., 2013; Eldridge et al., 2011; Wang et al., 2012; Wang et al., 2017) and represent the largest terrestrial biome on the planet (Schimel, 2010). Drylands cover about 41% of the global land surface (Millennium Ecosystem Assessment, 2005), support a population of nearly 2.5 billion (Gilbert, 2011), and account for as much as 40% of global net primary productivity (Grace, 2006). Given the pressures of climate change, population growth that are expected to impact dryland regions over the coming decades (Millennium Ecosystem Assessment, 2005), especially as around 90% of dryland populations are geographically located within developing countries (Wang et al., 2012), a better understanding of these systems is becoming an international imperative.

Many drylands around the world are affected by “desertification”, i.e., land degradation in arid, semi-arid and dry sub-humid areas resulting from various reasons including climatic variations and human activities (UNCCD, 1994). It has been estimated that up to 70% of the world’s drylands (excluding those in hyper-arid deserts) suffer from degradation (Dregne, 2002). Evidence has also shown that changing climate conditions have resulted in the intensification of hydrologic cycles, leading to changes in water-resource availability, increase in the frequency and intensity of climate extremes such as floods and droughts, and amplification of warming through the water vapor feedback (Huntington, 2006). The disruptions to hydrological cycles has more severe



consequences on drylands since they result in less rainfall, yet more erratic rainfall events, as well as extreme heat and aridity that exacerbate the already critical state of water scarcity.

Enhanced atmospheric CO<sub>2</sub>, temperature extremes, and changes in precipitation are three of the most critical factors determining the impact of climate change on the dynamics of water and vegetation in drylands. Generally, warmer temperatures tend to intensify the water stress through increased evapotranspiration, but the increase in atmospheric CO<sub>2</sub> could partially mitigate these effects by accelerating the photosynthetic rates of plants or enhancing the water use efficiency (Tietjen et al., 2010). Changes in precipitation show that drylands are facing decreases in mean annual precipitation, with less frequency of precipitation events, but more extreme events (Dore, 2005; Easterling et al., 2000). However, climate change impacts could vary substantially from region to region because of the differences in geographical characteristics and local climate (Naz et al., 2016); thus the ecohydrological responses to climate changes are region-specific and the scale of observation is an important factor to consider in understanding and predicting climate change impacts (Wang et al., 2012).

Considerable progress has been made in recent years in understanding climate change impacts on hydrological cycles, especially with the establishment of Intergovernmental Panel on Climate Change (IPCC). There are a number of exciting developments in monitoring tools used for the climate change studies, particularly, the recent development of techniques using remote sensing and stable isotopes has provided

useful tools to characterize the water budget at various scales. Remote sensing has the advantage in temporal and spatial duration and stable isotopes have the advantage in detecting mechanisms (Wang et al., 2012). Through the remote sensing platforms, data could be extrapolated across the spatial and temporal domain, which therefore extends the point scale focus of many ecohydrological investigations to larger spatial extents, and offers insight into pattern change and development through time (Wang et al., 2012). Evapotranspiration (ET) loss can reach up to 95% in some dryland systems (Wang et al., 2014; Wilcox and Thurow, 2006) and the development of techniques using stable isotopes of water provides a useful tool to separate evaporation (E) and transpiration (T) that can be applied across broad spatial and temporal scales. Besides facilitating ET partitioning, the stable isotopic composition of E and T can also provide insights regarding plant water use dynamics as well as the nature of land-atmosphere interactions (Parkes et al., 2017). This study uses remote sensing and stable isotopes of water to assist in addressing some critical issues in the understanding of dryland ecohydrology.

Despite these recent developments, there are still a large number of knowledge gaps in the field of dryland ecohydrology, which hinder our ability to understand and predict the effects of climate change on hydrological cycles and soil-vegetation interaction in drylands. My dissertation research aims to resolve some important knowledge gaps related to the effect of CO<sub>2</sub> enhancement, changes in precipitation and temperature extremes on soil and vegetation hydrological conditions in dryland systems

(Figure 1.1), using advanced techniques of remote sensing and stable isotopes.

Specifically, my study addresses the following questions:

- ✚ In contrast to growing desertification and declining vegetation productivity in drylands, recent findings based on remote sensing data have suggested a trend of increasing vegetation greening in global drylands. What are the drivers behind the observed greening response, and what are the processes and mechanisms by which these drivers could cause the greening?
- ✚ Stomatal conductance ( $g_s$ ) is key to understanding plant-water-atmosphere interactions, and the response of vegetation to climate-induced water stress. Although there are  $g_s$  models with different levels of complexity, the establishment of an accurate stomatal conductance model under diverse environmental conditions remains an important research goal and no previous studies have attempted to evaluate different  $g_s$  models under diverse conditions. This study, by using field data from different environmental conditions, aims to find out how well do the  $g_s$  models perform under diverse conditions.
- ✚ IPCC has predicted a likely decrease in late summer rainfall over southern Africa; however, this prediction was run at a coarse spatial resolution while the rainfall process has a much higher spatial variability. With the valuable ground-based observations, can we develop an approach to evaluate the ecohydrological processes in extreme data scarcity regions through trend analysis with Multi-satellite Precipitation Analysis (TMPA) data?

✚ Extreme heat and aridity caused by high temperature and drought has put more stringent pressure on the already limited water resources in some dryland regions. Can we use stable isotope techniques to determine how much and to what extent irrigated water is transpired by crops relative to being lost through evaporation in such an unusually harsh production environment?

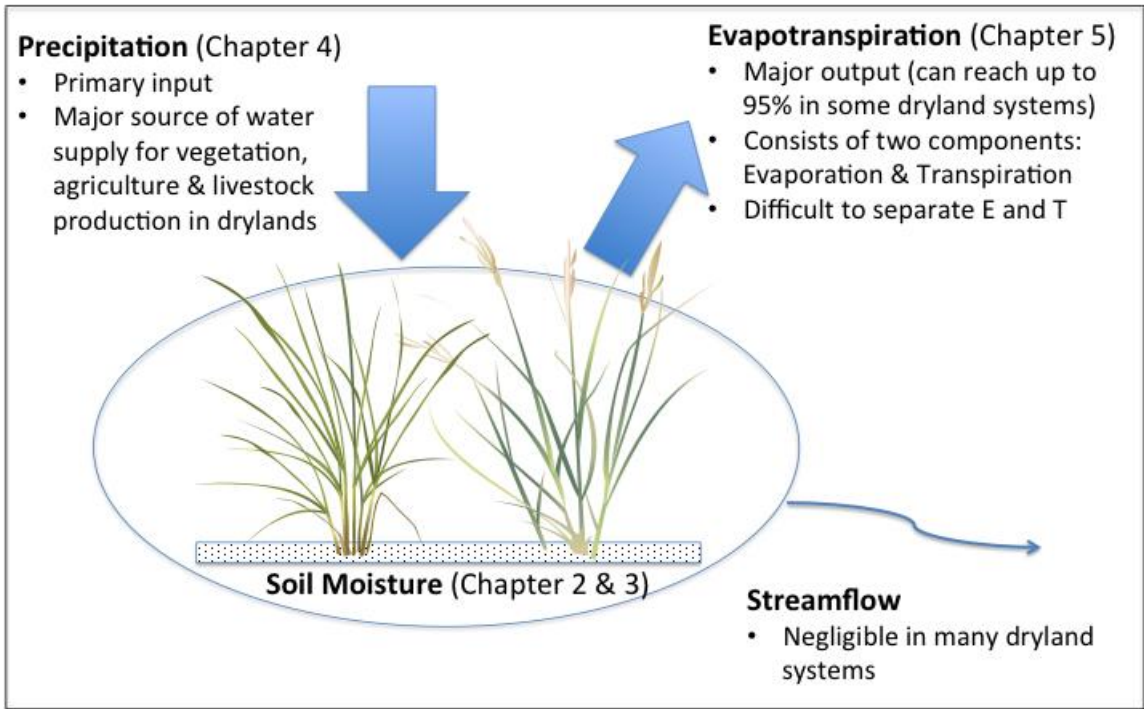


**Figure 1.1** Conceptual framework for this dissertation.

## References

- D'Odorico, P., Bhattachan, A., Davis, K.F., Ravi, S., Runyan, C.W., 2013. Global desertification: drivers and feedbacks. *Advances in Water Resources*, 51: 326-344.
- Dore, M.H., 2005. Climate change and changes in global precipitation patterns: what do we know? *Environment International*, 31(8): 1167-1181.
- Dregne, H.E., 2002. Land degradation in the drylands. *Arid Land Research and Management*, 16(2): 99-132.
- Easterling, D.R., Meehl, G.A., Parmesan, C., Changnon, S.A., Karl, T.R., Mearns, L.O., 2000. Climate extremes: observations, modeling, and impacts. *Science*, 289(5487): 2068-2074.
- Eldridge, D.J., Bowker, M.A., Maestre, F.T., Roger, E., Reynolds, J.F., Whitford, W.G., 2011. Impacts of shrub encroachment on ecosystem structure and functioning: towards a global synthesis. *Ecology Letters*, 14(7): 709-722.
- Gilbert, N., 2011. United Nations considers creating advisory panel on land degradation akin to IPCC. *Nature*, 477: 262-264, doi:10.1038/477262a.
- Grace, J.B., 2006. *Structural equation modeling and natural systems*. Cambridge University Press.
- Huntington, T.G., 2006. Evidence for intensification of the global water cycle: review and synthesis. *Journal of Hydrology*, 319(1): 83-95.
- Millennium Ecosystem Assessment, 2005. *Ecosystems and human well-being: desertification synthesis*. World Resources Institute, Washington, DC.

- Naz, B.S., Kao, S.C., Ashfaq, M., Rastogi, D., Mei, R., Bowling, L.C., 2016. Regional hydrologic response to climate change in the conterminous United States using high-resolution hydroclimate simulations. *Global and Planetary Change*, 143: 100-117.
- Parkes, S.D., McCabe, M.F., Griffiths, A.D., Wang, L., Chambers, S., Ershadi, A., 2017. Response of water vapour D-excess to land-atmosphere interactions in a semi-arid environment. *Hydrology and Earth System Sciences*, 21(1): 533-548.
- Schimel, D.S., 2010. Drylands in the Earth System. *Science*, 327(5964): 418-419.
- Tietjen, B., Jeltsch, F., Zehe, E., Classen, N., Groengroeft, A., Schiffers, K., Oldeland, J., 2010. Effects of climate change on the coupled dynamics of water and vegetation in drylands. *Ecohydrology*, 3(2): 226-237.
- UNCCD, 1994. United Nations Convention to Combat Desertification, Elaboration of an International Convention to Combat Desertification in Countries Experiencing Serious Drought and/or Desertification, Particularly in Africa U.N. Doc. A/AC.241/27, 33 I.L.M. 1328.
- Wang, L., D'Odorico, P., Evans, J., Eldridge, D., McCabe, M., Caylor, K., King, E., 2012. Dryland ecohydrology and climate change: critical issues and technical advances. *Hydrology and Earth System Sciences*, 16: 2585-2603.
- Wang, L., Good, S.P., Caylor, K.K., 2014. Global synthesis of vegetation control on evapotranspiration partitioning. *Geophysical Research Letters*, 41: 6753–6757.

Wang, L., Kaseke, K.F., Seely, M., 2017. The effects of non-rainfall water inputs on ecosystem functions. *Wiley Interdisciplinary Reviews: Water*, 30(19): 2077–2086.

Wilcox, B.P., Thurow, T.L., 2006. Emerging issues in rangeland ecohydrology: vegetation change and the water cycle. *Rangeland Ecology & Management*, 59: 220–224.



## CHAPTER 2: IS ELEVATED CO<sub>2</sub> A DRIVER OF GLOBAL DRYLAND GREENING?

### 2.1 Abstract

Recent findings based on satellite records have indicated there is a positive trend in vegetation greenness over global drylands. However, the reasons behind the observed greening trend remain elusive. We hypothesize that enhanced levels of atmospheric CO<sub>2</sub> are responsible for the observed greening through a CO<sub>2</sub> driven impact on plant water savings and consequent available soil water increases. In this study, we used meta-analytic techniques to compare the soil water content under ambient and elevated CO<sub>2</sub> treatments across different climate regimes, vegetation types, soil textures and land management practices. Based on 1705 field measurements from 21 distinct sites, we observed a consistent and statistically significant increase (11%) in soil water under elevated CO<sub>2</sub> treatments in both drylands and non-drylands. More importantly, drylands showed a statistically stronger response over non-drylands (17% vs. 9%). Given the inherent water limitation in drylands, we suggested that the additional soil water availability is likely driving observed increases in vegetation greenness.

## **2.2 Introduction**

Defined broadly as zones where mean annual precipitation is less than two-third of potential evaporation, drylands are critically important systems (D’Odorico et al., 2012; Eldridge et al., 2011; Wang et al., 2012) and represent the largest terrestrial biome on the planet (Schimel, 2010). Climate change, increasing populations and resulting anthropogenic effects are all expected to impact dryland regions over the coming decades (Millennium Ecosystem Assessment, 2005). Considering that approximately 90% of the more than 2 billion people living in drylands (Gilbert, 2011) are geographically located within developing countries (Wang et al., 2012), improved understanding of these systems is an international imperative. Recent regional scale analyses using satellite based vegetation indices such as the Normalized Difference Vegetation Index (NDVI), have found extensive areas of “greening” in dryland areas of the Mediterranean (Osborne and Woodward, 2001), the Sahel (Herrmann et al., 2005), the Middle East (Nielsen and Adriansen, 2005) and Northern China (Runnström, 2000), as well as greening trends in Mongolia and South America (Hellden and Tottrup, 2008). More recently, a global synthesis over the period from 1982-2007 that used an integrated NDVI and annual rainfall, showed an overall “greening-up” trend over the Sahel belt, Mediterranean basin, China-Mongolia region and the drylands of South America (Fensholt et al., 2012).

To better predict system responses to possible climate changes, it is necessary to understand the drivers behind the observed greening response. Several mechanisms may contribute to the apparent trends in vegetation greenness. For example, increased rainfall

is one obvious driver of change, with a number of studies establishing a positive relationship between NDVI and precipitation (Fensholt et al., 2012; Herrmann et al., 2005). However, rainfall does not explain the observed trends at a global scale. Indeed, there are regions where greening occurs in the absence of any observed rainfall increases (Fensholt et al., 2012). Likewise, there are areas where a significant rainfall increase occurs without a corresponding change in greening (Fensholt et al., 2012). In addition, even in those regions experiencing concurrent greening and rainfall increase (such as in the African Sahel), removing the effects of rainfall from the NDVI time series does not completely remove the NDVI residual, indicating that the vegetation greening in the Sahel may be attributable to additional factors (Herrmann et al., 2005). Changes in land use or the implementation of improved management practices may also impact vegetation in certain areas, such as the observed agricultural expansions in Australia's Murray-Darling basin, the Middle East, the southwest United States, tree plantations in west China (Liu et al., 2015), as well as grazing practices triggering changes in plant community composition in South Africa. Greening can also result from variations in species composition (e.g., exotic species invasion in many drylands (Herrmann and Tappan, 2013)). However, similar to rainfall changes, human-induced factors and compositional changes in vegetation communities are more likely to be an important local driver impacting vegetation response. As vegetation greening has been observed across all drylands, discriminating the influence of a potential global driver that is enhanced or suppressed by local scale factors, is one of the goals of this work.

To this end, we hypothesize that higher levels of atmospheric CO<sub>2</sub> concentration are a key driver of the observed dryland greening, through an impact on plant water savings and consequent available soil water increase. A novel modeling framework introduced by Donohue et al. (2013), described higher vegetation water use efficiency (*WUE*) under CO<sub>2</sub> enrichment, with the authors using this mechanism to explain increases in maximum vegetation cover in warm and dry environments. The hypothesis developed in this study implies that the greening in global drylands is a response to higher atmospheric CO<sub>2</sub> levels and resulting increase in soil water availability. The hypothesis is based on increasing atmospheric CO<sub>2</sub> inducing decreases in plant stomatal conductance and enhancing vegetation *WUE* (Donohue et al., 2013; Farquhar et al., 1989). Higher *WUE* encourages increased soil water under the same productivity levels. Since soil water is a limiting factor in dryland vegetation growth and function (Rodriguez-Iturbe and Porporato, 2004), any increase in available soil water is expected to enhance plant growth and greening.

Here, we attempt to examine this hypothesis using a data driven meta-analytic approach. One of the key aims of this work is not just to identify the potential contribution of CO<sub>2</sub> to observed changes in global greening, but also to identify different soil water responses that might be occurring within dryland and non-dryland systems. Understanding the varying interactions between soil water and vegetation under CO<sub>2</sub> enrichment between dryland and non-dryland systems would significantly increase our

capacity to predict vegetation response to future climatic changes, as dynamic vegetation responses often pose large uncertainties in global models.

### **2.3 Methods**

Our study is based on an analysis of data obtained from field experiments in which changes in soil water were measured under elevated atmospheric CO<sub>2</sub> concentrations using a Free-Air CO<sub>2</sub> Enrichment (FACE) facility or open top chamber. To collect the data required in the meta-analysis, a comprehensive literature search using the terms ‘CO<sub>2</sub> enrichment’, ‘soil moisture’, ‘FACE’, ‘open top chamber’ and ‘growth chamber’ was conducted across Thomson Reuters Web of Science and Google Scholar databases. All of the field data used in this study was derived from *in-situ* field experiments that examined soil water responses to both ambient and elevated atmospheric CO<sub>2</sub> levels.

A rigorous procedure was employed to ensure the independence of each data entry, avoiding over-representation of any particular study and reducing publication bias. For instance, in cases where data were collected over consecutive years, but using identical treatments with the same soil texture and vegetation cover, data were averaged and only a single entry from that study was used in the meta-analysis. In cases where different types of vegetation cover or soil texture were used, or where the same experiment was carried out under different treatments (e.g., nitrogen addition vs. control), data were treated as separate contributions. When soil water content was measured at multiple depths, only the top 0-25 cm measurements were used in the meta-analysis. We focus on soil water

content from the growing season only, since this is the period with the closest interaction between vegetation and soil water. A summary of the soil water content data under different CO<sub>2</sub> enhancement studies was provided in Appendix A.

The Meta-Win 2.0 software (Rosenberg et al., 2000) was used to perform statistical analysis on results. In order to include those studies that did not adequately report sample sizes or standard deviations, we conducted an unweighted analysis using the log response ratio ( $\ln R$ ) to calculate bootstrapped confidence limits (Rosenberg et al., 2000). Elevated CO<sub>2</sub> was considered to have a significant effect on soil water content if the bootstrap confidence interval did not overlap with zero (Rosenberg et al., 2000). The CO<sub>2</sub> response of two groups was considered significantly different if their bootstrap confident intervals did not overlap. A statistical significance level of  $P < 0.05$  was used.

A structural equation model (SEM) (Grace, 2006) was also employed to test the relative importance of direct versus indirect linkages between CO<sub>2</sub> enrichment and vegetation productivity for both drylands and non-drylands using all the available data. SEM statistics were calculated using International Business Machines (IBM) SPSS AMOS version 22 (AMOS Development Corp. Meadville, PA). We used a maximum likelihood based goodness-of-fit test to assess the degree of accord between observed and predicted covariance structures. Because our models were saturated, i.e., all possible pathways between all variables were accounted for, we could not test the significance of our models (Grace, 2006). The calculated path coefficients are based on the amount of variance explained in the response variables and they represent relative strengths of the

specific pathways.  $R^2$  values represent the total variances explained by all of the contributing variables.

To test the soil water response under different climate regimes, we classified the study locations as “dryland vs. non-dryland” based on an aridity index database (Figure 2.1). Following the United Nations Environment Program (UNEP) terminology, drylands are defined as regions where the Aridity Index (AI) is less than 0.65, with AI expressed as the ratio of mean annual precipitation to mean annual potential evapotranspiration. In addition to climatic regimes, a number of other factors might affect the response of the available soil water under  $\text{CO}_2$  enrichment. These include the system type, vegetation type and soil texture. We classified the system types as “natural vs. managed” by defining agriculture as a managed ecosystem and the remainder (i.e., forest and grassland) as natural systems (Figure 2.3A). Similarly, vegetation was discriminated into “woody vs. non-woody”, with the latter comprising grassland and cropland (Figure 2.3B). Soil texture was grouped into two classes based upon the United States Department of Agriculture (USDA) soil texture triangle: (1) Sand, which includes sand and loamy sand; and (2) Loam, which includes loam, clay loam, silt loam, sandy loam, and silty clay loam (Figure 2.3C). To test any potential introduced methodological bias, we compared the results of studies reporting volumetric water content (the predominant unit used in the studies comprising our synthesis) and results using other techniques such as gravimetric water content (Figure 2.3D).

## 2.4 Results and discussion

In order to test my hypothesis and to evaluate the soil water response differences occurring within dryland and non-dryland systems, a total of 45 studies from 8 countries (yielding 1705 measurements from 21 distinct sites), were included in the meta-analysis (Figure 2.1A). The meta-analysis revealed that increasing atmospheric CO<sub>2</sub> to between 1.2 and 2.0 times the ambient CO<sub>2</sub> level has a positive effect on soil water content, as indicated by the fact that the effect size was greater than zero in both drylands and non-drylands (Figure 2.1B). When considering the entire data set, higher CO<sub>2</sub> levels resulted in an 11% increase in soil water content across all systems (Figure 2.1B). Importantly, the analysis revealed that elevated CO<sub>2</sub> significantly enhanced soil water levels in drylands more so than it did in non-drylands ( $P < 0.05$ , Figure 2.1C), with soil water content increasing by 9% in non-drylands compared to 17% in drylands ( $P < 0.05$ , Figure 2.1C). According to our meta-analysis data set, the mean soil water content was 11.6% under the ambient CO<sub>2</sub> level in drylands, while it was 24.1% in non-drylands. Based on the meta-analysis results, the enhanced CO<sub>2</sub> level would result in a 1.9% soil moisture change in drylands and 2.2% change in non-drylands. Although the absolute change of soil moisture in drylands is comparable to that in non-drylands, studies have shown that even a small change of soil moisture in drylands could be significant enough to cause large changes in vegetation productivity (Wang et al., 2010). The CO<sub>2</sub> induced soil water increase seems contrary to the conventional understanding that any additional soil water should be transpired or evaporated in drylands, as water is a limiting resource.



However, similar responses have been observed across many individual studies and are apparent in our global synthesis at both dryland and non-dryland sites, highlighting the strong role vegetation plays in the soil water balance (Rodriguez-Iturbe and Porporato, 2004). Importantly, the observed response lends weight to the hypothesis that any additional soil water in the root zone is then available to facilitate vegetation growth and greening under enhanced atmospheric CO<sub>2</sub>. Determining the mechanisms of stronger soil water responses in drylands requires further investigation, since it is generally thought that elevated CO<sub>2</sub> has a smaller effect on stomatal response during dry periods or under extreme drought (Ainsworth and Rogers, 2007).

The direct effects of elevated CO<sub>2</sub> on photosynthesis can act to increase plant productivity through the alleviation of any carbon limitation (Strain and Cure, 1985). However, CO<sub>2</sub> is not a limiting factor in most drylands, where productivity is governed mainly by water and nutrient constraints (Scholes and Walker, 1993). Assuming that a direct CO<sub>2</sub> effect occurs through the alleviation of carbon limitation in both dryland and non-dryland ecosystems, as shown earlier, our analysis has demonstrated that the indirect soil water response to elevated CO<sub>2</sub> levels is 89% higher in drylands ( $P < 0.05$ , Figure 2.1C), indicating that factors other than a direct CO<sub>2</sub> effect play a role in increasing plant productivity in dryland systems.

To explore this idea further, a SEM approach (Grace, 2006) was used to test the relative importance of direct (increased CO<sub>2</sub> removing any carbon limitation) versus indirect (i.e., increased CO<sub>2</sub> increasing soil water content) links between CO<sub>2</sub> enrichment

and vegetation productivity for both drylands and non-drylands. SEM results show that the CO<sub>2</sub> effect on productivity was stronger for both direct effects on growth (path coefficients = 0.86 for drylands and 0.2 for non-drylands) and indirect effects on soil water content (path coefficients = 0.74 for drylands and 0.13 for non-drylands) (Figure 2.2), providing additional support that CO<sub>2</sub> induced soil moisture increases is important in drylands.

There are other variables that could affect the interaction between soil water content and elevated CO<sub>2</sub> level, including soil texture (i.e. sand vs. loam), vegetation type (i.e. woody vs. non-woody) and system type (i.e. managed agricultural system vs. natural forest or grassland). However, with the protocols developed in this exercise, the meta-analysis shows no evidence for any significant effects of these on soil water under higher CO<sub>2</sub> levels (Figure 2.3A-C). In addition to accounting for the potential influence of other factors on vegetation response, the use of different methodologies to quantify soil water content has the capacity to influence the interpretation of results. To test any introduced methodological bias, we compared the results of studies reporting volumetric water content (the predominant unit used in the studies included in our analysis) and results using techniques such as gravimetric water content. The meta-analysis results were consistent between the different approaches (Figure 2.3D).

To date, the global average concentration of CO<sub>2</sub> in the atmosphere has increased by nearly 27% (from 315 ppm to approximately 400 ppm) over the period 1960-2015 (NOAA, 2015), with the expectation of a continued rise into the 21st century. To establish

the validity of using results from higher CO<sub>2</sub> enrichment experiments (1.2 to 2.0 times ambient atmospheric CO<sub>2</sub>) to explain the soil water-vegetation responses observed under current CO<sub>2</sub> levels, we examined the sensitivity of soil water change to varying levels of CO<sub>2</sub> using a regression analysis. Using the global meta-analysis data, a significant positive change in soil water along the CO<sub>2</sub> enrichment gradient was determined ( $P < 0.05$ , Figure 2.4), supporting the CO<sub>2</sub> enrichment effect on soil water. At the same time, the rate of change was low (slope = 0.138, Figure 2.4), indicating that soil water changes in response to CO<sub>2</sub> are comparable between higher CO<sub>2</sub> enrichment levels (1.2-2.0) and currently observed CO<sub>2</sub> enrichment (~1.27). The stability of the rate of change justifies using higher CO<sub>2</sub> enrichment levels to interpret soil water responses to currently observed CO<sub>2</sub> enrichment.

As noted earlier, increased CO<sub>2</sub> is not the only potential driver of changes in vegetation response. Temperature increases could also affect dryland plant productivity and greenness. Studies on the impact of concurrent CO<sub>2</sub> and temperature increase upon *WUE* have found that *WUE* substantially increased with elevated CO<sub>2</sub>, despite a significant increase in air temperature, because the increase in leaf temperature is not significantly different between CO<sub>2</sub> treatments due to evaporative cooling of the leaf (Eamus, 1991). In addition, none of the CO<sub>2</sub> enrichment studies used in this data synthesis have a concurrent temperature treatment operating, indicating that temperature is not a confounding factor for our main conclusion. At the same time, we argue temperature is an important factor to constrain the degree of CO<sub>2</sub> induced greening due to its direct and negative impact on *WUE*

and vegetation phenology. For example, an experiment at an agricultural field in a semi-arid region of China showed that *WUE* could decrease by 7.3% with a mean daily temperature increase of 1.2°C (Xiao et al., 2007). In some Mediterranean-type ecosystems such as annual-dominated California grasslands, warming has accelerated the decline of canopy greenness because the effects of reduced transpiration losses push the canopy to an earlier senescence (Zavaleta et al., 2003). These facts indicate that the positive effect of CO<sub>2</sub> induced water savings may eventually be offset by the negative effect of CO<sub>2</sub> induced temperature increases when the temperature increase crosses a certain threshold. Further understanding of this complex feedback process is required.

## **2.5 Conclusions**

Dryland greening presents something of a paradox in our intuitive understanding of plant-water-CO<sub>2</sub> interactions. Combining our meta-analysis results and early work, it illustrates that higher concentrations of atmospheric CO<sub>2</sub> induce plant water saving and that consequent available soil water increases are a likely driver of the observed greening phenomena. The results support recent modeling work showing higher vegetation *WUE* and higher maximum vegetation cover under CO<sub>2</sub> enrichment in warm and dry environments (Donohue et al., 2013). The time scale of the CO<sub>2</sub> enrichment effect on greening may have potential implications on global carbon budgets, as drylands have been found to be significant players in modulating the inter-annual variability of carbon cycling (Poulter et al., 2014). By identifying the contributing mechanisms that result in vegetation greenness, the findings provide important insights into plant-water interactions. Predicting

system level response to future climatic and/or anthropogenic perturbations in dryland systems remains a critically important but under-investigated area of inquiry.

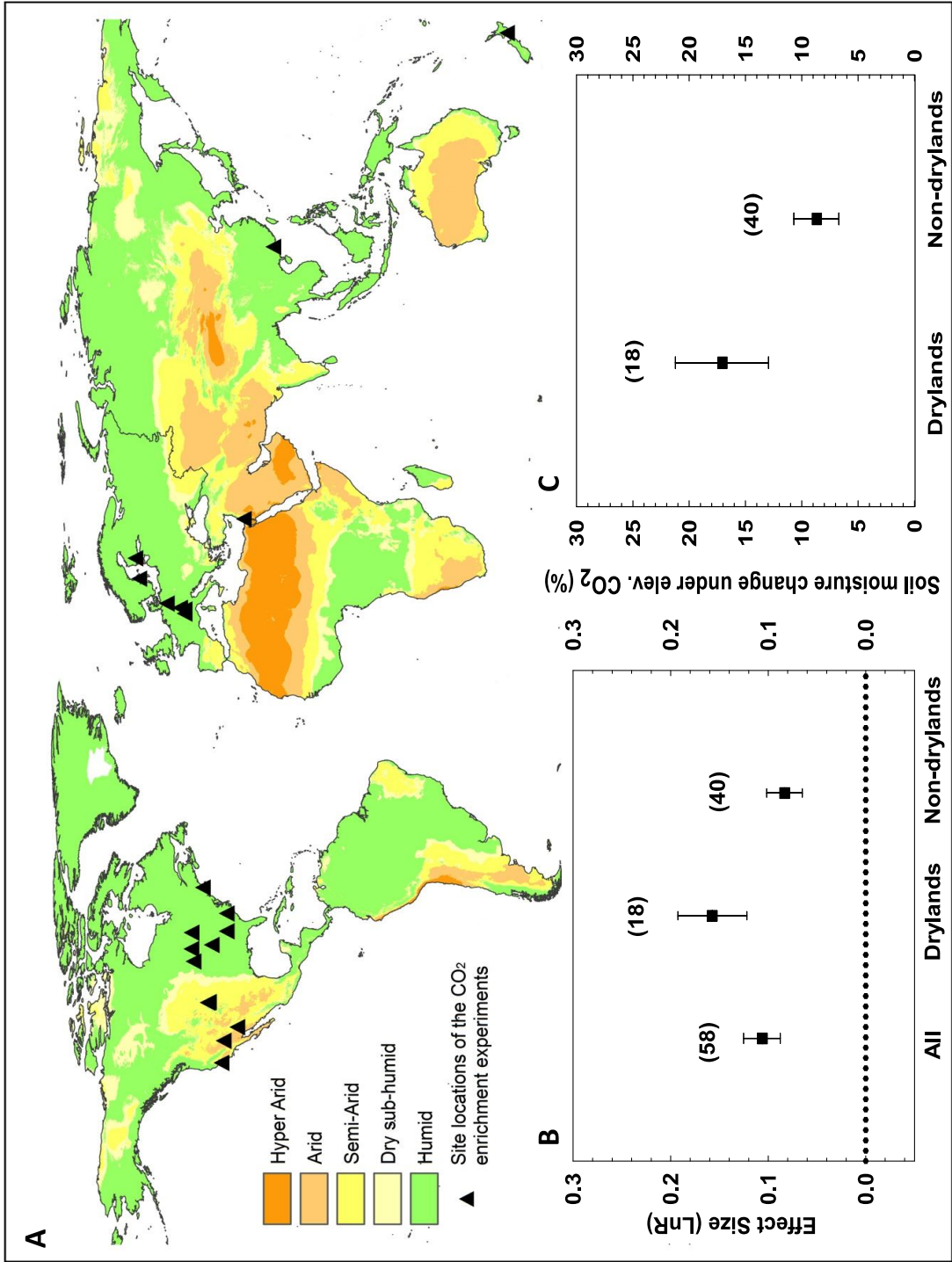


**Figure 2.1** Global climate map and a comparison of mean effect size and soil water response under elevated CO<sub>2</sub>. A. Site locations of the CO<sub>2</sub> enrichment experiments together with globally distributed climate zones based on a standard aridity index formulation (precipitation/potential evapotranspiration); B. Mean effect size of soil water content under elevated CO<sub>2</sub> for the entire data set, under dryland and non-dryland regimes. The effect size was calculated as the natural log of the magnitude of an experimental treatment mean (the soil water under elevated CO<sub>2</sub>) relative to the control treatment mean (the soil water under ambient CO<sub>2</sub>); C. Enhancement of soil water content under elevated CO<sub>2</sub> for dryland versus non-dryland regimes. The number of cases is shown in brackets. Error bars are bootstrapped confidence intervals (*CI*). All the statistics are significant at  $P < 0.05$ . The map was generated using ArcGIS for Desktop 10.3.1 (<http://www.arcgis.com>).

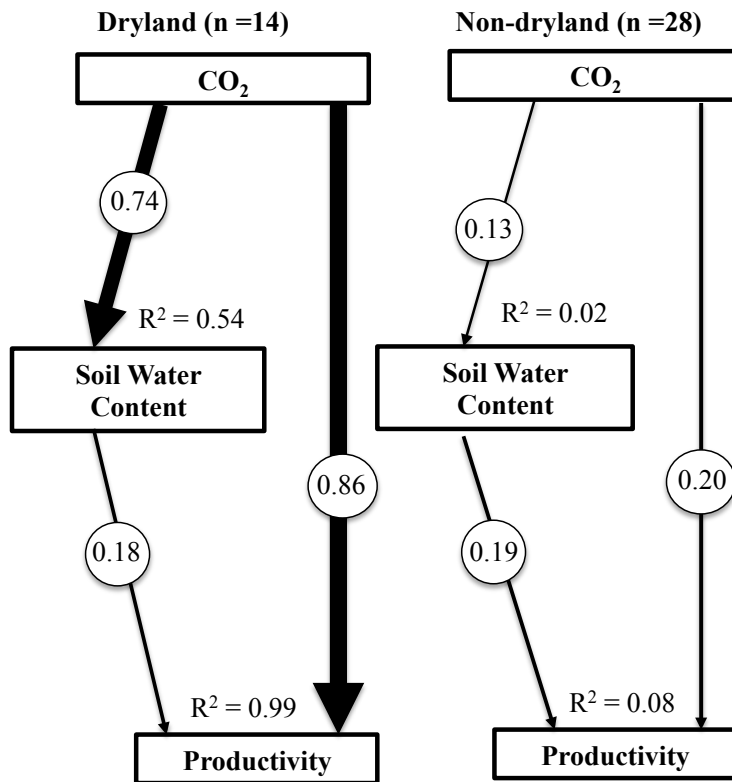


**Figure 2.2** Structural equation modeling of direct and indirect effects of CO<sub>2</sub> enrichment on vegetation productivity for both drylands and non-drylands. The number of cases is shown in brackets. Arrow thickness is proportional to path coefficient.



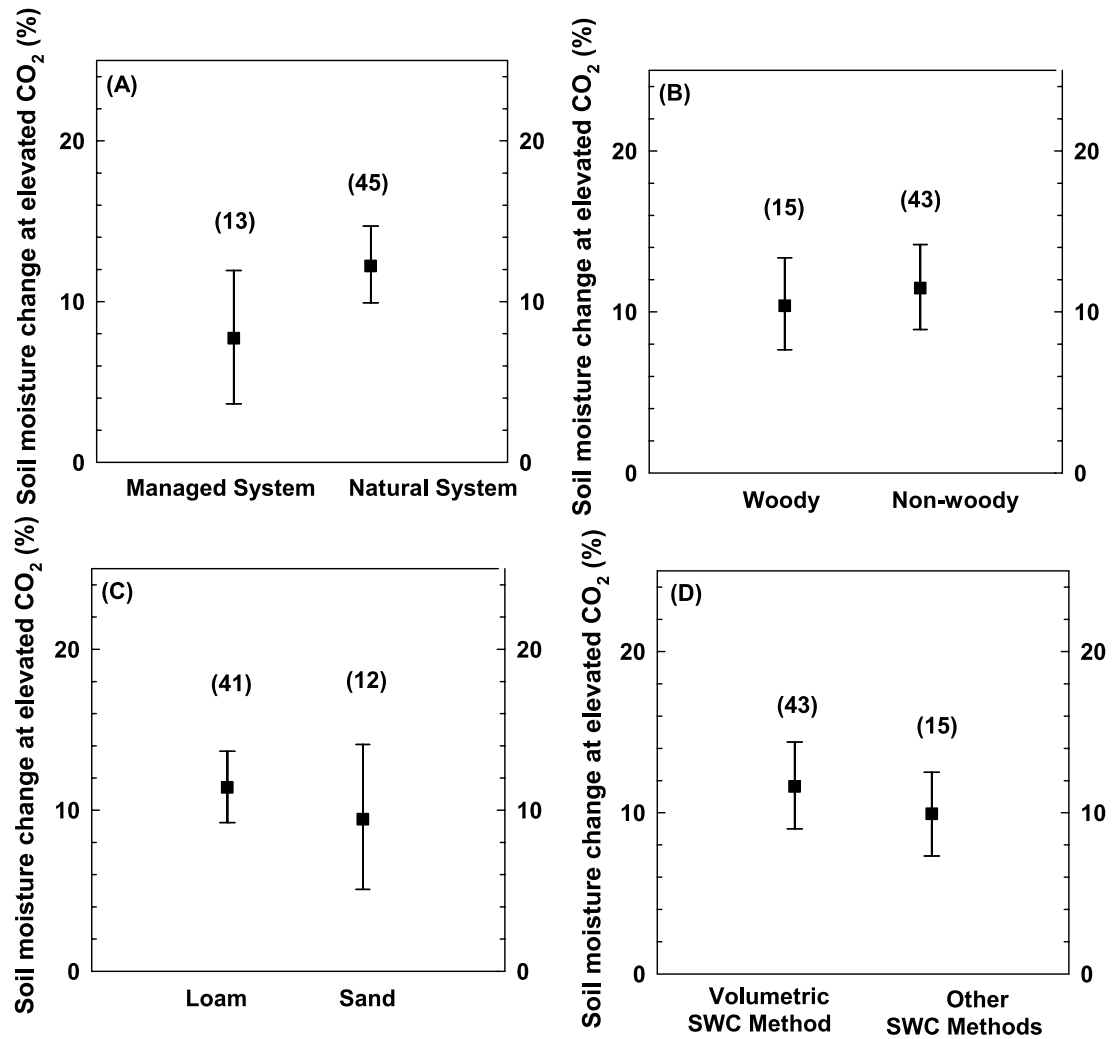


**Figure 2.3** Enhancement of soil water content for elevated CO<sub>2</sub> levels (A) under different management systems; B) under different vegetation types; and (C) under different soil texture; and (D) using results from different soil water content (SWC) measurement methods (volumetric method, gravimetric method). The number of cases is shown in brackets. Error bars are bootstrapped confidence intervals (*CI*). All the statistics are significant at  $P < 0.05$ .

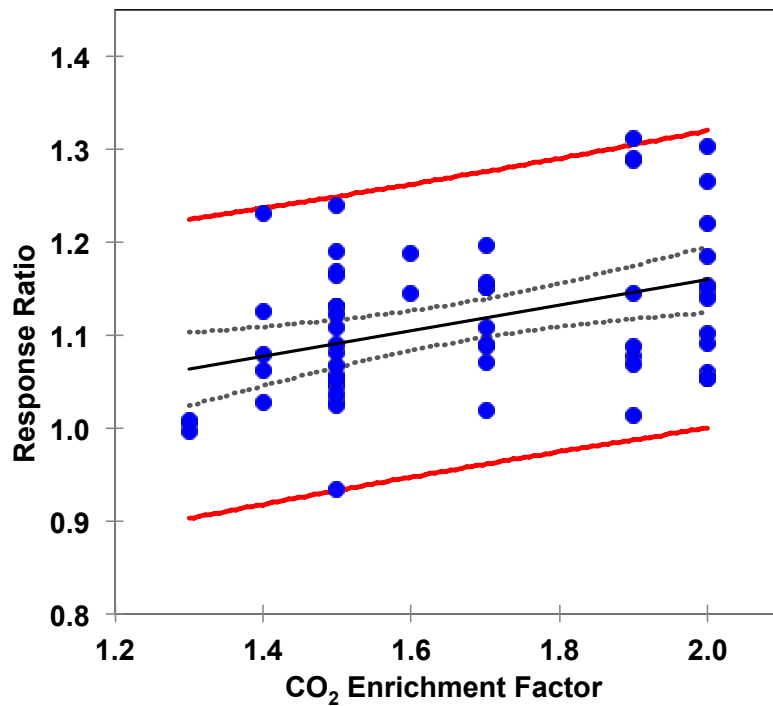


**Figure 2.4** Sensitivity of the soil water response to CO<sub>2</sub> enrichment for the entire data set.

The response index was calculated as the soil water content under elevated CO<sub>2</sub> divided by the soil water content under ambient CO<sub>2</sub>. The closed circles are the observations, with the solid black line providing a linear regression. The red lines represent the 95% confidence intervals of the observations and the dashed grey lines represent the 95% confidence interval of the model.  $m$  is the slope of the regression line.

## References

- Ainsworth, E.A., Rogers, A., 2007. The response of photosynthesis and stomatal conductance to rising [CO<sub>2</sub>]: mechanisms and environmental interactions. *Plant, Cell & Environment*, 30(3): 258-270.
- D'Odorico, P., Bhattachan, A., Davis, K., Ravi, S., Runyan, C., 2012. Global desertification: drivers and feedbacks. *Advances in Water Resources*.
- Donohue, R.J., Roderick, M.L., McVicar, T.R., Farquhar, G.D., 2013. Impact of CO<sub>2</sub> fertilization on maximum foliage cover across the globe's warm, arid environments. *Geophysical Research Letters*, 40(12): 3031-3035.
- Eamus, D., 1991. The interaction of rising CO<sub>2</sub> and temperatures with water use efficiency. *Plant, Cell & Environment*, 14(8): 843-852.
- Eldridge, D.J., Bowker, M.A., Maestre, F.T., Roger, E., Reynolds, J.F., Whitford, W.G., 2011. Impacts of shrub encroachment on ecosystem structure and functioning: towards a global synthesis. *Ecology Letters*, 14(7): 709-722.
- Farquhar, G., Ehleringer, J., Hubick, K., 1989. Carbon isotope discrimination and photosynthesis. *Annual Review Plant Physiology and Plant Molecular Biology*, 40: 503-537.
- Fensholt, R., Langanke, T., Rasmussen, K., Reenberg, A., Prince, S.D., Tucker, C., Scholes, R.J., Le, Q.B., Bondeau, A., Eastman, R., Epstein, H., Gaughan, A.E., Hellden, U., Mbow, C., Olsson, L., Paruelo, J., Schweitzer, C., Seaquist, J., Wessels, K., 2012. Greenness in semi-arid areas across the globe 1981-2007 - an

- Earth Observing Satellite based analysis of trends and drivers. *Remote Sensing of Environment*, 121: 144-158.
- Gilbert, N., 2011. United Nations considers creating advisory panel on land degradation akin to IPCC. *Nature*, 477: 262-264, doi:10.1038/477262a.
- Grace, J.B., 2006. *Structural equation modeling and natural systems*. Cambridge University Press.
- Hellden, U., Tottrup, C., 2008. Regional desertification: A global synthesis. *Global and Planetary Change*, 64(3-4): 169-176.
- Herrmann, S.M., Anyamba, A., Tucker, C.J., 2005. Recent trends in vegetation dynamics in the African Sahel and their relationship to climate. *Global Environmental Change-Human Policy Dimensions.*, 15(4): 394-404.
- Herrmann, S.M., Tappan, G.G., 2013. Vegetation impoverishment despite greening: A case study from central Senegal. *Journal of Arid Environments*, 90: 55-66.
- Liu, Y.Y., Dijk, A.I.J.M.v., Jeu, R.A.M.d., Canadell, J.G., McCabe, M.F., Evans, J.P., Wang, G., 2015. Recent reversal in loss of global terrestrial biomass. *Nature Climate Change*, 5(5): 470-474.
- Millennium Ecosystem Assessment, 2005. *Ecosystems and human well-being: desertification synthesis*. World Resources Institute, Washington, DC.
- Nielsen, T.T., Adriansen, H.K., 2005. Government policies and land degradation in the Middle East. *Land Degradation & Development*, 16(2): 151-161.

NOAA/ESRL.

<http://www.esrl.noaa.gov/gmd/ccgg/trends>, (2015) (Date of access: 05/11/2015).

Osborne, C.P., Woodward, F.I., 2001. Biological mechanisms underlying recent increases in the NDVI of Mediterranean shrublands. *International Journal of Remote Sensing*, 22(10): 1895-1907.

Poulter, B., Frank, D., Ciais, P., Myneni, R.B., Andela, N., Bi, J., Broquet, G., Canadell, J.G., Chevallier, F., Liu, Y.Y., 2014. Contribution of semi-arid ecosystems to interannual variability of the global carbon cycle. *Nature*, 509(7502): 600-603.

Rodriguez-Iturbe, I., Porporato, A., 2004. *Ecohydrology of water-controlled ecosystems: Soil moisture and plant dynamics*. Cambridge University, Cambridge, UK.

Rosenberg, M.S., Adams, D.C., Gurevitch, J., 2000. *MetaWin. Statistical Software for Meta-Analysis. Version 2.0*. Sinauer Associates, Sunderland, MA.

Runnström, M.C., 2000. Is northern China winning the battle against desertification? Satellite remote sensing as a tool to study biomass trends on the Ordos Plateau in semiarid China. *AMBIO: A Journal of the Human Environment*, 29(8): 468-476.

Schimel, D.S., 2010. Drylands in the Earth System. *Science*, 327(5964): 418-419.

Scholes, R.J., Walker, B.H., 1993. *An African savanna: synthesis of the Nylsvley study*. Cambridge University Press.

Strain, B.R., Cure, J.D., 1985. *Direct effects of increasing carbon dioxide on vegetation*. United States Department of Energy Washington, DC.

- Wang, L., D'Odorico, P., Evans, J., Eldridge, D., McCabe, M., Caylor, K., King, E., 2012. Dryland ecohydrology and climate change: critical issues and technical advances. *Hydrology and Earth System Sciences*, 16: 2585-2603.
- Wang, L., D'Odorico, P., Ries, L., Caylor, K., Macko, S., 2010. Combined effects of soil moisture and nitrogen availability variations on grass productivity in African savannas. *Plant Soil*, 328: 95-108, 10.1007/s11104-009-0085-z.
- Xiao, G., Zhang, Q., Yao, Y., Yang, S., Wang, R., Xiong, Y., Sun, Z., 2007. Effects of temperature increase on water use and crop yields in a pea–spring wheat–potato rotation. *Agricultural Water Management*, 91(1): 86-91.
- Zavaleta, E.S., Thomas, B.D., Chiariello, N.R., Asner, G.P., Shaw, M.R., Field, C.B., 2003. Plants reverse warming effect on ecosystem water balance. *Proceedings of the National Academy of Science*, 100(17): 9892-9893.

**CHAPTER 3: EVALUATION AND DEVELOPMENT OF  
ECOHYDROLOGICAL MODELING FRAMEWORK TO LINK  
ATMOSPHERIC CO<sub>2</sub>, STOMATAL CONDUCTANCE RESPONSE, AND  
ROOT-ZONE SOIL MOISTURE DYNAMICS**

**3.1 Abstract**

The establishment of an accurate stomatal conductance ( $g_s$ ) model in responding to CO<sub>2</sub> enrichment under diverse environmental conditions remains an important research issue as  $g_s$  is a key factor in understanding plant-water-atmosphere interactions and how changing climate affects vegetation responses. Although there are  $g_s$  models with different levels of complexity, no previous studies have attempted to evaluate these models using the same set of measurements from various environmental conditions. In this study, we evaluated three of the most commonly-used  $g_s$  formations for the estimation of the stomatal response to environmental factors using *in situ* measurements under different environmental conditions. The three  $g_s$  models were Leuning's modified Ball-Berry model, and two specific cases of the optimization models (i.e., Rubisco limitation model and RuBP regeneration limitation model). Based on an analysis of 234 data points obtained from field experiments under instantaneous, semi-controlled and the Free-Air CO<sub>2</sub> Experiment (FACE) conditions, we found that Leuning's modified Ball-Berry model and RuBP limited optimization model showed similar performance and both performed better than Rubisco limitation model. Functional groups (e.g., C<sub>3</sub> versus C<sub>4</sub> species) and life form (e.g., annual versus perennial species) play an important role in

determining the  $g_s$  model performance and thus pose a challenge for  $g_s$  predictions in mixed vegetation communities. Further, a conceptual relationship was developed to link the relative effect of a change in  $g_s$  to the soil water status, which helped to better understand the atmospheric  $\text{CO}_2$  effect on root-zone soil moisture dynamics in dryland systems where soil water is a limiting factor in vegetation growth and function.



### 3.2 Introduction

Stomata control the water losses and CO<sub>2</sub> uptake between plant and atmosphere, and therefore play a key role in determining the vegetation response to climate change. Stomatal conductance (hereafter  $g_s$ ) modeling has long been used as an effective and well-adapted tool to study the physiological controlling mechanisms of stomata. A large number of studies have modeled stomatal behavior as a function of environmental factors, such as CO<sub>2</sub>, light, relative humidity or vapor pressure deficit (Ball et al., 1987; Cowan and Farquhar, 1977b; Jarvis, 1976; Leuning, 1995). There are three basic approaches to modeling stomatal conductance; namely empirical approach, mechanistic (process-based) approach, and economic (optimization-based) approach (Buckley and Mott, 2013). In addition to the categorization based on modeling methods employed, the stomatal conductance models can also be categorized into two major types, depending on whether physiological constraint or hydrological limitation is the main controlling factor for stomatal response. The former models express  $g_s$  as a function of the biochemical and physiological processes associated with carbon dioxide assimilation, and the latter express  $g_s$  as a function of water availability such as soil water content (Damour et al., 2010).

The advantages and disadvantages of these different modeling approaches are well acknowledged. Most leaf and canopy gas exchange studies use the empirical (phenomenological) models because they are simpler, and in many conditions, agree well with direct  $g_s$  measurements (Buckley and Mott, 2013). The widely used empirical

models include the multiplicative and empirical model of Jarvis (1976), ‘Ball-Berry’ model (1987), and modified ‘Ball-Berry’ model by Leuning (1995). The major limitation of such models is that the empirical approach relies on the choice of certain sets of empirical parameters and the use of statistical correlations to assume a link of the relevant mechanisms to the processes, so it cannot fully describe the system behaviors and interactions (Adams et al., 2013). It is worth noting, however, both Ball-Berry’s model and Leuning’s modified ‘Ball-Berry’ model have showed good agreement with observations across a broad range of vegetation types (Ball et al., 1987; Collatz et al., 1992; Harley et al., 1992; Leuning, 1995).

To address the limitations of empirical models, some recent studies have attempted to model  $g_s$  in a more comprehensive and mechanistically explicit way (Adams et al., 2013; Buckley and Mott, 2013; Dewar, 2002; Gao et al., 2002). However, the mechanistic knowledge is often difficult to translate into a mathematic framework (Damour et al., 2010), and parameters associated with biophysical properties are difficult to measure experimentally (Buckley and Mott, 2013). In reality, the mechanistic models are less often used to predict the environmental stimuli’s impact on  $g_s$  in the cellular and subcellular processes. Because it is generally easier to build models using observations, the majority of stomatal conductance models are ‘semi-empirical’, meaning that the models are built on physiological mechanisms, but are combined with empirical functions (Damour et al., 2010).

The optimization approach is pioneered by Cowan & Farquhar (Cowan and Farquhar, 1977b), based on the theory that plants tend to maximize CO<sub>2</sub> assimilation for a fixed amount of water loss or tend to minimize water loss for a fixed amount of CO<sub>2</sub> assimilation. Using Lagrange transformation, the optimization theory has been mathematically translated into the assumption that the marginal water cost per unit carbon gain  $\partial E/\partial A_{net}$ , i.e. the ratio of the sensitivities of rate of transpiration ( $E$ ) and net carbon assimilation ( $A_{net}$ ) to changes in  $g_s$ , stomatal remains constant and equals to the Lagrange multiplier  $\lambda$  during a finite time interval (i.e., within a given day) (Cowan and Farquhar, 1977b; Damour et al., 2010). Although there has been debated that  $\lambda$  may vary with environmental conditions and is difficult to measure (Buckley, 2007; Collatz et al., 1992; Makela et al., 1996), the optimization models have recently received renewed interest because they do not require a priori specification to describe the response of observed stomatal conductance to environmental variables (Manzoni et al., 2011; Medlyn et al., 2011). The optimization models provide a close-form expression for  $g_s$  as a function of environmental variables and an additional parameter  $\lambda$  (Vico et al., 2013). There are two major assumptions for optimization models, in which Katul (2009) and Lloyd and Farquhar (1994) assumed that leaf photosynthesis is limited by Rubisco activity (i.e. limited by CO<sub>2</sub> availability within the sub-stomatal cavity), while Medlyn et al. (2011) focused on conditions where photosynthesis was limited by ribulose-1,5-biphosphate (RuBP regeneration) regeneration rate (i.e. limited by light availability).

The stomatal conductance models also can be categorized into CO<sub>2</sub> assimilation models and water limited conductance models (Damour et al., 2010). The CO<sub>2</sub> assimilation models focus on the biochemical and physiological processes associated with carbon assimilation, and so these are also called moisture-independent models. The model assumes that the stomatal conductance is regulated by the environmental variables such as light, temperature, CO<sub>2</sub> and nitrogen through the biochemical processes of assimilation (Cowan and Farquhar, 1977a; Farquhar et al., 1980; Field and Mooney, 1986). Ball-Berry model (Ball et al., 1987) and Leuning's (1995) modified version have been recognized as the most widely-used moisture-independent models to successfully estimate the stomatal conductance for well-watered systems. In contrast, the water limited conductance models are called moisture-limited models because they attempt to address the water limitation, either through scaling a photosynthesis-based model using some factors representing water stress (e.g. Albertson and Kiely, 2001; Jacquemin and Noilhan, 1990; Rodriguez - Iturbe et al., 1999; Thornthwaite and Mather, 1955), or by linking the rate of stomatal conductance with soil moisture status by assuming there is a continuous functional dependence of conductance upon soil moisture (e.g., Buckley et al., 2003; Dewar, 2002; Gao et al., 2002; Katul et al., 2003).

Stomata respond to environmental stimuli in a complex way. Therefore, it has been challenging to design  $g_s$  models that are capable to deal simultaneously with all the environmental factors. The establishment of a reliable and general stomatal conductance model remains an important research problem since  $g_s$  is the key for understanding the

plant-water-atmosphere interactions and how changing climate affects the three-way interactions. A recent study introduced by our group (Lu et al., 2016) has described that the greening in global drylands is a response to higher CO<sub>2</sub> levels. Thus, we hypothesize that elevated CO<sub>2</sub> decreases stomatal conductance and increases vegetation water use efficiency, and subsequently increases the available soil moisture under the same productivity level. This study will help to evaluate such hypothesis from the modeling perspective. A complex model with physical based and realistic parameterization likely performs well; however, development of such a model can be difficult due to numerous model parameters and data inputs. In this study, I will evaluate three of the most commonly-used  $g_s$  models for estimation of stomatal response to environmental stimuli using *in situ* measurements under different environmental conditions. To our knowledge, no previous study has used the same dataset to test all three different model predictions simultaneously, and to test them under diverse conditions. The second objective of this study is to develop a modeling framework that could link the changes in stomatal conductance and soil water status. The establishment of this framework is important in dryland systems where soil water is a limiting factor in vegetation growth and function (Rodriguez-Iturbe and Porporato, 2004).

### **3.3 Methods**

#### **3.3.1 Model formulation**

In this study, I tested three  $g_s$  models: the Leuning's modified Ball-Berry model that is the modification of a widely used semi-empirical Ball-Berry approach, and the two

solutions to the stomatal optimization theory for estimating  $g_s$ : the optimization model for RuBP regeneration limitation, and the optimization model for Rubisco limitation. These two cases presented the optimal extreme conditions since it is assumed that stomata aperture was optimized either under RuBP regeneration limitation or under Rubisco limitation only. Although the mechanistic models are theoretically better for predicting the stomatal response to environmental stimuli, the complex parameterization make it difficult to parameterize in the field setting, and therefore no mechanistic model was chosen for this study.

#### 1. Ball-Berry and Leuning's stomatal conductance models

Ball et al. (1987) developed one of the most commonly used models of  $g_s$ . It assumed that stomatal conductance is a function of photosynthetic rate ( $A$ ), CO<sub>2</sub> concentration at the leaf surface ( $C_a$ ), and humidity deficit ( $D$ ). Leuning (1995) suggested a hyperbolic function of  $D$  for humidity response, so the mathematical form of Leuning's modified Ball-Berry model is given by

$$g_s = g_0 + a_1 \frac{A}{(C_a - \Gamma)(1 + D/D_0)} \quad (1)$$

where  $g_0$ ,  $a_1$  and  $D_0$  are empirically determined coefficients, and  $\Gamma$  is the CO<sub>2</sub> compensation point, which is zero for C<sub>4</sub> plant (Cox et al., 1998).

Cox et al. (1998) showed that the Ball-Berry and Leuning models produced good fits to the experimental data, and in both cases the optimal minimum canopy conductance  $g_0$  was relatively small, and thus suggested to simplify Leuning's model by taking  $g_0$

as zero. Based on simplified Leuning's model, Yu et al. (2001) further proposed to use gross assimilation rate instead of net assimilation, and correspondingly use  $C_a$  to replace  $C_a - \Gamma$ , because stomatal conductance could increase immediately with increasing light even below the light compensation point. Next, by taking humidity response parameter  $D_0$  as 1.5 kpa (Leuning, 1995), the Leuning's model shows the following approximation:

$$g_s \sim a_1 \frac{A}{C_a \times (1 + D/1.5)} \quad (2)$$

Many other studies, however, showed better results when  $f(D) = D^{-1/2}$  was used for humidity response than a hyperbolic function of  $D$ . It is interesting to note when replacing  $D$  with a form of  $D^{-1/2}$ , the Leuning's modified Ball-Berry's photosynthesis model shows a similar approximation for the function of  $A$ ,  $C_a$  and  $D$ , as the RuBP regeneration limitation optimization model does.

## 2. Optimization model for RuBP regeneration limitation

CO<sub>2</sub> fixation can be limited by Rubisco kinetics or by the regeneration of RuBP or co-limited by both. Here we tested two model solutions derived from optimal stomatal theory as shown in Vico et al. (2013). The first model assumed that stomatal aperture was optimized under RuBP regeneration, and the atmospheric CO<sub>2</sub> concentration was much larger than the CO<sub>2</sub> compensation point (i.e.,  $c_a \gg \Gamma$ ) and  $c_a \gg a\lambda D$  ( $a = 1.6$ ,  $\lambda$  is the marginal water use efficiency). Based on this assumption, Medlyn et al.'s (2011) derived the following approximation on the left for the optimal stomatal conductance, and Vico et al. further simplified the equation to obtain the approximation on the right (Vico et al., 2013):

$$g_s \sim \frac{A}{c_a \sqrt{D}} a(\sqrt{D} + \sqrt{\frac{3\Gamma}{a\lambda}}) \sim \frac{A}{c_a \sqrt{D}} \sqrt{\frac{3a\Gamma}{\lambda}}, \quad (3)$$

where  $\Gamma$  is the CO<sub>2</sub> compensation point.

### 3. Optimization model for Rubisco limitation

The second model was derived by Katul et al. (2009) assuming that stomatal aperture was optimized under Rubisco limitation only, and  $c_a \gg \Gamma$ , so the following linear dependence of stomatal conductance can be found (Vico et al., 2013):

$$g_s \sim \frac{A}{c_a \sqrt{D}} \sqrt{\frac{c_a}{a\lambda}}, \quad (4)$$

I re-arranged equation (4) and obtained the following expression:

$$g_s \approx \frac{A}{\sqrt{c_a D}} \sqrt{\frac{1}{a\lambda}}, \quad (5)$$

Assuming that  $\lambda$  is constant, the relations of equation (3) and (5) show that the  $g_s$  could be linearized with the function of  $C_a$ ,  $A$ , and  $D$ , with the slopes of the lines being proportional to  $(3a\Gamma/\lambda)^{1/2}$  for RuBP regeneration limited model and  $(a\lambda)^{-1/2}$  for Rubisco limited model. Although  $\lambda$  may vary with environmental conditions for long-term (monthly to seasonal), in practice,  $\lambda$  can often be considered constant for short term (i.e., sub-hourly to daily) exposure to changing environmental conditions (Vico et al., 2013).

### 3.3.2 Testing data sets

This study consisted of two-steps, model evaluation and modeling framework development. The model evaluation was based on an analysis of data obtained from various field experiments in which changes in stomatal conductance were measured under acclimation to atmospheric CO<sub>2</sub> concentrations under different environmental conditions.



A comprehensive literature search using the terms ‘CO<sub>2</sub> acclimation’, ‘stomatal conductance’, ‘FACE’, and ‘growth chamber’ was conducted across Thomson Reuters Web of Science and Google Scholar databases. All of the field data used in this study was derived from *in-situ* field experiments that examined stomatal conductance responses to different atmospheric CO<sub>2</sub> levels. The raw data was summarized in Appendix B.

Three types of field measurements were used to evaluate the performance of the three photosynthesis models. The conditions to be tested included: (1) the instantaneous measurement of  $g_s$  and atmospheric CO<sub>2</sub> concentration (hereafter  $C_a$ ), (2) the measurement of  $g_s$  and  $C_a$  from semi-controlled plant growth facility, and (3) the Free-Air CO<sub>2</sub> Experiment (FACE) measurement of  $g_s$  and  $C_a$ . For a better comparison, we re-adjusted the x-axis (i.e.,  $f(A, C_a, D)$ ) for Rubisco simulation, to scale it to the same range of  $f(A, C_a, D)$  as those of Leuning’s modified Ball-Berry model and RuBP limited model. Such adjustments do not change the slope and R<sup>2</sup> values of  $f(A, C_a, D)$  and  $g_s$  correlation for the Rubisco model.

In the instantaneous  $g_s$  measurements, each chamber measurement was made over a short period in the field, and the environmental conditions were kept constant. For example, Yu et al. (2004) conducted leaf gas exchange measurements in a winter wheat cropping system at North China Plain. In the experiment, the  $C_a$  was varied from 0 to 1000  $\mu\text{mol mol}^{-1}$  in the leaf chamber to get instantaneous  $g_s$  response to CO<sub>2</sub>, while temperature, humidity and wind speed over the leaves were kept constant.

For semi-controlled conditions, the steady-state leaf gas-exchange was measured in a semi-controlled plant growth facility that allowed the study of the effects of elevated CO<sub>2</sub> on the growth of plants under radiation and temperature conditions similar to the field (Anderson et al., 2001; Maherali et al., 2002). Only a few studies have investigated the stomatal acclimation to CO<sub>2</sub> in the field under semi-controlled conditions. Through an extensive literature search, five sets of semi-controlled measurement data sets were extracted from the literature and analyzed.

Much of the FACE studies compared  $g_s$  responses of plants grown under ambient  $C_a$  with those grown under doubled CO<sub>2</sub> concentration. In FACE experiments, the environmental factors such as leaf temperature and atmospheric water vapor pressure entering the chamber were not controlled during measurements but  $g_s$  was measured when it reached steady state. The database of FACE studies used in this study was extracted from 43 studies that have determined the response of  $g_s$  to CO<sub>2</sub> concentration ranging from 330 to 757  $\mu\text{mol mol}^{-1}$ , corresponding to 35 different plant species or growing conditions. These studies included thirteen datasets for C<sub>3</sub> crops, two datasets for C<sub>3</sub> herbaceous plants, eight datasets for C<sub>3</sub> grasses, seven datasets for C<sub>3</sub> shrubs, seventeen datasets for C<sub>3</sub> trees, four datasets for C<sub>4</sub> crops and four datasets for C<sub>4</sub> grasses.

### **3.3.3 Parameter sensitivity analysis**

There are three major factors in equations (2), (3) and (4) controlling  $g_s$ : assimilative rate ( $A$ ), CO<sub>2</sub> concentration ( $C_a$ ), and vapor pressure deficit ( $D$ ). In this study, a sensitivity analysis was conducted to examine which parameter (input) could have the

most influence on the modeled  $g_s$  output, by varying one parameter over its entire range while fixing others (i.e., no interactive effects were tested). For the sensitivity analyses, the mean value derived from the entire database was used as the “base case”, increasing and decreasing by 1% increment to reach the boundary values (i.e., maximum and minimum values derived from the entire database). The percent change in the model output was calculated. The average of the difference in percentage change between two consecutive  $g_s$  output values was then defined as the parameter’s sensitivity, which can be described as:

$$Sensitivity = \frac{\sum_{i=1}^n \Delta g_{s(i)}}{n} \times 100\%, \quad (6)$$

where  $\Delta g_{s(i)}$  is the percentage change of stomatal conductance corresponding to one interval increment in one parameter (e.g., 1% increment is used in this study),  $n$  is the number of intervals.

### 3.4 Results and discussion

#### 3.4.1 Sensitivity analysis

The sensitivity values for  $C_a$  and  $D$  were negative while the assimilative rate  $A$  had the positive values (Table 3.1). Sensitivity analyses suggested that the assimilative rate  $A$  was the most influential factor for all three models among all the parameters with an average sensitivity value of 1.68% (Table 3.1). The average sensitivity values for  $C_a$  and  $D$  varied among the different models.  $C_a$  exhibited the same sensitivity value of 1.25% for Leuning’s modified Ball-Berry model and RuBP limited model, while the Rubisco limited model had a lower average sensitivity value of -0.63% (Table 3.1).  $D$  had the lowest sensitivity values for all of the three models, ranging from -0.57% to -0.64%

(Table 3.1). The results suggested that  $A$  and  $C_a$  were two main parameters controlling the model output for Leuning's modified Ball-Berry model and RuBP limited model, while the model output for Rubisco limitation was more controlled by  $A$  and less controlled by  $C_a$  and  $D$ . All three models were less sensitive to the parameter  $D$ .

### 3.4.2 Evaluation of model performance under different environmental conditions

Figure 3.1 shows the response of  $g_s$  to the function of  $C_a$ ,  $A$ , and  $D$ , as predicted by the Leuning's modified Ball-Berry model and the two single-limitation optimization models, by using the instantaneous measurement data. The response of  $g_s$  to environmental factors was better predicted by Leuning's modified Ball-Berry model and RuBP limited optimization model, with a  $R^2$  value of 0.78 for Leuning's modified Ball-Berry model ( $p < 0.05$ ), and 0.81 for RuBP-limited optimization model ( $p < 0.05$ ) (Figure 3.1). However, the Rubisco-limited optimization model could not predict the response of  $g_s$  well with the functions of  $C_a$ ,  $A$ , and  $D$ , showing a low  $R^2$  value of 0.21 ( $p < 0.05$ ) (Figure 3.1).

None of the three models show a good performance to predict the response of  $g_s$  to the function of  $C_a$ ,  $A$ , and  $D$  using the semi-controlled measurement data (Figure 3.2). The predictability of  $g_s$  using the function of  $C_a$ ,  $A$ , and  $D$  was low for all the three models, with  $R^2$  values ranging from 0.21 to 0.31 ( $p < 0.05$ ) (Figure 3.2). However, there was a significant difference between functional groups. The predictability of  $g_s$  was significantly improved when separating functional groups. The Leuning's modified Ball-Berry model and the RuBP-limited optimization model provided  $R^2$  values of 0.56 and 0.54 ( $p < 0.05$ )

for C<sub>3</sub> species, and R<sup>2</sup> values of 0.67 and 0.58 ( $p < 0.05$ ) for C<sub>4</sub> species, respectively (Figure 3.3). The Rubisco-limited optimization model, however, showed much better  $g_s$  predicting power for C<sub>4</sub> species ( $R^2 = 0.67, p < 0.05$ ) than C<sub>3</sub> species ( $R^2 = 0.19, p < 0.05$ ) (Figure 3.3). Besides the difference in functional groups, it was also found there was a significant difference between annual and perennial species.  $g_s$  can be better predicted by the function of  $C_a$ ,  $A$ , and  $D$  for the annual species alone, with a R<sup>2</sup> value of 0.68, 0.72, and 0.58, for Leuning's model, RuBP limited model and Rubisco limited model, respectively ( $p < 0.05$ ) (Figure 3.4). In comparison, the  $g_s$  predictability on perennial species was much lower, with a R<sup>2</sup> value ranging between 0.25 and 0.36 ( $p < 0.05$ ) (Figure 3.4). This may imply that  $g_s$  is less sensitive to  $C_a$ ,  $A$ , and  $D$  for perennial species than annual species.

Because the environmental factors such as atmospheric water vapor pressure were not monitored in FACE experiments, only the estimates of  $g_s$  as the function of  $C_a$  and  $A$  were tested for FACE data. In general, neither model provides a good estimate of  $g_s$  as the function of  $C_a$  and  $A$  on either C<sub>3</sub> plants or C<sub>4</sub> plants using the FACE data (Figure 3.5). But a detailed analysis of the FACE database used in this study indicated that there was significant variability among functional groups in how  $g_s$  responded to elevated CO<sub>2</sub> (Figure 3.6). On average,  $g_s$  was reduced by 22.8%, 23.6%, 13.5%, 16.6%, 30.5%, and 32.3% in C<sub>3</sub> herbaceous crops, C<sub>3</sub> grasses, C<sub>3</sub> shrubs, C<sub>3</sub> trees, C<sub>4</sub> herbaceous crops, and C<sub>4</sub> grasses, with an atmospheric CO<sub>2</sub> enhancement of 58%, 69%, 59%, 54%, 52%, 81%, respectively. Trees and shrubs showed a lower percentage decrease in  $g_s$  compared to C<sub>3</sub> and C<sub>4</sub> grasses and herbaceous crops, similar to the trend reported previously (Ainsworth

and Rogers, 2007; Nowak et al., 2004; Saxe et al., 1998). When separating into different plant life forms (e.g., trees, shrub or grasses), the predicted linear correlation of  $g_s$  and the function of  $C_a$  and  $A$  on trees and shrubs had been considerably improved. The regression factor of  $R^2$  value increased to 0.70, 0.70 and 0.65 for  $C_3$  trees ( $p < 0.05$ ), 0.87, 0.87 and 0.83 for  $C_3$  shrubs ( $p < 0.05$ ), on linear fitting with Leuning's modified Ball-Berry model, RuBP limited model, and Rubisco limited model, respectively (Figure 3.6). But crops and grasses still had low  $R^2$  value for the  $g_s$  dependence on the function of  $C_a$  and  $A$  (Figure 3.6). It was noted that  $g_s$  might be better predicted by the function of  $C_a$  and  $A$  for the perennial species than for the annual species (Figure 3.7). Although the result seemingly contrasted with what was observed from semi-controlled data, a detailed data check revealed that the majority of annual species were  $C_3$  and  $C_4$  crops, indicating that the functional group could be a more important factor affecting the model performance as discussed in the later sections.

In general, the Leuning's modified Ball-Berry model and RuBP limited optimization model showed similarly better predictive performance than Rubisco limited model. It is not surprising to see that these two models exhibited the similar patterns because the RuBP model was derived structurally homogenous to the classic Ball-Berry model but was based on the optimal stomatal conductance theory (Medlyn et al., 2011). A major difference between these two formulations of  $g_s$  was that Leuning's model used a hyperbolic form of  $D$  while the RuBP limited model used  $f(D) = D^{-1/2}$ . Our sensitivity analysis has indicated that model output for Leuning's modified model and RuBP limited

model were more sensitive to  $A$  and  $C_a$ , and less sensitive to  $D$ , so the modeled stomatal conductance was less influenced by using the different form of the function  $D$ . The RuBP regeneration limited model generally simulated more reasonable  $C_a$  response because its formulation could predict a stomatal closure to rising  $C_a$  for all the values above 200 ppm, while the Rubisco limited formulation predicted that the stomata remained open at rising  $C_a$  up to  $C_a$  values of 500-600 ppm (Buckley, 2017; Medlyn et al., 2013). The current data-driven analytical results generally supported previous findings, but it is noted that other factors such as functional groups could play a more important role in achieving a better model performance.

The results showed that the Rubisco-limited optimization model could not predict the response of  $g_s$  well with the functions of  $C_a$ ,  $A$ , and  $D$ , for any types of the field data on  $C_3$  species. This can be explained by what process is limiting  $A$  at given  $CO_2$  and whether the control of  $A$  shifts from Rubisco to RuBP regeneration as  $CO_2$  arises. For  $C_3$  plants, Rubisco capacity is the predominant limitation on  $A$  at low  $CO_2$  while the limitation shifts to RuBP regeneration capacity at elevated  $CO_2$  (Long and Drake, 1992). Our collected data for  $C_a$  ranged between 100 and 998 ppm, particularly, a major part of the  $C_a$  from the instantaneous measurements and semi-controlled measurements were within the transition for the stomatal aperture being Rubisco activity to RuBP regeneration. As  $C_a$  continued to rise, the photosynthesis on  $C_3$  plants moved towards more predominately limited by RuBP regeneration. To date, the global average concentration of  $CO_2$  in the atmosphere has increased to approximately 405 ppm

(Iugokencky, 2017), which implies that the RuBP limited model maybe give more reasonable prediction.  $C_4$  metabolism behaves in different mechanism in which  $CO_2$  is saturated at low  $C_a$ , and  $A$  is less sensitive to the increase in  $C_a$  (Ghannoum et al., 2000).

Functionally different groups of plants can significantly affect the model performance. Previous studies had indicated that, for  $C_3$  plants, the magnitude of a decrease in Rubisco activity or increase in the capacity for RuBP regeneration varied among the different functional groups. For example, Ainsworth et al. (2007) has shown that trees had the smallest reduction in Rubisco activity when compared to grasses, crops, and shrubs. It was also found that crops reduced Rubisco activity at elevated  $CO_2$  to a greater extent than the capacity for RuBP regeneration (Long et al., 2006). The  $C_4$  plants are different because they are  $CO_2$  saturated at current  $CO_2$ , and when  $CO_2$  rises, the competitive advantage conferred by  $C_4$  metabolism will be reduced (Sage, 2004).

### **3.4.3 Evaluation of model performance under environmental different conditions for dryland data**

The  $CO_2$  assimilation models such as the Ball-Berry model and Leuning's modified version work well under conditions of ample water supply. In this study, I am interested to know whether these models could perform well under water-stressed conditions. Given the limited data available, I tested the performance of Leuning's modified Ball-Berry model and the two optimization models using semi-controlled field measurement data collected at dryland sites. It is not surprising to find that neither model provides a good estimation of  $g_s$  as a function of  $C_a$ ,  $A$ , and  $D$  (Figure 3.8). But it was found that plant



functional groups and life forms might pose a significant influence on the results. The linear correlation of  $g_s$  dependence of the function of  $C_a$  and  $A$  had been considerably improved when data were separated into different plant and life forms (e.g., perennial  $C_3$  grass or annual  $C_3$  grass) (Figure 3.9). The  $R^2$  values generally ranged from 0.65 to 0.90 on linear fitting with Leuning's modified Ball-Berry model and RuBP limited model. However, the predictability of  $g_s$  on perennial  $C_3$  herb and annual  $C_3$  grass was still low for Rubisco limited model, with the  $R^2$  values of 0.02 for annual  $C_3$  grass and 0.16 for perennial  $C_3$  herb (Figure 3.9). This is consistent with the overall trend as we discussed in the previous section.

#### **3.4.4 Development of a modeling framework to link $g_s$ and soil water content**

To develop a conceptual relationship to link stomatal conductance and soil moisture potential, I selected a hydromechanical model that was originally developed by Gao et al. (2002). Although the model has some limitations that may affect the performance at short timescales (e.g., sub-daily) (Emanuel et al., 2007), Gao's model was selected because it did not require a priori assumption of a threshold for soil water limitation (Dewar, 2002; Katul et al., 2003). The model simply assumed there was a linear dependence of stomatal conductance on soil water potential. The water-limited conductance sub-model was used to develop the linkage between  $g_s$  and soil moisture because the availability of soil water is the limiting factor for growth of vegetation in drylands.

Gao's model shows a relation between soil water potential  $\psi_s$  and stomatal conductance  $g_s$  as:

$$g_s = \frac{g_{0m} + k_\psi \psi_s + k_{\alpha\beta} I_p}{1 + k_{\beta g} d_{vp}}, \quad (7)$$

where  $g_{0m}$  is the maximum residual stomatal conductance at saturated soil conditions,  $I_p$  is photosynthetic active radiation (PAR), and  $k_\psi$ ,  $k_{\alpha\beta}$ , and  $k_{\beta g}$  are model-specific parameters,  $d_{vp}$  is  $D$  normalized by atmospheric pressure.

By re-arranging the equation (7), and computing a derivative (see Appendix C), it can find that the relative effect of a change in  $g_s$  on  $\psi_s$  is given by:

$$\frac{d\psi_s}{\psi_s} = \frac{1}{k_\psi} \frac{dg_s}{g_s} + \frac{k_{\beta g}}{k_\psi} \left( \frac{dg_s}{g_s} + \frac{dD_v}{D_v} \right) - \frac{k_{\alpha\beta}}{k_\psi} \frac{dI_p}{I_p}, \quad (8)$$

Next, the dependence of  $g_s$  on  $D_v$  can be further modeled by taking  $\frac{dg_s}{g_s}$  as being proportional to  $\frac{dD_v^{-0.5}}{D_v^{-0.5}}$ . Similarly, the dependence of  $g_s$  on  $I_p$  can be modeled by taking  $\frac{dg_s}{g_s}$  as being proportional to  $\frac{d(1+\beta/I_p)^{-1}}{(1+\beta/I_p)^{-1}}$ . Further, a relation between soil water potential and water content can be modeled by taking  $\frac{d\psi_s}{\psi_s}$  as being proportional to  $\frac{d(\theta)^{-a}}{(\theta)^{-a}}$  (see Appendix C for details). By replacing with all these approximations, it can eventually find that

$$\frac{d\theta}{\theta} = \frac{\left( -\frac{1}{k_\psi} + \frac{k_{\beta g}}{101.3 \times k_\psi} + \frac{k_{\alpha\beta}}{k_\psi} \right) dg_s}{k \times a} \frac{1}{g_s}, \quad (9)$$

where  $k_\psi$ ,  $k_{\alpha\beta}$ ,  $k_{\beta g}$ ,  $\beta$  and  $a$  are model-specific parameters.

### **3.5 Conclusions**

This study evaluated the performance of three commonly-used  $g_s$  models to predict the stomatal conductance response to CO<sub>2</sub> enrichment under different environmental conditions. This is one of the first studies that have attempted to test these models using the same set of measurements from various environmental conditions. Although there could be a potential limitation of using leaf level  $g_s$  models to test canopy-scale measurements (i.e., FACE data), Leuning's modified Ball-Berry model and RuBP limited optimization model generally provided a good estimate of  $g_s$  for all the tested datasets. In addition, the results of this study indicate that variables such as functional groups (e.g., C<sub>3</sub> versus C<sub>4</sub> species) and life form (e.g., annual versus perennial species) may play an important role in determining the stomatal response to changes in environmental factors, and therefore need to be explicitly considered in future modeling framework.

**Table 3.1** Model sensitivity of key parameters for Leuning’s modified Ball-Berry model, RuBP limited optimization model, and Rubisco limited optimization model.

Parameters	Step	Leuning’s modified Ball-Berry model		Optimization model for RuBP limited		Optimization model for Rubisco limited	
		Interval	Average sensitivity (%)	Interval	Average sensitivity (%)	Interval	Average sensitivity (%)
Assimilative rate $A$ ( $\mu\text{mol m}^{-2} \text{s}^{-1}$ )	1%	[1.8, 39.0]	1.68	[1.8, 39.0]	1.68	[1.8, 39.0]	1.68
$\text{CO}_2$ concentration $C_a$ ( $\mu\text{mol mol}^{-1}$ )	1%	[100, 998]	-1.25	[100, 998]	-1.25	[100, 998]	-0.63
Vapor pressure deficit (kPa)	1%	[0.45, 3.2]	-0.57	[0.45, 3.2]	-0.64	[0.45, 3.2]	-0.64

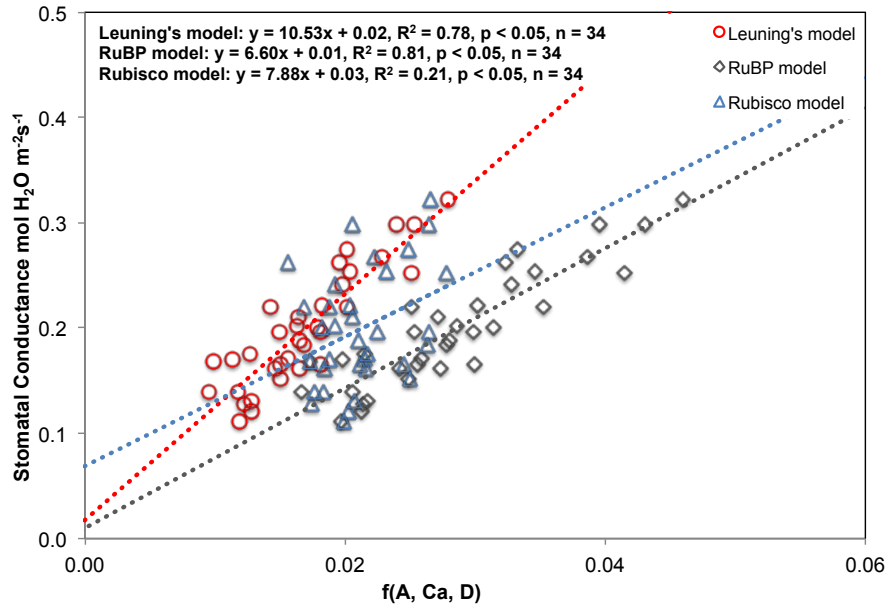


**Figure 3.1** Instantaneous measurements of stomatal conductance  $g_s$  as a function of  $C_a$ ,  $A$ , and  $D$  for the Leuning's modified Ball-Berry model (red open circles), RuBP limited optimization model (grey open squares), and Rubisco limited optimization model (blue open triangles), with  $C_a$  ranging between 200 and 1000 ppm.

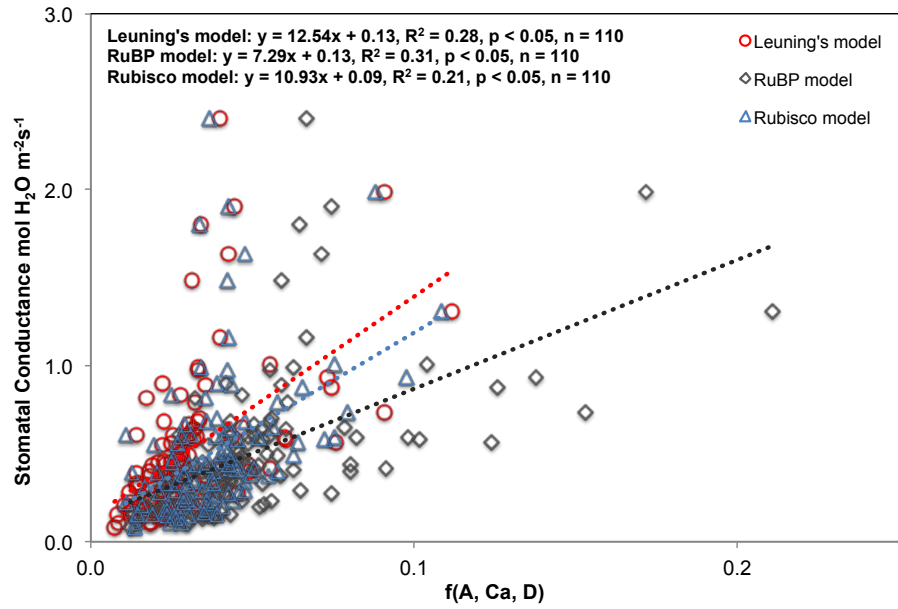


**Figure 3.2** Semi-controlled measurements of stomatal conductance  $g_s$  as a function of  $C_a$ ,  $A$ , and  $D$  for the Leuning's modified Ball-Berry model (red open circles), RuBP limited optimization model (grey open squares), and Rubisco limited optimization model (blue open triangles).

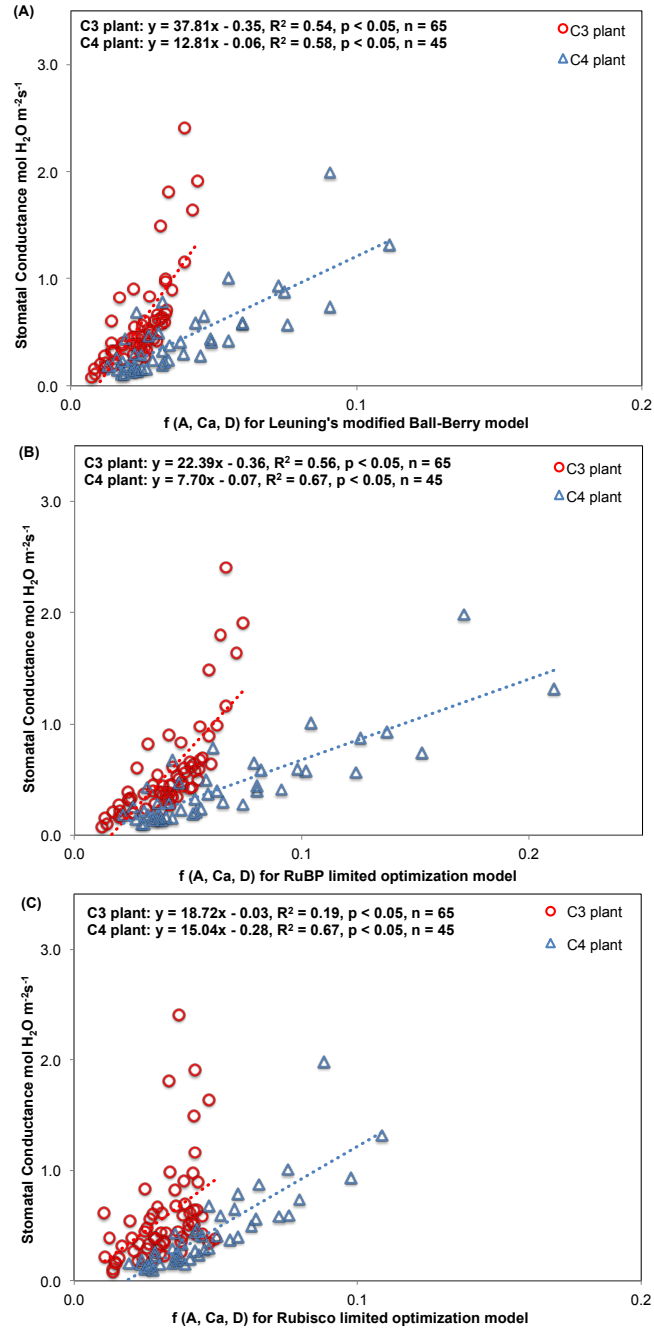


**Figure 3.3** The response of stomatal conductance  $g_s$  as a function of  $C_a$ ,  $A$ , and  $D$  for two functional groups (C<sub>3</sub> plant vs. C<sub>4</sub> plant), for the Leuning's modified Ball-Berry model (A), RuBP limited optimization model (B), and Rubisco limited optimization model (C). The data are from semi-controlled measurements.

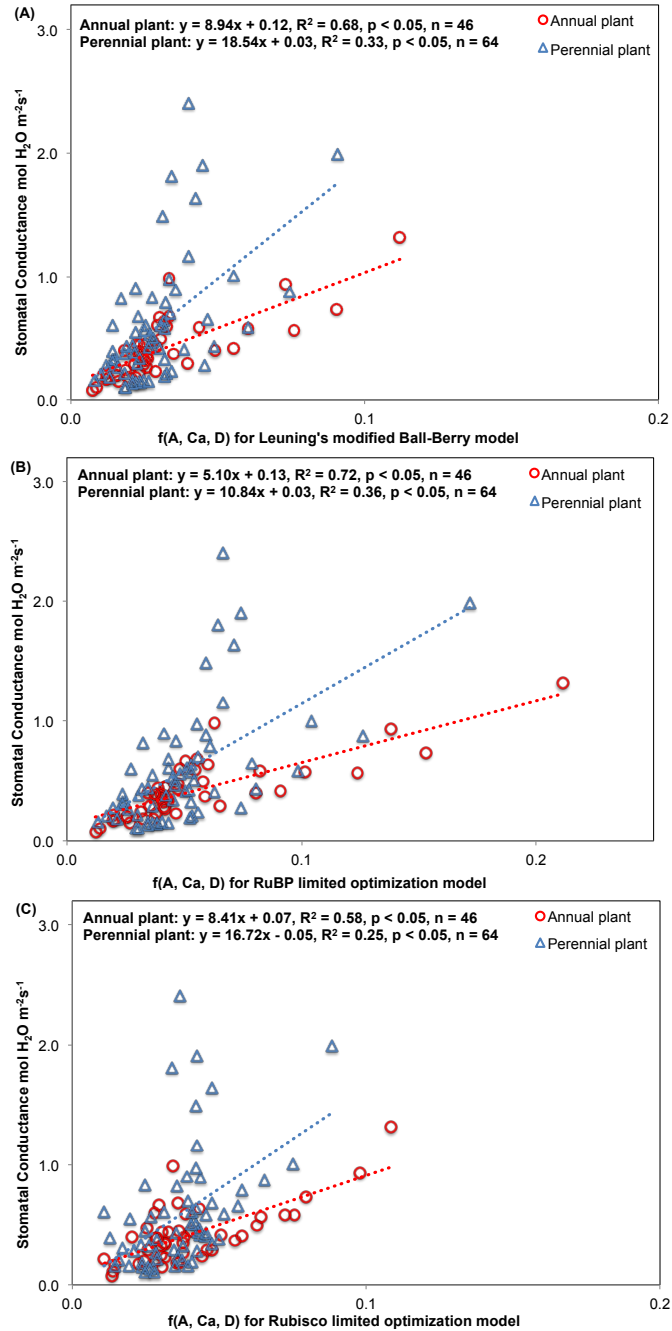


**Figure 3.4** The responses of stomatal conductance  $g_s$  as a function of  $C_a$ ,  $A$ , and  $D$  for different life forms (annual vs. perennial plant), for the Leuning's modified Ball-Berry model (A), RuBP limited optimization model (B), and Rubisco limited optimization model (C). The data are from semi-controlled measurements.



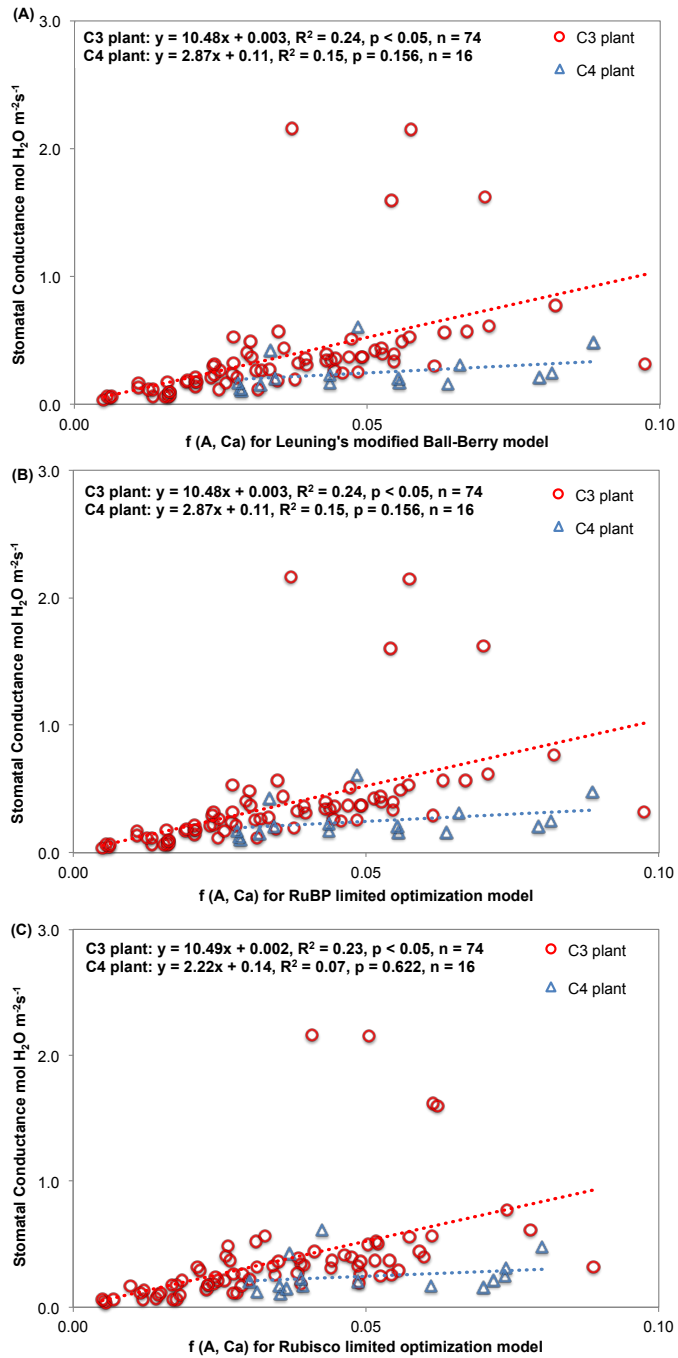


**Figure 3.5** The response of stomatal conductance  $g_s$  as a function of  $C_a$  and  $A$  for the Leuning's modified Ball-Berry model (A), RuBP limited optimization model (B), and Rubisco limited optimization model (C). The data are from FACE measurements.

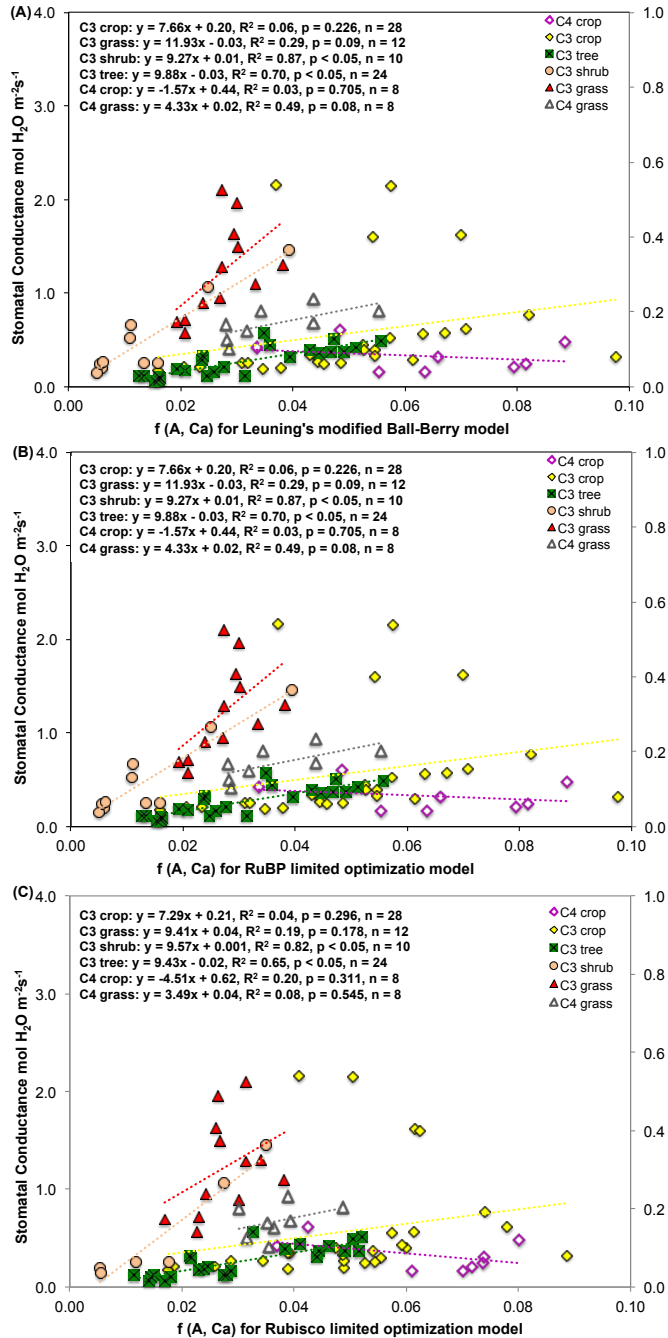


**Figure 3.6** The response of stomatal conductance  $g_s$  as a function of  $C_a$  and  $A$  for different functional groups, for the Leuning's modified Ball-Berry model (A), RuBP limited optimization model (B), and Rubisco limited optimization model (C). The data are from FACE measurements.

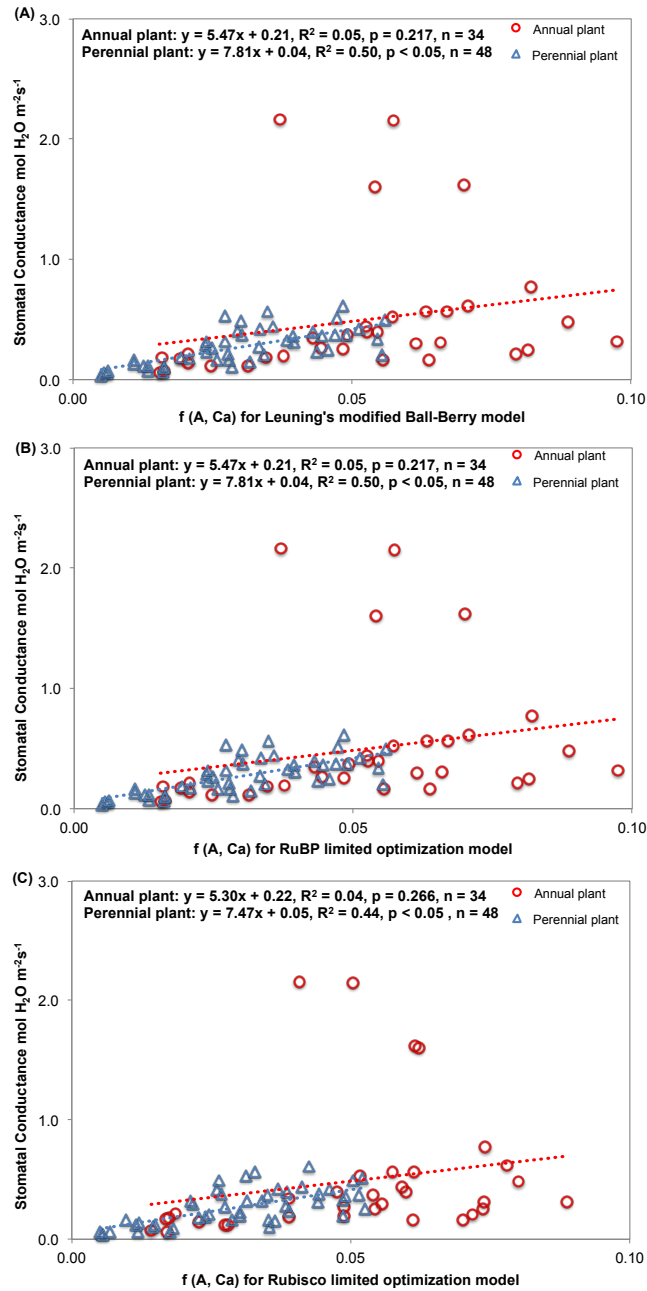


**Figure 3.7** The response of stomatal conductance  $g_s$  as a function of  $C_a$  and  $A$  for different life forms (annual vs. perennial plant), for the Leuning's modified Ball-Berry model (A), RuBP limited optimization model (B), and Rubisco limited optimization model (C). The data are from FACE measurements

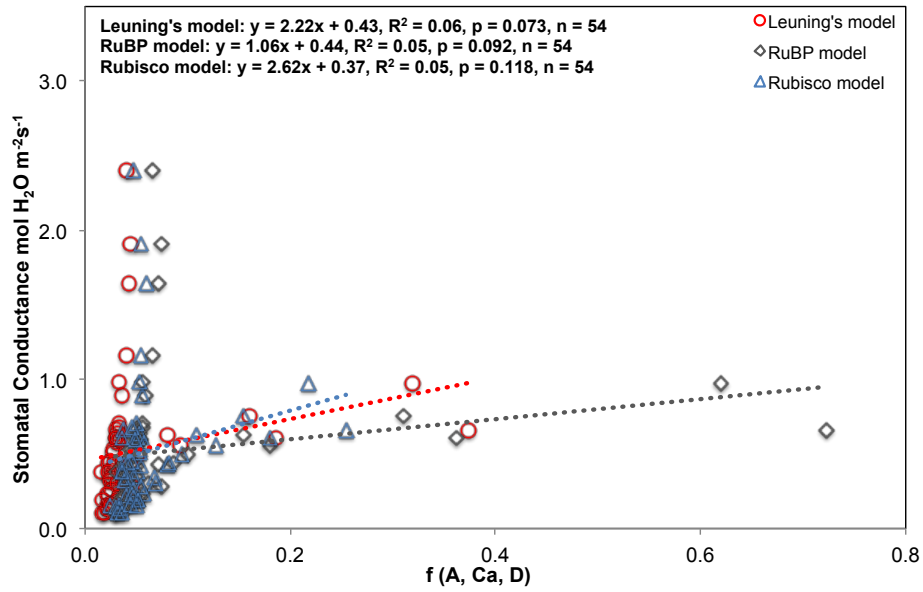


**Figure 3.8** Regression of stomatal conductance  $g_s$  as a function of  $C_a$ ,  $A$ , and  $D$  for the Leuning's modified Ball-Berry model (red open circles), RuBP limited optimization model (grey open squares), and Rubisco limited optimization model (blue open triangles). The data are from semi-controlled measurements in drylands.

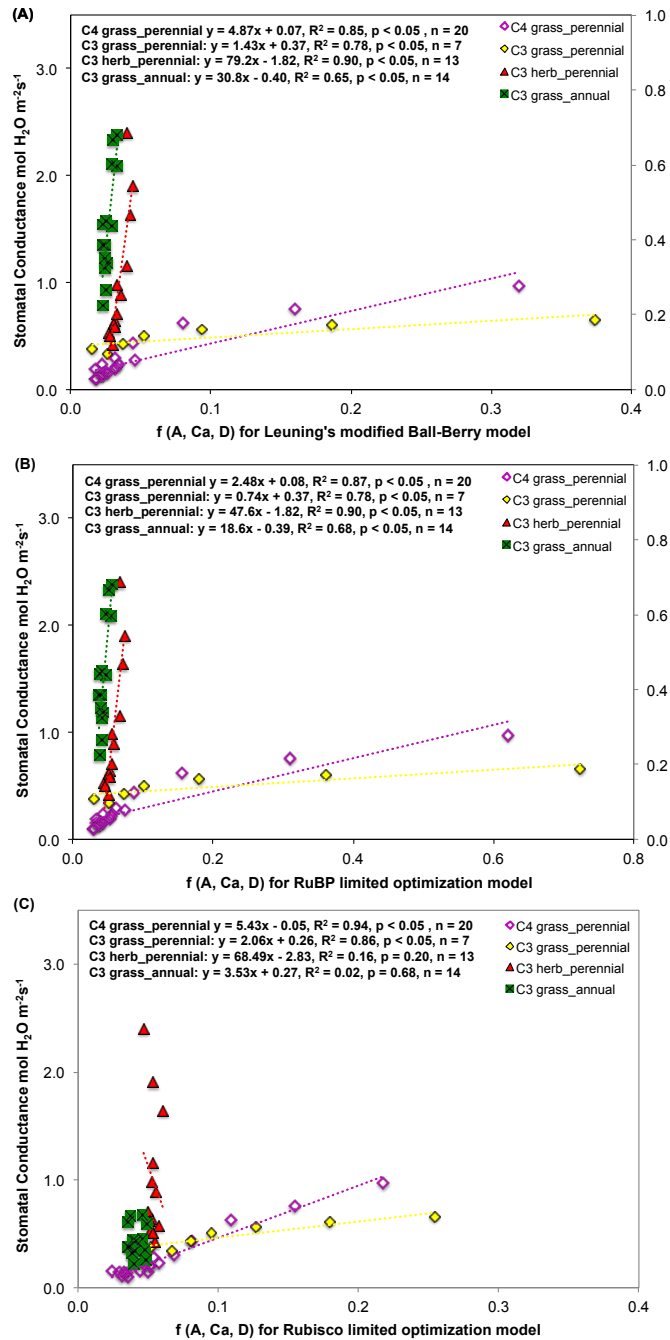


**Figure 3.9** The responses of stomatal conductance  $g_s$  as a function of  $C_a$ ,  $A$ , and  $D$  for different species and life form, for Leuning's modified Ball-Berry model (A), RuBP limited optimization model (B), and Rubisco limited optimization model (C). The data are from semi-controlled measurements in drylands.

## References

- Adams, H.D., Williams, A.P., Xu, C., Rauscher, S.A., Jiang, X., McDowell, N.G., 2013. Empirical and process-based approaches to climate-induced forest mortality models. *Frontiers in Plant Science*, 4.
- Ainsworth, E.A., Rogers, A., 2007. The response of photosynthesis and stomatal conductance to rising [CO<sub>2</sub>]: mechanisms and environmental interactions. *Plant, Cell & Environment*, 30(3): 258-270.
- Albertson, J.D., Kiely, G., 2001. On the structure of soil moisture time series in the context of land surface models. *Journal of Hydrology*, 243(1): 101-119.
- Anderson, L.J., Maherali, H., Johnson, H.B., Polley, H.W., Jackson, R.B., 2001. Gas exchange and photosynthetic acclimation over subambient to elevated CO<sub>2</sub> in a C<sub>3</sub>-C<sub>4</sub> grassland. *Global Change Biology*, 7(6): 693-707.
- Ball, J., Woodrow, I., Berry, J., 1987. A model predicting stomatal conductance and its contribution to the control of photosynthesis under different environmental conditions. In: Biggins, J. (Ed.), *Progress in Photosynthesis Research*. Martinus Nijhoff, Zoetermeer, Netherlands, pp. 221-224.
- Buckley, T.N., 2007. The role of stomatal acclimation in modelling tree adaptation to high CO<sub>2</sub>. *Journal of Experimental Botany*, 59(7): 1951-1961.
- Buckley, T.N., 2017. Modeling stomatal conductance. *Plant Physiology*, 174(2): 572-582.
- Buckley, T.N., Mott, K.A., 2013. Modelling stomatal conductance in response to environmental factors. *Plant, Cell & Environment*, 36(9): 1691-1699.

- Buckley, T.N., Mott, K.A., Farquhar, G.D., 2003. A hydromechanical and biochemical model of stomatal conductance. *Plant, Cell & Environment*, 26(10): 1767-1785.
- Collatz, G.J., Ribas-Carbo, M., Berry, J.A., 1992. Coupled photosynthesis-stomatal conductance model for leaves of C4 plants. *Functional Plant Biology*, 19(5): 519-538.
- Cowan, I.R., Farquhar, G.D., 1977a. Stomatal function in relation to leaf metabolism and environment. *Symposia of the Society for Experimental Biology* 31: 471-505.
- Cowan, I.R., Farquhar, G.D., 1977b. Stomatal function in relation to leaf metabolism and environment. *Symposia of the Society for Experimental Biology* 31: 471-505.
- Cox, P.M., Huntingford, C., Harding, R.J., 1998. A canopy conductance and photosynthesis model for use in a GCM land surface scheme. *Journal of Hydrology*, 212: 79-94.
- Damour, G., Simonneau, T., Cochard, H., Urban, L., 2010. An overview of models of stomatal conductance at the leaf level. *Plant, Cell & Environment*, 33(9): 1419-1438.
- Dewar, R.C., 2002. The Ball–Berry–Leuning and Tardieu–Davies stomatal models: synthesis and extension within a spatially aggregated picture of guard cell function. *Plant, Cell & Environment*, 25(11): 1383-1398.
- Emanuel, R., D'Odorico, P., Epstein, H.E., 2007. A dynamic soil water threshold for vegetation water stress derived from stomatal conductance models. *Water Resource Research*, 43: W03431, doi:10.1029/2005WR004831.

- Farquhar, G.V., von Caemmerer, V.S., Berry, J.A., 1980. A biochemical model of photosynthetic CO<sub>2</sub> assimilation in leaves of C<sub>3</sub> species. *Planta*, 149(1): 78-90.
- Field, C., Mooney, H., 1986. The photosynthesis-nitrogen relationship in wild plants. In: Givnish, T. (Ed.), *On the Economy of Plant Form and Function*. Cambridge, Cambridge University Press, pp. 25-55.
- Gao, Q., Zhao, P., Zeng, X., Cai, X., Shen, W., 2002. A model of stomatal conductance to quantify the relationship between leaf transpiration, microclimate and soil water stress. *Plant, Cell & Environment*, 25(11): 1373-1381.
- Ghannoum, O., Caemmerer, S.V., Ziska, L.H., Conroy, J.P., 2000. The growth response of C<sub>4</sub> plants to rising atmospheric CO<sub>2</sub> partial pressure: a reassessment. *Plant, Cell & Environment*, 23(9): 931-942.
- Harley, P.C., Thomas, R.B., Reynolds, J.F., Strain, B.R., 1992. Modelling photosynthesis of cotton grown in elevated CO<sub>2</sub>. *Plant, Cell & Environment*, 15(3): 271-282.
- Jacquemin, B., Noilhan, J., 1990. Sensitivity study and validation of a land surface parameterization using the HAPEX-MOBILHY data set. *Boundary-Layer Meteorology*, 52(1-2): 93-134.
- Jarvis, P.G., 1976. The interpretation of the variations in leaf water potential and stomatal conductance found in canopies in the field. *Philosophical Transactions of the Royal Society of London B: Biological Sciences*, 273(927): 593-610.



- Katul, G., Leuning, R., Oren, R., 2003. Relationship between plant hydraulic and biochemical properties derived from a steady- state coupled water and carbon transport model. *Plant, Cell & Environment*, 26(3): 339-350.
- Katul, G.G., Palmroth, S., Oren, R.A.M., 2009. Leaf stomatal responses to vapour pressure deficit under current and CO<sub>2</sub>- enriched atmosphere explained by the economics of gas exchange. *Plant, Cell & Environment*, 32(8): 968-979.
- Leuning, R., 1995. A critical appraisal of a combined stomatal-photosynthesis model for C<sub>3</sub> plants. *Plant, Cell & Environment*, 18: 339–355.
- Lloyd, J., Farquhar, G.D., 1994. 13-C discrimination during CO<sub>2</sub> assimilation by the terrestrial biosphere. *Oecologia*, 99(3-4): 201-215.
- Long, S.P., Ainsworth, E.A., Bernacchi, C.J., Davey, P.A., Morgan, P.B., Hymus, G.J., Osborne, C.P., 2006. Long-term responses of photosynthesis and stomata to elevated [CO<sub>2</sub>] in managed systems. Springer Berlin Heidelberg, pp. 253-270.
- Long, S.P., Drake, B.G., 1992. Photosynthetic CO<sub>2</sub> assimilation and rising atmospheric CO<sub>2</sub> concentrations. *Topics in Photosynthesis*, 12: 69-103.
- Lu, X., Wang, L., McCabe, M.F., 2016. Elevated CO<sub>2</sub> as a driver of global dryland greening. *Scientific Reports*, 6: 20716.
- Lugokencky, E.T., P. NOAA/ESRL. , 2017.

Available from: <http://www.esrl.noaa.gov/gmd/ccgg/trends>.

- Maherali, H., Reid, C.D., Polley, H.W., Johnson, H.B., Jackson, R.B., 2002. Stomatal acclimation over a subambient to elevated CO<sub>2</sub> gradient in a C<sub>3</sub>/C<sub>4</sub> grassland. *Plant, Cell & Environment*, 25(4): 557-566.
- Makela, A., Berninger, F., Hari, P., 1996. Optimal control of gas exchange during drought: theoretical analysis. *Annals of Botany* 77(5): 461–468.
- Manzoni, S., Vico, G., Katul, G., Fay, P.A., Polley, W., Palmroth, S., Porporato, A., 2011. Optimizing stomatal conductance for maximum carbon gain under water stress: a meta- analysis across plant functional types and climates. *Functional Ecology*, 25(3): 456-467.
- Medlyn, B.E., Duursma, R.A., De Kauwe, M.G., Prentice, I.C., 2013. The optimal stomatal response to atmospheric CO<sub>2</sub> concentration: Alternative solutions, alternative interpretations. *Agriculture and Forest Meteorology*, 182: 200-203.
- Medlyn, B.E., Duursma, R.A., Eamus, D., Ellsworth, D.S., Prentice, I.C., Barton, C.V., Wingate, L., 2011. Reconciling the optimal and empirical approaches to modelling stomatal conductance. *Global Change Biology*, 17(6): 2134-2144.
- Nowak, R.S., Ellsworth, D.S., Smith, S.D., 2004. Functional responses of plants to elevated atmospheric CO<sub>2</sub>—do photosynthetic and productivity data from FACE experiments support early predictions? *New Phytologist*, 162(2): 253-280.
- Rodriguez-Iturbe, I., Porporato, A., 2004. *Ecohydrology of water-controlled ecosystems: Soil moisture and plant dynamics*. Cambridge University, Cambridge, UK.

- Rodriguez- Iturbe, I., D'odorico, P., Porporato, A., Ridolfi, L., 1999. On the spatial and temporal links between vegetation, climate, and soil moisture. *Water Resources Research*, 35(12): 3709-3722.
- Sage, R.F., 2004. The evolution of C<sub>4</sub> photosynthesis. *New Phytol.*, 161: 341–370.
- Saxe, H., Ellsworth, D.S., Heath, J., 1998. Tree and forest functioning in an enriched CO<sub>2</sub> atmosphere. *New Phytologist*, 139: 395-436.
- Thornthwaite, C.W., Mather, J.R., 1955. The Water Balance. *Publications in Climatology*, 8(1): 1 – 104.
- Vico, G., Manzoni, S., Palmroth, S., Weih, M., Katul, G., 2013. A perspective on optimal leaf stomatal conductance under CO<sub>2</sub> and light co-limitations. *Agriculture and Forest Meteorology*, 182: 191-199.
- Yu, O., Goudriaan, J., Wang, T.D., 2001. Modelling diurnal courses of photosynthesis and transpiration of leaves on the basis of stomatal and non-stomatal responses, including photoinhibition. *Photosynthetica*, 39(1): 43-51.
- Yu, Q., Zhang, Y., Liu, Y., Shi, P., 2004. Simulation of the stomatal conductance of winter wheat in response to light, temperature and CO<sub>2</sub> changes. *Annals of Botany*, 93(4): 435-441.

**CHAPTER 4: A MULTI-SCALE ANALYSIS OF NAMIBIAN RAINFALL OVER  
THE RECENT DECADE – COMPARING TMPA SATELLITE ESTIMATES  
AND GROUND OBSERVATIONS**

**4.1 Abstract**

In many dryland regions, the lack of ground observations has long been a major obstacle in studying rainfall patterns, particularly in African where rainfall data is extremely scarce. In this study, a continuous 6-year (2008-2013) daily record of ground observations was collected from Weltevrede Farm at the edge of the Namib Desert. The ground observations were used to evaluate Tropical Rainfall Measuring Mission (TRMM) 0.25° daily satellite rainfall estimates of this area. The result showed the agreement between ground and satellite rainfall data was generally good at annual scales but large variations were observed at daily scales. Then we conducted a Mann-Kendall trend analysis using bias-corrected annual satellite data (1998-2013) to examine long-term patterns in rainfall amount, intensity, frequency and seasonal variations over four locations across a rainfall gradient. The trend analyses showed there were significant changes in frequency, but insignificant changes in intensity and no changes in total amount for the driest location. No changes were found in total rainfall, intensity or frequency among another three locations, which emphasized the spatial variability of dryland rainfall. Contrary to IPCC prediction of drying trend in Namibia, our trend analysis did not reveal any significant changes in rainfall amount from any site over the recent decade, but frequency changes were observed in the driest location.

## 4.2 Introduction

Rainfall is one of the main components of hydrologic cycle and the major source of water for natural vegetation as well as agriculture and livestock production in dryland regions (Wang and D'Odorico, 2008). About 90% of the world's dryland population is in developing countries (Wang et al., 2012), where the vast majority of drylands consist of rangelands (Millennium Ecosystem Assessment, 2005) (i.e., 69%). Dryland rangelands support approximately 50% of the world's livestock and its production is particularly vulnerable to climate variability, of which rainfall is the most important component (Millennium Ecosystem Assessment, 2005). African rangelands are of critical importance since they cover 43% of Africa's inhabited surface and are home to 40% of the continent's population (AU-IBAR, 2012). Though the proportion of rainfed cropland is not as significant as rangeland, rainfed agriculture is most prominent in some regions of Africa such as Sub-Saharan Africa where more than 95% of the cropland is rainfed (Rockström et al., 2010). Changes in rainfall amount, intensity and rain patterns could significantly affect dryland agriculture leading to decreased resource productivity and production (Daryanto et al., 2016). Erratic rainfall patterns in Nigeria, for example, made it difficult for farmers to plan their operations and resulted in low germination in cropping season, reduced yield and crop failure (Oriola, 2009). Study of maize production in Zimbabwe also indicated that more accurate climate predictions would be valuable in crop management decisions in that it reduced risk in agricultural production associated with rainfall variability at the site level (Phillips et al., 1998).

However, most areas of Africa lack sufficient observational data to study long-term rainfall trend and variability. Apart from the scarcity of data, an additional complication is that, in many regions of Africa, discrepancies exist between different observed rainfall data sets (Barros, 2014). Intergovernmental Panel on Climate Change (IPCC) has predicted a likely decrease in annual rainfall over parts of the western and eastern Sahel region in northern Africa as well as a likely increase over parts of eastern and southern Africa during the period of 1951–2010 (Barros, 2014). Particularly, a reduction in late austral summer rainfall has been observed and projected over western parts of southern Africa extending from Namibia, through Angola, and towards Congo during the second half of the 20th century (Barros, 2014). As shown in the IPCC AR5, signal of future change in precipitation is not obvious (less agreement) until the middle of the 21st century over southern Africa. IPCC prediction using General Circulation Models (GCMs) is run at a coarse spatial resolution of 150–300 km while the rainfall process has a much higher spatial variability, and thus high-resolution data is needed for better prediction. IPCC prediction has great uncertainty and ground data is therefore very important to constrain the model prediction for the future.

Rain gauges have historically been considered the most accurate form of local rainfall measurement (Villarini et al., 2009). However, they can only capture the variability of small areas and therefore in many cases, precipitation estimates from rain gauges are subject to uncertainty when representing the entire observation site. Errors and omissions or power outages from the recording devices, human operators, and data transmission

could also cause valuable data to be lost, damaged, or altered and result in poor data quality (Kneis et al., 2014). In many regions of the world, rain gauge data is difficult to access due to technical or administrative reasons (Kneis et al., 2014). Particularly in many remote parts of developing countries, ground-based rainfall measurements are rare or nonexistent. Radar and satellite-based rainfall estimates have been shown to provide a potential solution to the limitations of rain gauge data (Ward and Trimble, 2003). But satellites do not measure rainfall directly, so combining of ground observations with radar and satellite remote sensing of rainfall estimates could be a viable approach to produce a consistent, long sequence of climate data records (Villarini et al., 2009).

Although previous studies have documented some characteristics of Namibia rainfall (Eckardt et al., 2013), rarely have they looked at how well satellite-based rainfall data is correlated with ground-based observations. More importantly, no attempt has been made to comprehensively analyze the long-term changes in rainfall in Namibia, where the rainfall is highly variable both spatially and temporally with the greatest rainfall variation coefficient over Southern Africa (Eckardt et al., 2013). A normal rainy season spans from October to April (Foissner et al., 2002), and October, as the transition month from dry season to wet season, is characterized by very high inter-annual rainfall variability (Eckardt et al., 2013). There hasn't been a rainfall observation site from the Namibia Meteorological Services at the edge of the Namib Desert, so the ground rainfall measurements from this region are very valuable. Moreover rainfall in this region could be highly localized with large inter- and intra- annual variation as the area is located right on

the steep rainfall gradient from the desert interior to the Namibian highland (Eckardt et al., 2013; Kaseke et al., 2016). As a result of strong the NE-SW rainfall gradient across, Southern Africa rainfall events mainly occur in the north-eastern, northern and central parts, and the southern parts of Namibia are largely hot and dry having only isolated rainfall occurrences, and ultimately the west Namib coast is hyper-arid (Eckardt et al., 2013). Therefore, another focus of this study is to evaluate the rainfall pattern changes at different locations along the rainfall gradient; and for each location, the detailed rainfall trend analyses will be conducted (e.g., total rainfall trend, rainy season rainfall trend, the average rainfall depth per storm, and the average storm frequency).

In this study, we compared the Tropical Rainfall Measuring Mission (TRMM) Multi-satellite Precipitation Analysis (TMPA) satellite data with available ground observations from the local rain gauges. The TMPA satellite estimates were then used to resolve the spatial and temporal distributions of rainfall over the study area. TMPA satellite is a US-Japan joint mission launched in November 1997 (Simpson et al., 1988), and its primary goal is to measure precipitation in the Tropics where surface observations are scarce (Bowman, 2005). It operates in a low-inclination ( $35^\circ$ ), low-altitude orbit (Bowman, 2005), and the primary merged microwave-infrared product is computed at finer scale with the 3-h,  $0.25^\circ \times 0.25^\circ$  latitude–longitude resolution (Huffman et al., 2007). In this study, we aim to address the following questions: 1) are satellite based rainfall data useful to study the rainfall characteristics at regions with the lack of ground observations traditionally? 2) if so, what are the temporal scales at which the satellite rainfall data are comparable with



ground observations? and 3) are there any significant long-term changes in rainfall characteristics over multiple locations in Namibia across a rainfall gradient?

### **4.3 Methods**

To examine the spatial variations and assess the long-term rainfall trends as well as long-term rainfall variability, we analyzed TMPA rainfall estimates from four locations across a rainfall gradient (Figure 4.1). The four locations are Farm 1 and Farm 2 within the Weltevrede Guest farm, the Gobabeb Research and Training Center (GRTC, TMPA pixel centered at 23.625°S, 15.125°E) located within hyper-arid Namib Desert (long-term annual average rainfall <60 mm) (NMS, 2015), and Windhoek (WDH, TMPA pixel centered at 22.625S°, 17.125E°) that is subject to a long-term annual average rainfall up to 400 mm (NMS, 2015). The time period covered is January 1, 1998 to December 31, 2015 (17 years) and TRMM mission ended in April 2016. A summary of TMPA satellite rainfall data for the above-mentioned four locations was provided in Appendix D.

In the Weltevrede Guest Farm site, we have ground rainfall records at two locations for validation of TMPA data. The Weltevrede Guest Farm is located in the escarpment of the southern Namib Desert, and is characterized by semi-desert and savanna transition in biomes (Foissner et al., 2002). The farm is next to the road C 19, around 300 kilometers southwest of Windhoek, and bordered on three sides by the Namib Naukluft Park (24°10'S, 15°58'E, Elev. 1087 m) (Figure 4.1). It is nestled amidst rugged mountains, shifting dunes, harsh gravel plains, dusty prehistoric riverbeds and camelthorn trees. The farm covers an area of about 11.6 km<sup>2</sup> and there are two local rain gauges situated at Farm House (Farm 1)

and Brine Tank (Farm 2), respectively (Figure 4.1). Most of the rain falls in summer, and only very rare rainfall occurs through the winter. The two rain gauges within the Weltevrede Guest Farm are the only two sites with available ground records to validate the TMPA data. A major limitation is that although the ground observations collected from the Weltevrede Farm are likely very reliable since local farmers tend to take rainfall measurements faithfully, we have to assume they are the “correct” values. A similar approach has been used in other data scarce regions, such as the central Kenyan highlands (Franz et al., 2010).

This study uses version 7 of the TMPA 3B42 data product with a spatial resolution of  $0.25^\circ \times 0.25^\circ$  ( $\sim 25$  km) at the finest scale of 3-h interval (Huffman et al., 2007). The raw TMPA data was averaged into daily time-scale to match the ground record. For the Weltevrede Guest Farm, Farm 1 is located within the TMPA pixel centered at  $24.125^\circ\text{S}$  and  $15.875^\circ\text{E}$ ; and Farm 2 is within the immediate next pixel ( $24.125^\circ\text{S}$ ,  $16.125^\circ\text{E}$ ). The quality of TMPA rainfall estimates was evaluated by comparing 6-year daily, monthly and annual data with ground observations from rain gauges at Farm 1 and Farm 2 shown in Figure 4.1. Furthermore, the cumulative distribution functions (CDFs) of TMPA rainfall data and ground observations were compared.

Rainfall trends were analyzed using non-parametric rank based statistical test, namely Mann-Kendall (MK) test to detect monotonic trends. The MK test has been widely used to assess the significance of trends in hydro-metrological time series including

rainfall. Based on the null distribution of the MK test, the critical regions of the MK statistic  $S$  can be approximately given by

$$|S| > z_{1-\beta/2} \sqrt{V(S)}, \quad (1)$$

where  $\beta$  is the preselected significance level,  $z_{1-\beta/2}$  are the  $1 - \beta/2$  quantile's of the standard normal distribution, and  $V(S)$  is the sample variance of the MK statistic  $S$ . In this study, the significance level  $\alpha$  is set to be 0.05. In this study, besides the total rainfall amount, we also analyzed the temporal trends of two important hydrological parameters decomposed from the total rainfall: the average rainfall depth per storm,  $\alpha$  (mm), and the average storm frequency or average inter-storm arrival rate,  $\lambda$  (day<sup>-1</sup>) using the Mann-Kendall statistical test (Franz et al., 2010).

Three measures of the rainfall variability in annual rainfall were analyzed including the standard deviation, the coefficient of variation (CV), and precipitation variability index (PVI). PVI is a new dimensionless index defined as the standard deviation of the ratio ( $R_i$ ) between a time series of cumulative precipitation measurement ( $C_i$ ) and a time series of cumulative mean precipitation rate ( $E_i$ ) (Gu et al., 2014) (Eq. (2)). From the measured daily precipitation  $p_j$ , a time series of cumulative rainfall  $C_i$  (Eq. (4)) and mean precipitation rate  $\bar{p}$  (Eq. (5)) were computed. The time series of cumulative mean  $E_i$  then were computed based on mean precipitation rate  $\bar{p}$  (Eq. (6)), and  $R_i$  is the ratio of the cumulative precipitation to the cumulative mean (Eq. (3)).  $\bar{R}$  is the average of  $R_i$  over  $n$ . Study shows that PVI can simultaneously capture the characteristics of both intensity distribution and event spacing of precipitation, whereas

the commonly used index such as CV can only quantify intensity distribution (Gu et al., 2014).

$$PVI = \sqrt{\frac{\sum_{i=1}^n (R_i - \bar{R})^2}{n}}, \quad (2)$$

where

$$R_i = \frac{C_i}{E_i}, \quad (3)$$

$$C_i = \sum_{j=1}^i p_j, \quad i = 1, \dots, n, \quad (4)$$

$$\bar{p} = \frac{\sum_{i=1}^n p_i}{n}, \quad (5)$$

$$E_i = i\bar{p}, \quad i = 1, \dots, n, \quad (6)$$

## 4.4 Results and discussion

### 4.4.1 TMPA data validation using two ground gauges

A significant issue with comparing satellite and rain gauge data is that the satellite data are estimates of area-averaged precipitation amount while rain gauges make point measurements (Bowman, 2005). For example, TMPA might observe rainfall in the area surrounding a rain gauge while it is not raining at the gauge itself. Conversely, the gauge sometimes observes a localized heavy rainfall, but TMPA tends to average the localized high measurements with the nearby lower measurements in order to obtain the area-averaged estimates, and consequently reduce the reliability of data. Prior to using TMPA satellite data to study long-term rainfall patterns in the studied areas, it is therefore necessary to make quantitative estimates on how well the TMPA data represents rainfall characteristics as compared to ground observations. In this study, data from two locations

(Farm 1 and Farm 2 rain gauges) were used to evaluate the TMPA retrievals at daily, monthly, and annual time scales.

TMPA data was compared with *in-situ* rain gauge measurements for a 6-year evaluation period from 1 January 2008 to 31 December 2013. Figure 4.2 shows results of the evaluation for Farm 1 and Farm 2. The performance of the satellite data varies between the two locations, and generally, the bias of the satellite data in measuring daily mean values is larger than that of monthly and annual values. The results showed that the monthly and annual estimates correlate relatively well for both locations with  $R^2$  of 0.47–0.64 (Figure 4.2), with the daily estimates having the lower agreements ( $R^2 = 0.24$ –0.25). Our  $R^2$  values were lower than other studies conducted in wetter environments such as the La Plata Basin in South America (Su et al., 2008), and the Upper Midwest and far Northeast over the United States (Ebert et al., 2007). In general, at daily time scales, there were a number of high intensity rain days (e.g., 30 mm day<sup>-1</sup>) on which rainfall was considerably higher for ground observations relative to TMPA data. The opposite was observed on a number of low intensity rain days (e.g., <10 mm day<sup>-1</sup>) on which the rainfall was considerably higher for TMPA data relative to ground observations.

The rainfall pattern of rain gauge Farm 2 was generally well reproduced by TMPA data, with a slope of 0.94 and 1.02 at monthly and annual scales, respectively (Figure 4.2). However, the satellite data tended to slightly underestimate the mean precipitation amount at Farm 1 (Figure 4.2). Satellite data averages the estimates of rainfall amount over a 25 × 25 km area, which may induce bias by averaging localized high measurements with

nearby lower measurements. According to the Namibia Meteorological Services (NMS, 2015), total rainfall is the lowest along the arid west coast, increasing towards the east and north, with extreme variability experienced across the central and northern Namibia (Eckardt et al., 2013). The Weltevrede Guest Farm is located across a steep rainfall gradient from the desert interior to the Namibian highlands, with the eastern part less arid than the hyper-arid western part. This may be responsible for the mismatch between Farm ground observations and satellite data.

Figure 4.3 shows the CDF comparisons for daily, monthly and annual rainfall at Farm 1 and Farm 2. As seen from Figure 4.3, the ground observation CDFs for Farm 1 generally agreed well with the TMPA data, but the discrepancy became larger for Farm 2 data, particularly at annual scale. A close examination showed that the Farm 2 gauge is allocated to the TMPA pixel immediately next to Farm 1. However, the Farm 2 gauge is actually located at the edge of two pixels and thus may be influenced by its neighboring pixels. This point is illustrated in Figure 4.9 that shows the CDFs for ground observations from Farm 2 were closer matched to TMPA data from the same pixel as Farm 1. So considering the results from both scatter-plots (Figure 4.2) and CDF analyses (Figure 4.3), using the uncorrected TMPA data for the trend analysis is a viable approach without introducing additional bias.

In this study, two factors limit the amount of data available for our analysis; one is the relatively short period for which the TMPA rainfall estimates are available (17 years because TRMM mission ended in April 2016), and the other is the limited availability of

rain gauge data. A previous study has found that the gaps in the data available at the NMS are serious enough to place the required level of confidence in the analysis results in doubt (Ministry of Agriculture, 1999). Therefore the ground observations that we collected from Weltevrede Farm could help improve the rainfall analysis in this region. In addition, although the number of rain gauge is limited in this study, our validation results are in agreement with other studies that indicate even if the network density is high, TMPA achieves reasonable performance at monthly scale but not at daily time scales (Ebert et al., 2007; Huffman et al., 2007; Su et al., 2008).

#### **4.4.2 Mann-Kendall trend analysis**

Namibia's climate is characterized by hot and dry spells with scarce and unpredictable rainfall, and is second in aridity only to the Sahara within Africa (Foissner et al., 2002). The combination of a cold, subantarctic upwelling ocean current on the Atlantic coast and a hot subtropical interior have led to 69% of the country being semi-arid, and 16% being arid, where the average rainfall of under 250 mm per year is coupled with annual mean evaporation of up to 3700 mm (Foissner et al., 2002). Besides, the rains have been erratic in recent years with many parts of country enduring severe drought, which poses a threat to rangeland owners and crop farmers (Haeseler, 2013).

Trend analyses were conducted for both annual and rainy-season rainfall for total rainfall, frequency ( $\lambda$ ), rainfall intensity ( $\alpha$ ) and rainfall variability parameters. Annual rainfall did not show any significant trend for all the four locations (Figure 4.4). However, some location differences in the patterns of trends were observed for the  $\alpha$  and  $\lambda$

parameters. There was a significant decreasing trend for  $\lambda$  ( $p = 0.006$ , Figure 4.4), along with increasing trend for  $\alpha$  at GRTC, which is located in the hyper-arid central Namib subject to a mean annual rainfall of about 20 mm per year. The changes in rainfall frequency became less significant at Farm 1 ( $p = 0.733$ , Figure 4.4) and Farm 2 ( $p = 0.383$ , Figure 4.4) where the mean annual rainfall was much more than that of the Namib Desert. There was no significant change in either frequency or rainfall intensity at Windhoek ( $p > 0.05$ , Figure 4.4), the wettest station among the four stations. Trend analyses of all the rainfall variability parameters (standard deviation, coefficient of variation, and precipitation variability index) did not reveal significant change in any of the locations for the annual rainfall ( $p > 0.05$ , Figure 4.6) except for the coefficient of variation of GRTC with increased variability.

The spatial patterns of trends in total rainfall, frequency and rainfall intensity for rainy season were similar to those for the annual ones. A decreasing trend in  $\lambda$  and increasing trend in  $\alpha$  was observed at GRTC; the changes were significant in frequency ( $\lambda$ ) ( $p = 0.019$ , Figure 4.5), but not in intensity ( $\alpha$ ) ( $p > 0.05$ , Figure 4.5). The total rainfall,  $\alpha$  and  $\lambda$  did not change significantly in either Farm sites or Windhoek station ( $p > 0.05$ , Figure 4.5).

Although IPCC's model projection has found there is likely a drying trend in annual average rainfall over mid to late 21st century (with large uncertainty), our trend analysis did not show any significant changes in total rainfall amount for all sites over the period of 1998 to 2015. Even though our TMPA rainfall estimates were limited to a



relatively short period, the TMPA data have a much finer spatial resolution than those of GCMs for IPCC predictions.

#### **4.4.3 Rainfall seasonality and erratic rain pattern with extreme rainfall events and droughts**

Typically there are two seasons in Namibia: cool and dry winter (May to September), and hot and rainy summer (October to April). Rainfall in all the four locations was highly seasonal in occurrence, with 99% or more of the annual rains occurring during the rainy season. More than 55% of the annual rains fell in late summer – February, March, and April but was highly dependent on location. The lowest proportion was seen in Windhoek (55%), which had the highest total annual rainfall, while the other three locations saw more than 65% of the annual rains during the late summer period.

The seasonality pattern derived from TMPA data showed the total rainfall was generally higher in February but with greater inter-annual variation (Figure 4.7). There were two rainfall peaks during the rainy season: the strong one in February or March, and the weak one in the early summer (November or December). These summer rainfall peaks are most likely associated with Tropical Temperate Troughs (TTTs), the most significant southern African summer rainfall producing systems that link an easterly wave in the tropics to a westerly wave in the south through a trough and cause cloud band and precipitation (Eckardt et al., 2013; Kaseke et al., 2016). Moreover, a reduction has been reported in late austral summer precipitation (February-March-April (FMA) response)

associated with an upward trend in tropical Indian Ocean sea surface temperature (SST) (Hoerling et al., 2006; New et al., 2006). Our trend analysis, however, did not show any significant changes in late summer precipitation at any of the sites (Figure 4.8).

The results showed an increase in extreme precipitation such as heavy rainfall and drought over our study area. Particularly, the extreme rainfall events seemed to increase in recent years with higher monthly peak rainfall amount in February, and more storm events in the peak month. In addition, the 2013 drought of Namibia has been captured in both rain gauge data and TMPA satellite rainfall estimates, which is consistent with the findings from NMS that reported the rainy season from October 2012 to April 2013 was very dry over the north, middle and the south of the country. The increased frequency of major storms caused damage to farmland, crops and livestock, as well as the roads. In the 2013 drought of Namibia, for example, water shortage during the main cropping season (November to June) resulted in the death of several thousand livestock and crop failure, and severely affected the local agrarian economy (Haeseler, 2013).

#### **4.5 Conclusions**

In this study, we evaluated the feasibility of utilizing satellite-based rainfall estimates for examining the changes in rainfall patterns in data scarce dryland regions. The TMPA satellite data were evaluated against the ground observed rain gauge data. In general, the TMPA estimates agreed well with the rain gauge data at monthly and annual time scales. The agreement between TMPA and gauge precipitation estimates became

lower at daily time scale, particularly for high intensity rain ( $>30 \text{ mm day}^{-1}$ ) and low intensity rain ( $<10 \text{ mm day}^{-1}$ ).

One of the most important findings from this study is the difference in trends of rainfall amount, frequency and intensity between drier and wetter regions. In a very arid and hot GRTC area, though the total rainfall amount does not change, there is a decrease (significant) in frequency ( $\lambda$ ) of storm accompanied by an increase (non-significant) in storm intensity ( $\alpha$ ). However, neither of these two indices shows significant changes at Windhoek, a much wetter site. The Weltevrede Farm, as located in the transition zone from the dry Namib Desert to less arid highland (Windhoek), shows less significant results compared to GRTC. The results also show increased rainfall variability for the driest location as indicated by the increasing trend of coefficient of variation. In addition, the long-term rainfall pattern and late summer precipitation (FMA response) based on TMPA satellite derived rainfall dataset, are contrary to the IPCC predictions (with large uncertainties) of a drying trend in Namibia, again emphasizing the spatial variability of dryland rainfall and the necessity of obtaining ground observations in data scarce regions. This study provides rare long-term ground observations of rainfall record at a daily scale from a data scarce region. More importantly, this study provides a useful approach of using annual TMPA data associated with trend analysis to facilitate the understanding of temporal and spatial rainfall variations in the areas of Africa where the in situ observations are scarce.

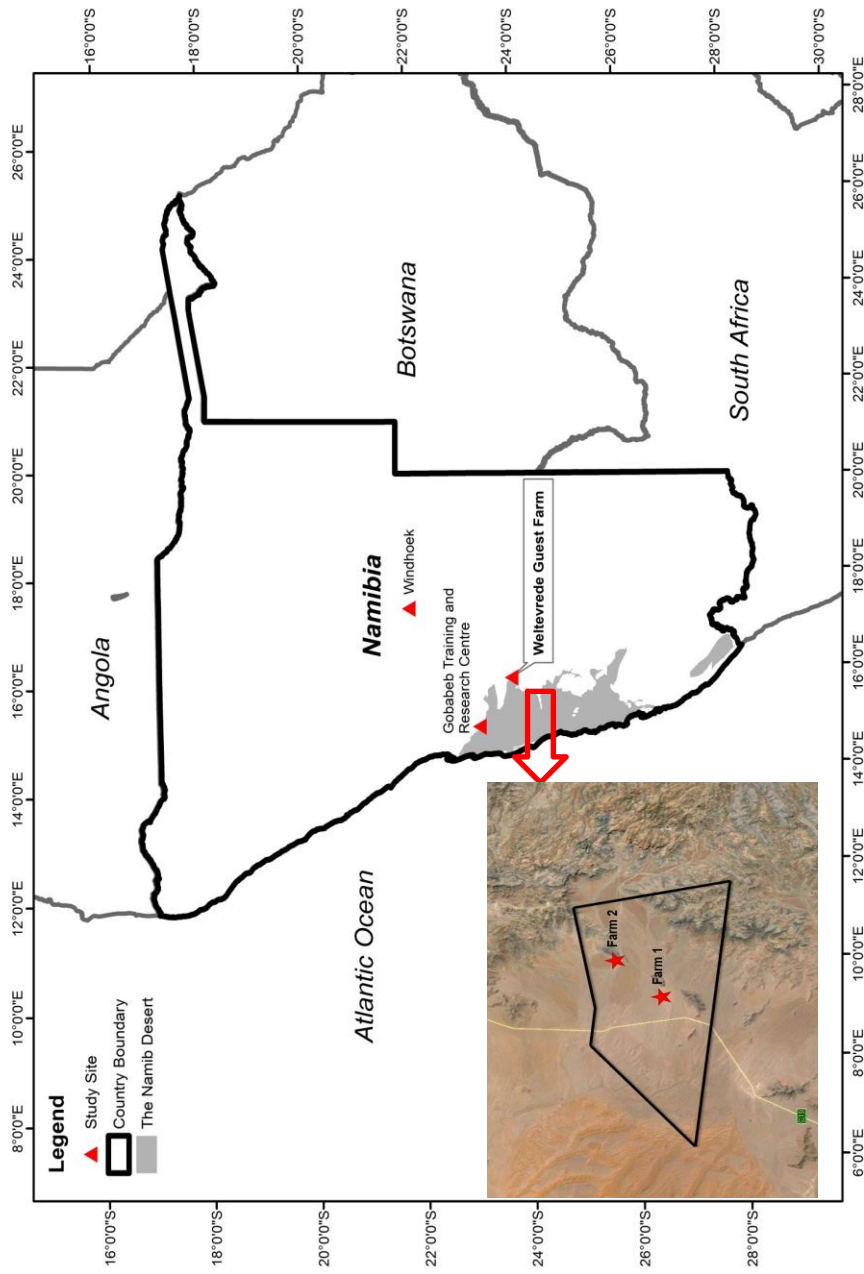


**Figure 4.1** Locations of the Weltevrede Farm (Farm 1 and Farm 2), Gobabeb Research and Training Center (GRTC), Windhoek (WDH) and the surface rain gauges. Black lines indicate the boundary of the Weltevrede Farm. The map was generated using ArcGIS for Desktop 10.3.1 (<http://www.arcgis.com>).

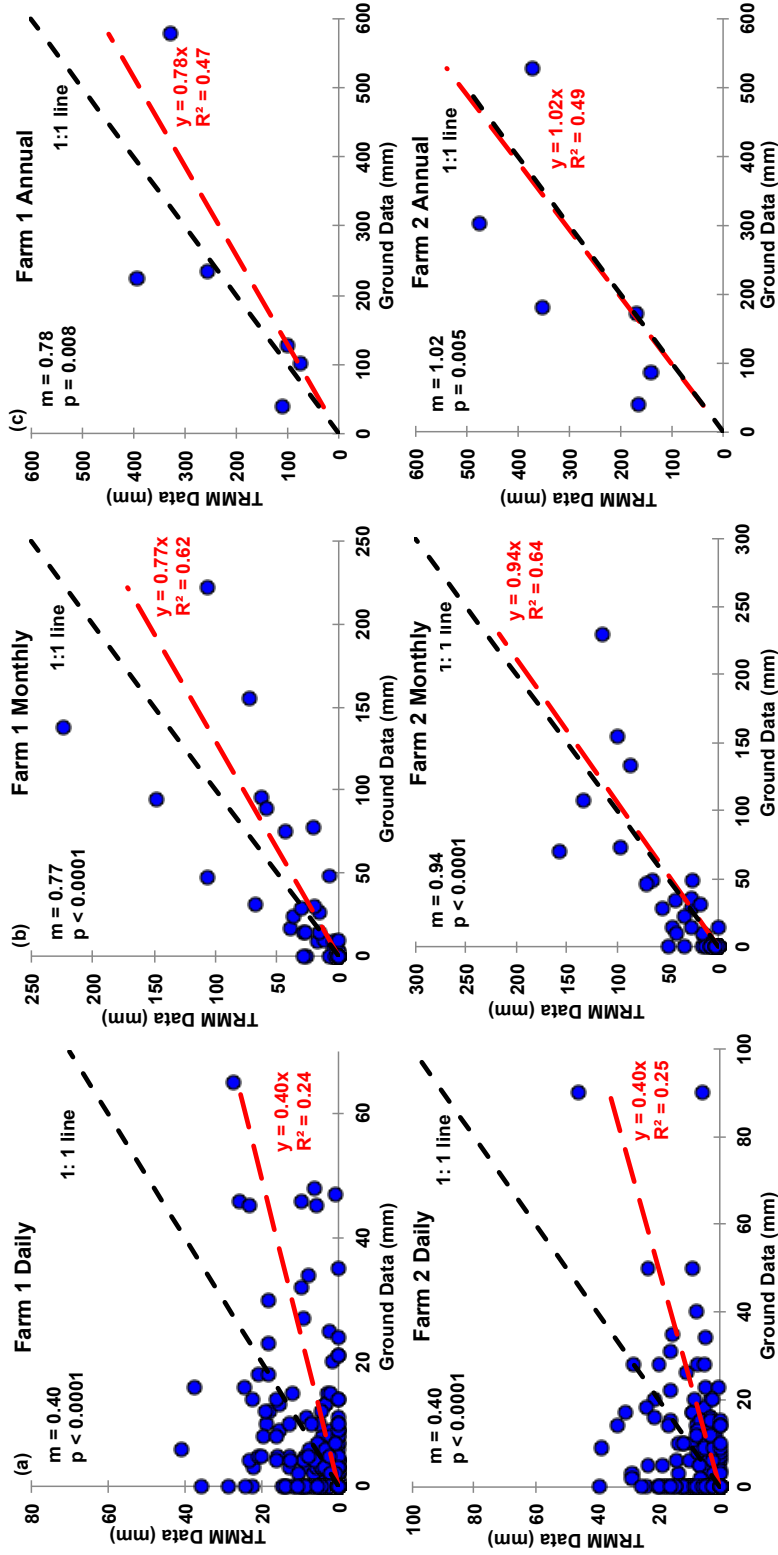


**Figure 4.2** Data validation of Tropical Rainfall Measuring Mission Multi-satellite Precipitation Analysis (TMPA) data set. Scatter plots of daily (a) ( $n = 2192$ ), monthly (b) ( $n = 72$ ), and annual (c) ( $n = 6$ ) rainfall from TMPA and gauged estimates at Farm 1 (Top Panel) and Farm 2 (Bottom Panel) for the period of January 1, 2008 to December 31, 2013.  $m$  is the slope coefficient.

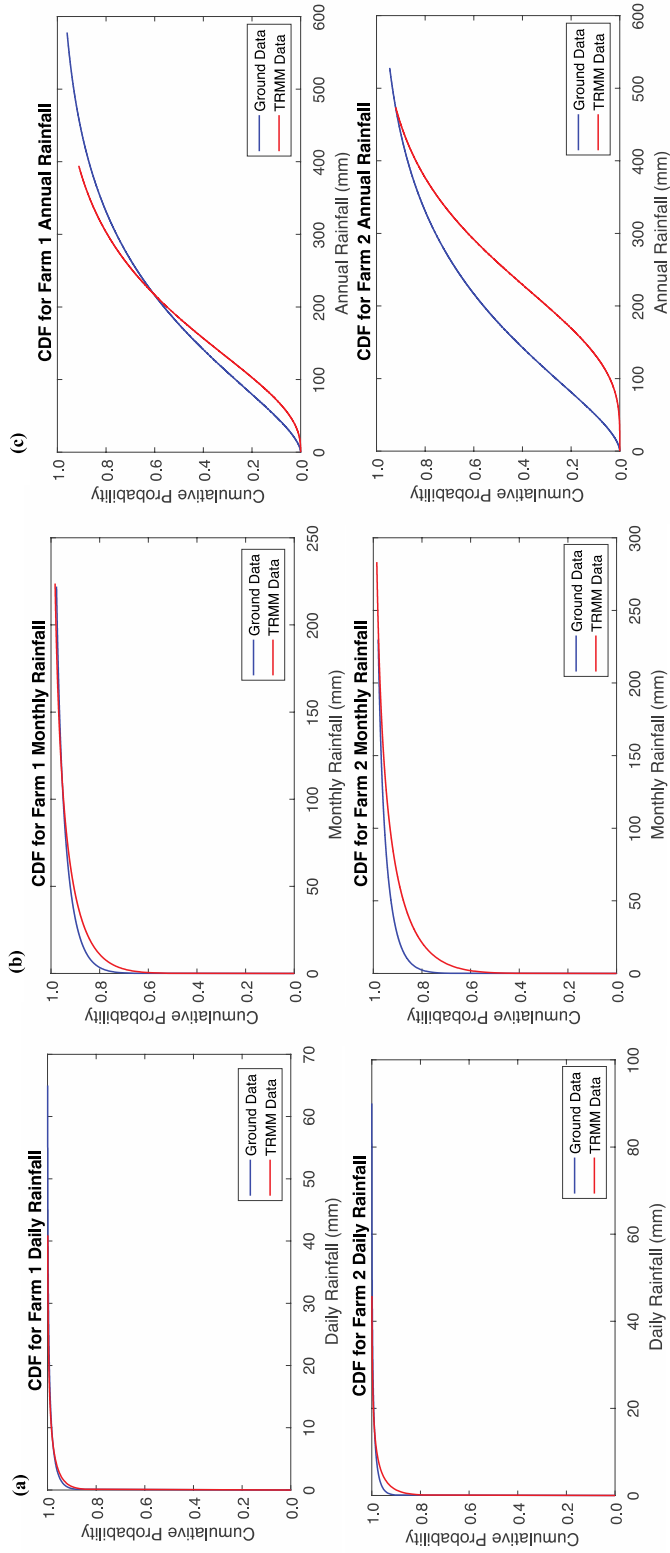


**Figure 4.3** Cumulative distribution functions (CDFs) of daily (a), monthly (b), and annual (c) rainfall from Tropical Rainfall Measuring Mission Multi-satellite Precipitation Analysis (TMPA) and gauged estimates at Farm 1 (Top Panel) and Farm 2 (Bottom Panel) for the period of January 1, 2008 to December 31, 2013.

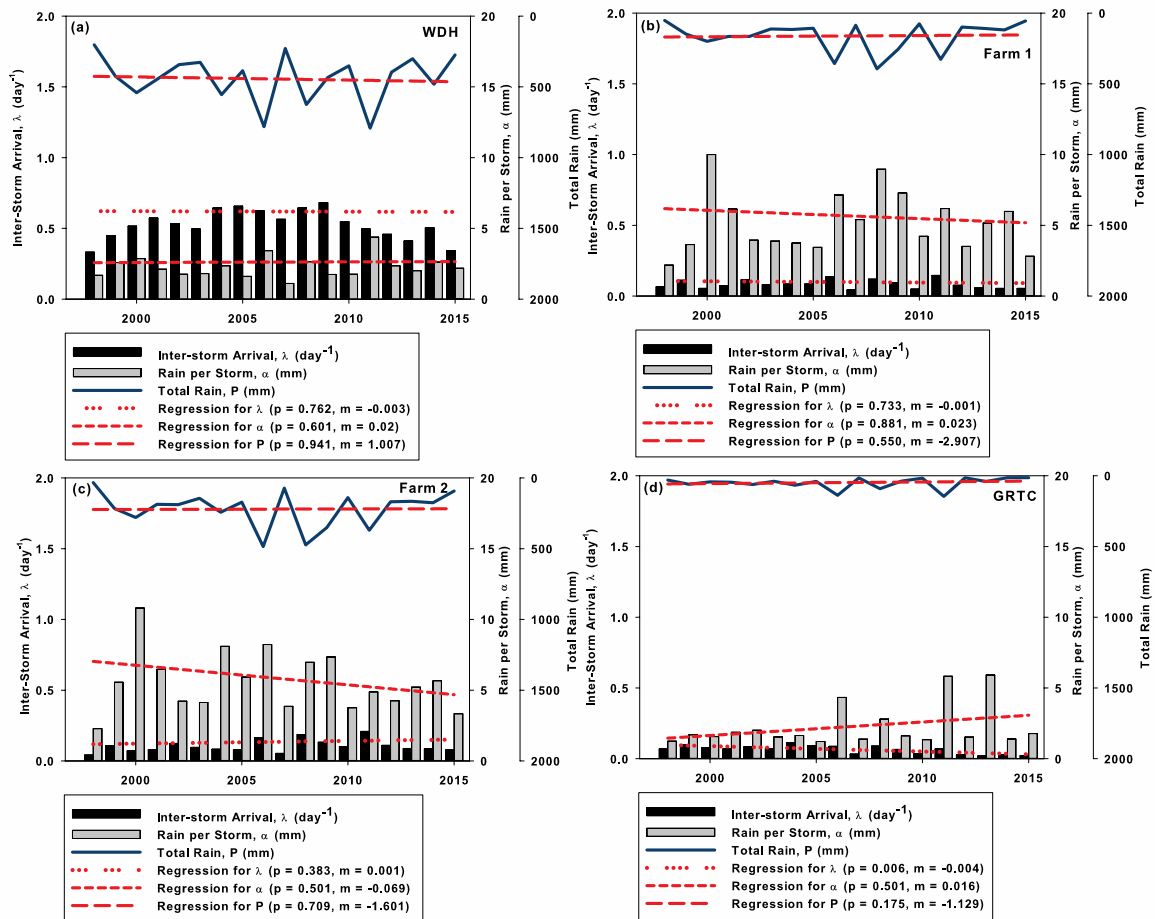


**Figure 4.4** Time series of annual rainfall (mm), average rain depth per storm (mm)  $\alpha$ , and the average storm arrival rate ( $\text{day}^{-1}$ )  $\lambda$  for (a) Windhoek (WDH), (b) Weltevrede Farm Location 1 (Farm 1), (c) Weltevrede Farm Location 2 (Farm 2), and (d) Gobabeb Research and Training Center (GRTC). Record length = 17 years, and  $m$  = Sen's slope.

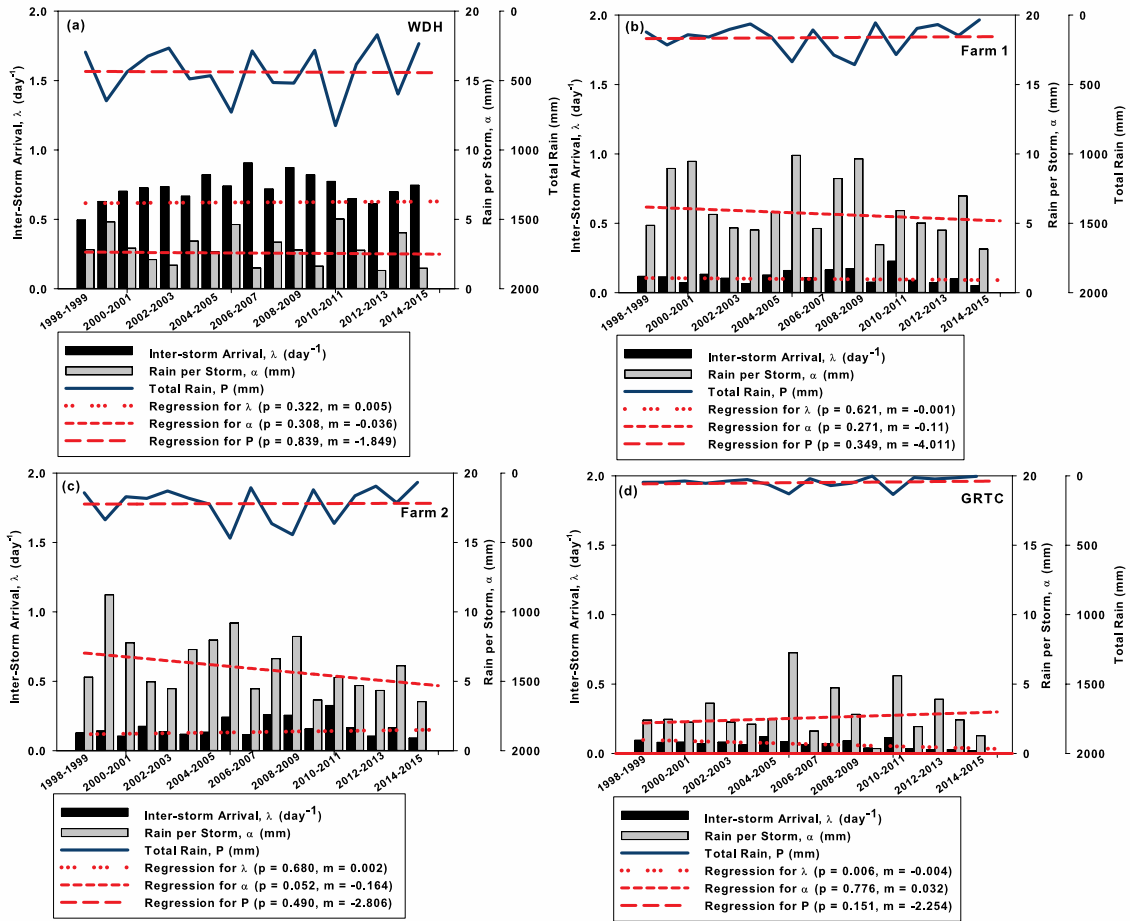


**Figure 4.5** Time series of seasonal precipitation (mm), the average rain depth per storm (mm)  $\alpha$ , and the average storm frequency ( $\text{day}^{-1}$ )  $\lambda$  for (a) Windhoek (WDH), (b) Weltevrede Farm Location 1 (Farm 1), (c) Weltevrede Farm Location 2 (Farm 2), and (d) Gobabeb Research and Training Center (GRTC). Rainy season is from October to April, record length = 17 years, and  $m$  = Sen's slope.



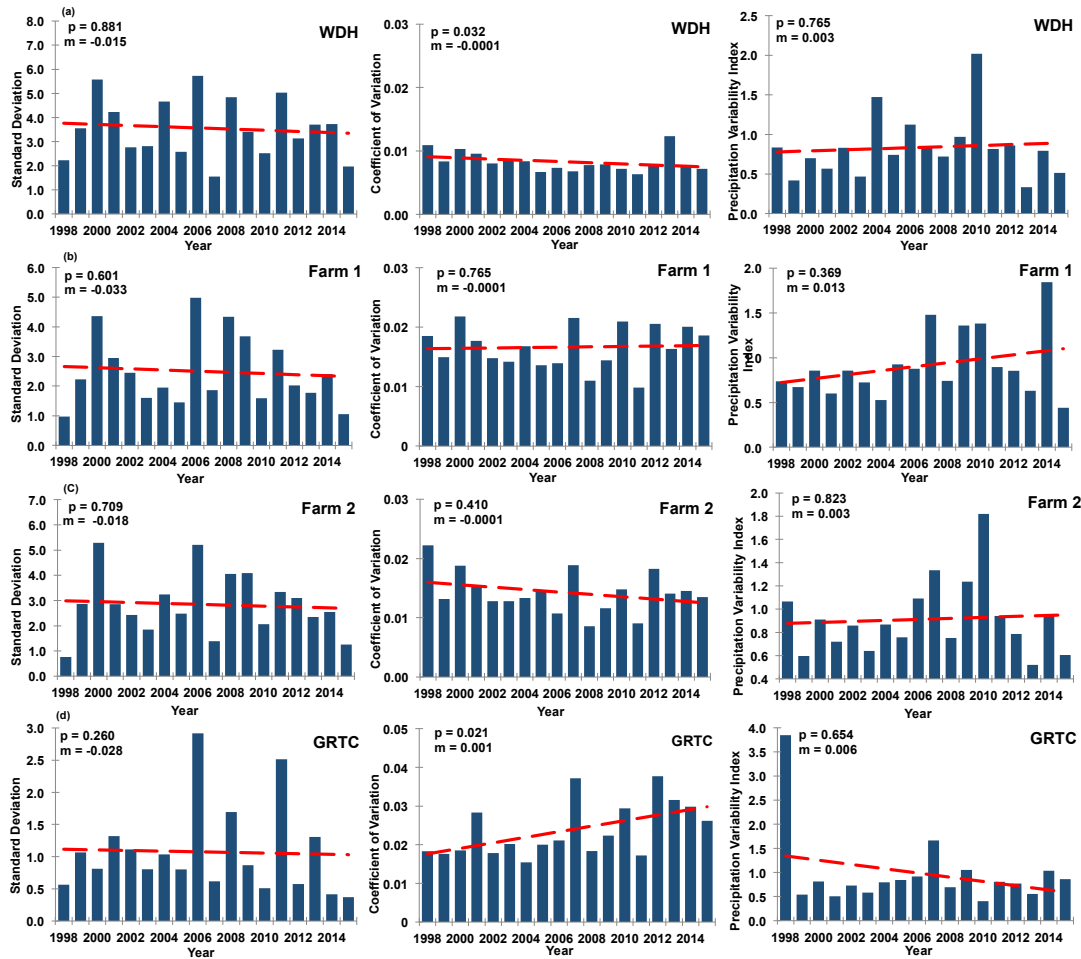


**Figure 4.6** Time series of standard deviation, coefficient of variance (CV), and precipitation variability index (PVI) of annual rainfall (mm) for (a) Windhoek (WDH), (b) Weltevrede Farm Location 1 (Farm 1), (c) Weltevrede Farm Location 2 (Farm 2), and (d) Gobabeb Research and Training Center (GRTC). Record length = 17 years, and  $m$  = Sen's slope.

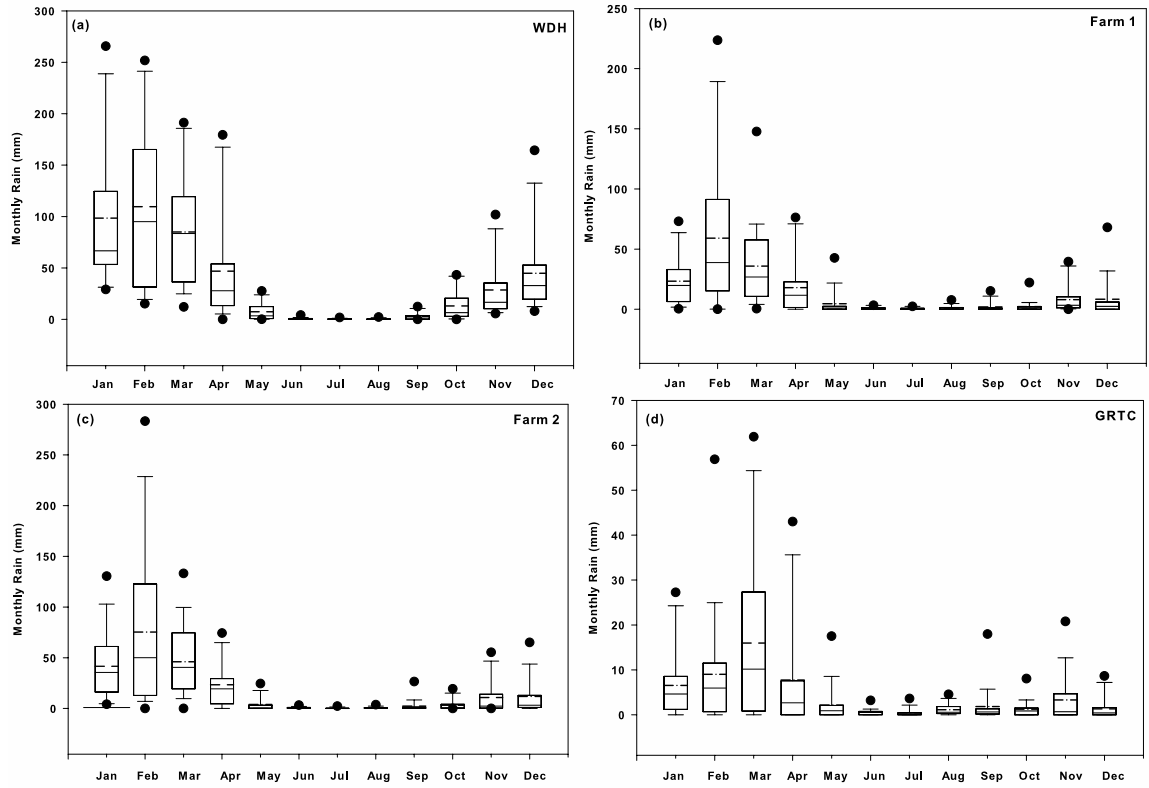


**Figure 4.7** Seasonality of annual precipitation (mm) for (a) Windhoek (WDH), (b) Weltevrede Farm Location 1 (Farm 1), (c) Weltevrede Farm Location 2 (Farm 2), and (d) Gobabeb Research and Training Center (GRTC). Median represented by dark solid line, box represents the 1st and 3<sup>rd</sup> quartile range. The boxes are drawn with widths proportional to the square roots of the number of observations in the groups. The whiskers extend to the most extreme data point which is no more than two times the inter quartile range from the box. Circles represent outliers.

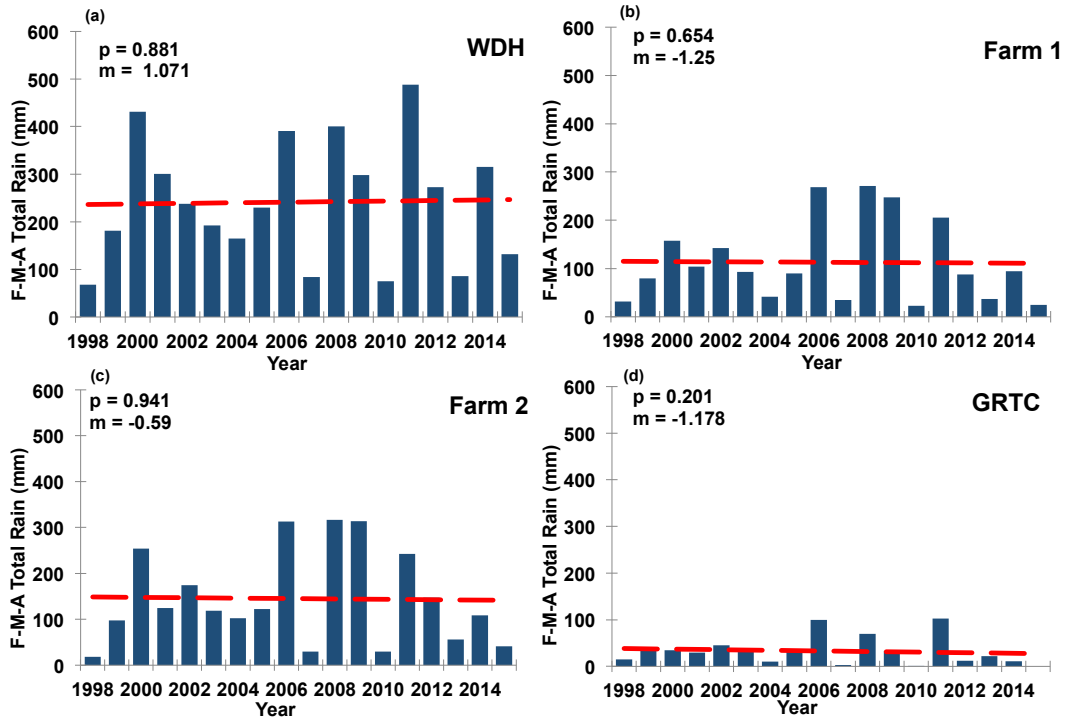


**Figure 4.8** Time series of late summer (February-March-April) precipitation (mm) for (a) Windhoek (WDH), (b) Weltevrede Farm Location 1 (Farm 1), (c) Weltevrede Farm Location 2 (Farm 2), and (d) Gobabeb Research and Training Center (GRTC). Record length = 17 years, and  $m$  = Sen's slope.

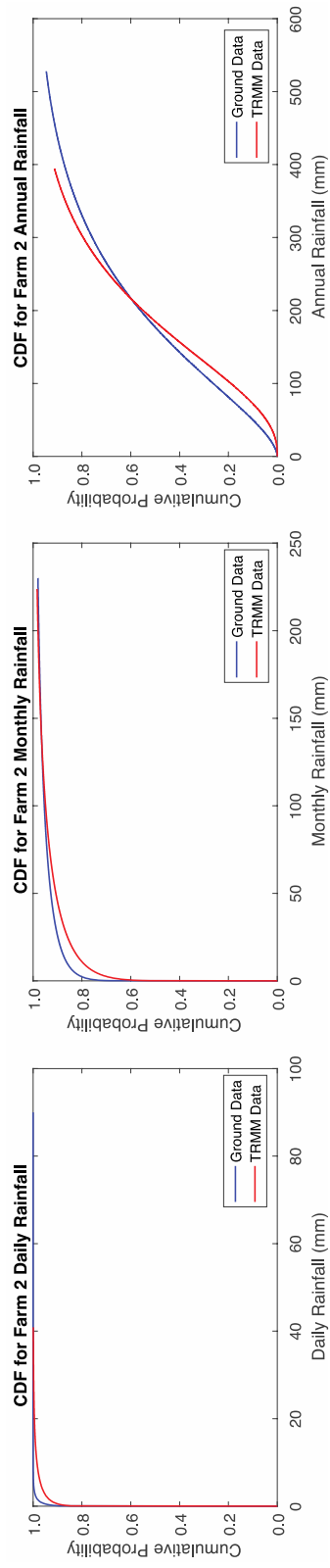


**Figure 4.9** Cumulative Distribution Functions (CDFs) of daily (a), monthly (b), and annual (c) precipitation from gauged estimates at Farm 2 and TMPA data at Farm 1 for period of January 1, 2008 to December 31, 2013.

## References

- AU-IBAR, 2012. Rational Use of Rangelands and Fodder Crop Development in Africa. AU-IBAR Monographic Series No. 1.
- Barros, R.e.a., 2014. Climate Change 2014: Impacts, Adaptation, and Vulnerability. Part B: Regional Aspects. IPCC: 688.
- Bowman, K.P., 2005. Comparison of TRMM precipitation retrievals with rain gauge data from ocean buoys. *Journal of Climate*, 18(1): 178-190.
- Daryanto, S., Wang, L., Jacinthe, P.A., 2016. Global synthesis of drought effects on maize and wheat production. *PLOS One*, 11(5): e0156362.
- Ebert, E.E., Janowiak, J.E., Kidd, C., 2007. Comparison of near-real-time precipitation estimates from satellite observations and numerical models. *Bulletin of the American Meteorological Society*, 88(1): 47-64.
- Eckardt, F., Soderberg, K., Coop, L., Muller, A., Vickery, K., Grandin, R., Jack, C., Kapalanga, T., Henschel, J., 2013. The nature of moisture at Gobabeb, in the central Namib Desert. *Journal of Arid Environment*, 93: 7-19.
- Foissner, W., Agatha, S., Berger, H., Landesmuseum, O., 2002. Soil ciliates (Protozoa, Ciliophora) from Namibia (Southwest Africa), with emphasis on two contrasting environments, the Etosha region and the Namib Desert, 1459. *Biologiezentrum der Oberösterreichischen Landesmuseums*.

- Franz, T.E., Caylor, K.K., Nordbotten, J.M., Rodríguez-Iturbe, I., Celia, M.A., 2010. An ecohydrological approach to predicting regional woody species distribution patterns in dryland ecosystems. *Advances in Water Resources*, 33(2): 215-230.
- Gu, L., Pallardy, S., Hosman, K., Sun, Y., 2014. impacts of precipitation variability on plant species and community water stress in a temperate deciduous forest in the central US. In Press.
- Haeseler, S., 2013. Drought in Namibia 2012/2013. Deutscher Wetterdienst: Wetter und Klima aus einer Hand.
- Hoerling, M., Hurrell, J., Eischeid, J., Phillips, A., 2006. Detection and attribution of twentieth-century northern and southern African rainfall change. *Journal of Climate*, 19(16): 3989-4008.
- Huffman, G.J., Bolvin, D.T., Nelkin, E.J., Wolff, D.B., Adler, R.F., Gu, G., Hong, Y., Bowman, K.P., Stocker, E.F., 2007. The TRMM multisatellite precipitation analysis (TMPA): Quasi-global, multiyear, combined-sensor precipitation estimates at fine scales. *Journal of Hydrometeorology*, 8(1): 38-55.
- Kaseke, K.F., Wang, L., Wanke, H., Turewicz, V., Koeniger, P., 2016. An analysis of precipitation isotope distributions across Namibia using historical data. *PLOS One* 11(5).
- Kneis, D., Chatterjee, C., Singh, R., 2014. Evaluation of TRMM rainfall estimates over a large Indian river basin (Mahanadi). *Hydrology and Earth System Sciences*, 11(1): 1169-1201.

- Millennium Ecosystem Assessment, 2005. Ecosystems and human well-being: desertification synthesis. . World Resources Institute, Washington, DC.
- Ministry of Agriculture, 1999. Rainfall Distribution in Namibia: Data Analysis and Mapping of Spatial, Temporal, and Southern Oscillation Index Aspects.
- New, M., Hewitson, B., Stephenson, D.B., Tsiga, A., Kruger, A., Manhique, A., Lajoie, R., 2006. Evidence of trends in daily climate extremes over southern and west Africa. *Journal of Geophysical Research: Atmosphere*, 111(D14): 1984–2012.
- Namibia Meteorological Service, 2015. <http://www.meteona.com>.
- Oriola, E., 2009. Irrigation agriculture: An option for achieving the millennium development goals in Nigeria. *Journal of Geograph and Regional Planning*, 2(7): 176-181.
- Phillips, J., Cane, M., Rosenzweig, C., 1998. ENSO, seasonal rainfall patterns and simulated maize yield variability in Zimbabwe. *Agriculture and Forest Meteorology*, 90(1): 39-50.
- Rockström, J., Karlberg, L., Wani, S.P., Barron, J., Hatibu, N., Oweis, T., Qiang, Z., 2010. Managing water in rainfed agriculture—The need for a paradigm shift. *Agricultural Water Management*, 97(4): 543-550.
- Simpson, J., Adler, R.F., North, G.R., 1988. A proposed tropical rainfall measuring mission (TRMM) satellite. *Bulletin of the American Meteorology Society*, 69(3): 278-295.

- Su, F., Hong, Y., Lettenmaier, D.P., 2008. Evaluation of TRMM Multisatellite Precipitation Analysis (TMPA) and its utility in hydrologic prediction in the La Plata Basin. *Journal of Hydrometeorology*, 9(4): 622-640.
- Villarini, G., Krajewski, W.F., Smith, J.A., 2009. New paradigm for statistical validation of satellite precipitation estimates: Application to a large sample of the TMPA 0.25° 3- hourly estimates over Oklahoma. *Journal of Geophysical Research: Atmosphere*, 114(D12).
- Wang, L., D'Odorico, P., 2008. The limits of water pumps. *Science*, 321: 36-37.
- Wang, L., D'Odorico, P., Evans, J., Eldridge, D., McCabe, M., Caylor, K., King, E., 2012. Dryland ecohydrology and climate change: critical issues and technical advances. *Hydrology and Earth System Sciences*, 16: 2585-2603.
- Ward, A.D., Trimble, S.W., 2003. *Environmental Hydrology*. CRC Press.



**CHAPTER 5: PARTITIONING OF EVAPOTRANSPIRATION USING A  
STABLE ISOTOPE TECHNIQUE IN AN ARID AND HIGH TEMPERATURE  
AGRICULTURAL PRODUCTION SYSTEM**

**5.1 Abstract**

The agricultural production in the arid and high temperature low-desert systems of Southern California is heavily relied on the irrigation. To better manage these agricultural production systems with increasingly limited water resources, it is very important to understand how much and to what extent the irrigated water is transpired by crops relative to being lost through evaporation. In this study, we examined the evapotranspiration (ET) partitioning over a field of forage sorghum (*Sorghum bicolor*), which was used for biofuel production, based on the isotope measurements of three irrigation cycles at the vegetative stage. We used the customized transparent chambers coupled with a laser-based isotope analyzer to continuously measure the stable isotopic composition of evaporation ( $E$ ,  $\delta_E$ ), transpiration ( $T$ ,  $\delta_T$ ) and ET ( $\delta_{ET}$ ) to partition the total water flux. Due to the extreme heat and dryness,  $\delta_E$  and  $\delta_T$  were very similar, which is rarely seen in the literature and reflect the unique aspects of this system. It was also interesting to find that  $\delta_E$ ,  $\delta_T$ , and  $\delta_{ET}$  increased initially as water was depleted following irrigation, but decreased with further soil drying in the mid to late irrigation cycles. These changes are likely caused by root water being transported from deeper to shallower soil layers. Results indicated that about 46% of the irrigated water delivered to the crop was used as transpiration, with 54% lost as direct evaporation during the crop development

for this biofuel production system. This implies that about 28 - 39% of the total source water was used by crops, considering the typical 60 - 85% efficiency of flood irrigation system. Therefore there is a need to improve the water management in these systems to minimize unproductive water losses.

## 5.2 Introduction

Agriculture is the largest single user of fresh water globally, accounting for approximately 70% of the total withdrawn for human consumption (Hoekstra and Mekonnen, 2012; Wada et al., 2014). In the United States (US), irrigated agriculture is the second largest primary user of fresh water, accounting for 31% of the developed water resource (Vörösmarty et al., 2000). The Imperial Valley, in the low elevation desert of southern California, a region characterized by extreme heat and evaporation, has been considered as a promising area for biofuel feedstock production (Oikawa et al., 2015). This area produces more than two-thirds of winter vegetables consumed in the US and about three-quarters of summer hay and other field crops in southern California (Medellín-Azuara et al., 2012). At present, there is a lack of data addressing the sustainability, including water use efficiency, of biofuel production in this high temperature agricultural site.

The Colorado River is a key source of water for California's irrigated desert agriculture, accounting for approximately one-third of annual flow (Cohen et al., 2013). A growing demand for water, coupled with the limited supplies and impacts of climate change (Vörösmarty et al., 2000), has placed enormous pressures on California's water supply. Recent years of drought have exacerbated this water scarcity challenge, especially in the Imperial Valley.

Evapotranspiration (ET) represents one of the largest components of the global water cycle, with approximately 65% of precipitation returned to the atmosphere via ET

at the global scale (Trenberth et al., 2007). However, ET loss can reach up to 95% in some dryland systems (Wang et al., 2014; Wilcox and Thurow, 2006). Evapotranspiration consists of two distinct components: evaporation from soil and plant surfaces (E) and transpiration taken up by roots and lost through stomatal pores (T). These two components are controlled by different processes and have different water use implications. Transpiration is mainly controlled by atmospheric evaporative demand and soil water status, and modified by plant physiological controls on leaf stomata. Because photosynthetic carbon dioxide fixation is concurrent with water vapor loss, and shares the stomatal diffusion pathway, irrigated water transpired by crops is productive in that it facilitates photosynthesis and leads to leaf cooling. Evaporation from soil, in contrast, is not directly linked to biological processes, but rather results from diffusion of water through the soil matrix and evaporation at the surface, and is controlled solely by physical factors. Although it may lead to local evaporative cooling, this water loss is not directly linked to biological productivity. Because of the different controlling mechanisms, E and T are likely to have different responses to environmental drivers such as temperature and soil water content (Kool et al., 2014; Wang et al., 2014). As competition for available irrigation water increases, a better understanding of how much is transpired relative to that lost through evaporation, and the factors controlling this partitioning, could contribute to improved water resource management (Wang and D'Odorico, 2008).

Separating E and T has proven to be difficult. Various methods have been proposed, including empirical measurements and modeling-based approaches. Empirical measurements can include lysimeters, large tree potometers, whole tree chambers, eddy covariance measurements of above- and below-canopy fluxes, up-scaling of sap-flow measurements, and flux-variance similarity partitioning, as well as using stable isotopes (Kool et al., 2014). Modeling approaches include the FAO-56 dual crop coefficient model (Ding et al., 2013), modeling of canopy and subcanopy fluxes driven by energy balance measurements (Ershadi et al., 2014; Kalma et al., 2008) or combining process-based modeling and isotope tracer measurements (Cai et al., 2015; Wang et al., 2015). The recent development of techniques using stable isotopes of water has provided a useful tool to separate E and T, that can be applied across broad spatial and temporal scales. Besides facilitating ET partitioning, the stable isotopic composition of E and T can also provide insights regarding plant water use dynamics as well as the nature of land-atmosphere interactions (Parkes et al., 2016).

The basis for using the isotopes of H and O in water to partition ET is that evaporation significantly fractionates the surface soil water, enriching the source with the heavier isotopes, while transpiration does not lead to fractionation when T is large (Wang et al., 2012; Wang et al., 2013). Therefore, the isotopic composition of transpiration ( $\delta_T$ ) remains similar to the isotopic composition of the plant source water, while the isotopic composition of evaporated water differs from that of the source. This results in distinct isotopic signatures of  $\delta_E$  and  $\delta_T$  (Wang et al., 2013; Zhang et al., 2011).

The development of field-deployable laser-based instruments with similar precision to traditional isotope ratio mass spectrometers (e.g., (Wang et al., 2009)), has provided a promising tool to separate T from E in agricultural systems (Wang et al., 2012; Wang et al., 2013). The application of such methods to direct measurement of the isotopic composition of E, T and the combination, ET, in a hot, arid agricultural production system has not previously been attempted.

The objectives of the current study are to: (1) use a laser-based isotope analyzer and customized T, E and ET chambers to measure the respective isotope signatures,  $\delta_T$ ,  $\delta_E$ , and  $\delta_{ET}$ ; (2) combine the estimates of  $\delta_T$ ,  $\delta_E$ ,  $\delta_{ET}$  and total ET to partition the evaporative flux and to quantify the fraction of irrigation that is partitioned to productive T in this sorghum production system. These measurements provide important information for regional water issues, for crop management scenarios, and offer substantial insight into currently temperate production systems that may become warmer.

### **5.3 Materials and methods**

#### **5.3.1 Study site**

The study was conducted at the University of California's Desert Research and Extension Center (DREC) located in the Imperial Valley, southern California (32.867°N 115.448°W) (Figure 5.1a). This area is an interior desert valley about 18.3 m below sea level. The weather represents a desert climate with over 350 days of sunshine. The nearest automatic weather station (Meloland, 32.806°N 115.446° W) is managed by the California Management Information System (CIMIS) (<http://www.cimis.water.ca.gov>).

Routine meteorological variables, including solar radiation, wind, humidity, air temperature, precipitation and soil temperature, as well as reference ET ( $ET_0$ ), have been recorded hourly since December 1989. The mean annual precipitation from 1990 to 2015 was  $80.3 \text{ mm year}^{-1}$ , while the mean annual  $ET_0$  reached  $1846 \text{ mm year}^{-1}$  (Figure 5.1b). Most of the rainfall occurs in late summer, with June being the driest month (Figure 5.1b). The mean annual temperature is  $22.4^\circ\text{C}$  with a monthly mean temperature of  $12.6^\circ\text{C}$  in January and  $32.9^\circ\text{C}$  in August (for the period 1990–2015) (Figure 5.1c). The mean annual relative humidity of the study area is around 46% (Figure 5.1d). The experimental field has been used for agricultural production since the establishment of DREC in 1912. Irrigation water is supplied through the All-American Canal, distributed by gravity from the Colorado River. Irrigation is provided by regularly scheduled flooding of furrows. Soils in the regions are moderately to well-drained deep alluvial soils (42% clay, 41% silt 16% sand) with sub-surface drainage tile, and pH of 8.3 (Oikawa et al., 2014).

The Sorghum bicolor (cv. Photoperiod LS; Scott Seed Inc.) was planted in February 2012 for biofuel production, and was cut three times each year at the end of the vegetative stage. Ten extensive field measurements of  $\delta_T$ ,  $\delta_E$  and  $\delta_{ET}$  were conducted on July 24, 26, 28, 30 and August 4, 6, 7, 13, 18 and 20, 2014. Measurements covered the three irrigation cycles of one of the three vegetative harvests obtained each year. Plants were harvested for biomass before substantial flowering had occurred, and thus remained in the vegetative stage throughout the experiment. The irrigation events occurred on July 22, July 31 and August 9, 2014, each lasting 24 h. Isotope sampling was conducted one

full day after irrigation to allow for drainage. There were two minor rainfall events during the measurement period, with a total rainfall of 1.27 mm. The mean monthly air temperature was 33.5 °C and 31.9 °C in July and August 2014.

### 5.3.2 Isotope-based partitioning

The technique developed by Wang et al. (2012; 2013) was modified to fit our specific needs. The isotopic compositions of the three component vapor fluxes ( $\delta_T$ ,  $\delta_E$  and  $\delta_{ET}$ ) were directly quantified using a field deployable Triple Water Vapor Isotope Analyzer (T-WVIA, Los Gatos Research, Inc., Mountain View, CA, USA). Samples were obtained using customized transparent acrylic chambers containing circulation fans and directly linked as a closed system with the T-WVIA.  $\delta_T$  was measured at 1 Hz with a customized leaf chamber (2 × 4 × 12 cm) having leaves sealed inside the chamber for 1-2 min. The  $\delta_E$  and  $\delta_{ET}$  were measured using a larger customized chamber (50 × 50 × 50 cm) placed over bare soil or over areas with both soil and vegetation. Chamber measurements were obtained under sunny conditions between 11:00 and 14:00 when stomata were as open as soil moisture allowed. This method has been shown to capture the short-term variations in  $\delta_T$ ,  $\delta_E$  and  $\delta_{ET}$ , including fast  $\delta_T$  responses to radiation (Wang et al., 2012).

The fraction of ET partitioned to T is found through measurement of isotopic signatures  $\delta_E$ ,  $\delta_T$  and  $\delta_{ET}$ . Assuming a two-component mixing model, the transpired fraction of ET is given by:

$$\frac{T}{ET} = \frac{\delta_{ET} - \delta_E}{\delta_T - \delta_E}, \quad (1)$$



where  $\delta_E$ ,  $\delta_{ET}$ , and  $\delta_T$  are the isotope signatures of E, ET and T, respectively (Wang et al., 2010).

Keeling plot and mass balance approaches have been used to estimate the isotopic composition of vapor fluxes. The Keeling plot approach assumes constant concentration and isotopic compositions of the ambient water vapor ( $\delta_A$ ). Source water vapor isotopic composition (e.g.,  $\delta_E$ ,  $\delta_T$  or  $\delta_{ET}$ ) was calculated as:

$$\delta_M = C_A(\delta_A - \delta_S) \left( \frac{1}{C_M} \right) + \delta_S, \quad (2)$$

where  $\delta_M$ ,  $\delta_A$  and  $\delta_S$  are the isotopic compositions of mixed water vapor, ambient water vapor and source water vapor in ET, E or T.  $C_M$  is the mixed water vapor concentration and  $C_A$  is the ambient water vapor concentration at the measurement location (Wang et al., 2010).

The calculation of source water vapor isotopic composition using a mass balance approach was given as:

$$\delta_S = \frac{C_M \delta_M - C_A \delta_A}{C_M - C_A}, \quad (3)$$

Under our measurement conditions, the maximum concentration of water vapor before condensation occurred in August was 49,100 ppm. Measurements were terminated when water concentration approached 45,000 ppm in order to prevent condensation. The  $\delta_E$ ,  $\delta_T$  and  $\delta_{ET}$  were measured at random locations with four repeated measurements from each sampling time. Data were excluded due to instrumental malfunction and obvious data errors (e.g., the fraction of ET is greater than 1 or less than 0). ET partitioning was not possible for August 13, August 18, and August 20, as chamber-based  $\delta_{ET}$  was not

available. Both  $\delta^{18}\text{O}$  and  $\delta\text{D}$  data were used to demonstrate the temporal changes in  $\delta_{\text{E}}, \delta_{\text{T}}$  or  $\delta_{\text{ET}}$ , while only  $\delta\text{D}$  data were used for ET partitioning. A summary of isotopic signatures for transpiration (T), evaporation (E), and evapotranspiration (ET) over our measurement was provided in Appendix E.

### 5.3.3 Total ET measurements

Total ET was monitored at 10 Hz using the eddy-covariance technique via an open-path infrared gas analyzer (IRGA) (Li7500, LI-COR, Lincoln, NE, USA) and a 3-D sonic anemometer (CSAT3, CSI, Logan, Utah, USA) (Oikawa et al., 2015). The instrument was mounted on a tower located within 10 m of the chamber measurements, at a height of 2.5 m above the canopy. Data processing was conducted in EddyPro 5.2 (LI-COR, Lincoln, NE, USA) and followed standard flux calculations over 30 min intervals. The footprint of the tower was determined using an approximate analytical model (Hsieh et al., 2000). Evapotranspiration fluxes with 70% of the footprint exceeding the edge of the field were removed. The ET data were gap-filled following Reichstein et al. (2005).

## 5.4 Results

This study was conducted under extremely hot and arid conditions (Figure 5.1). Figure 5.2 shows the hydrogen and oxygen isotopes in the evaporation and transpiration waters. The  $\delta^{18}\text{O}$  of transpiration water ( $\delta_{\text{T}}$ ) ranged from -6.07 to 6.99‰, with a mean value of 0.04‰ and standard deviation of 3.60‰, while  $\delta\text{D}$  of  $\delta_{\text{T}}$  ranged from -89.75 to -70.44‰, with a mean value of -83.27‰ and standard deviation of 7.28‰ (Figure 5.2).

The least squares fitting between  $\delta D$  and  $\delta^{18}O$  in transpiration was:  $\delta D = 1.4 \times \delta^{18}O - 83.3$  ( $R^2 = 0.47$ ,  $p < 0.05$ ). The  $\delta^{18}O$  of evaporation water ( $\delta_E$ ) ranged from -4.99 to 5.10‰, with a mean value of -1.35‰ and standard deviation of 3.52‰, while  $\delta D$  of  $\delta_E$  ranged from -97.33 to -71.07‰, with a mean value of -83.48‰ and standard deviation of 8.39‰ (Figure 5.2). The least squares fitting between  $\delta D$  and  $\delta^{18}O$  in evaporation was:  $\delta D = 1.5 \times \delta^{18}O - 82.0$  ( $R^2 = 0.38$ ,  $p < 0.05$ ). The local meteoric water line (LMWL) determined via least squares fitting of the irrigation water isotopic values was:  $\delta D = 7.3 \times \delta^{18}O + 3.6$ .

All  $\delta_E$  values fell to the right side of the irrigation waters line of best fit, revealing a strong evaporation effect on of  $\delta_E$  (Figure 5.2). The  $\delta D$ - $\delta^{18}O$  regression lines for both  $\delta_T$  and  $\delta_E$  deviated substantially from their corresponding local meteoric water line (LMWL), producing very negative values of deuterium excess (i.e., d-excess: defined as d-excess =  $\delta D - 8.0 \times \delta^{18}O$ ) of  $\delta_T = -83.6$  and  $\delta_E = -70.0$ ‰. Although such negative d-excess values are not commonly seen, the values are comparable to those obtained in a recent study in one of the driest regions in China. In that study, a negative d-excess value of -85.6‰ in leaf water was reported (Zhao et al., 2014). In the present study, the slopes of the  $\delta D$ - $\delta^{18}O$  regression lines for  $\delta_T$  and  $\delta_E$  were much lower than 8.0, suggesting substantial water loss through direct evaporation and transpiration drawn from isotopically enriched soil water. Moreover, the intersections of  $\delta D$ - $\delta^{18}O$  regression lines for  $\delta_T$  and for  $\delta_E$  and irrigation water line fell within the range of the isotopic compositions of irrigation waters, supporting an E and T origin from this source (Figure 5.2).

In contrast to the expectation that the isotopic signatures of T, E, and ET would become increasingly enriched as soils became drier, our results present a more complex pattern. Here, the isotopic signatures of E, T and ET increased (less negative) initially as water was depleted, but then decreased at the end of each irrigation cycle (Figure 5.3a and b). Both  $\delta D$  and  $\delta^{18}O$  followed similar patterns and it was replicated in all three irrigation cycles (Figure 5.3a and b).

ET partitioning was calculated using a simple 2-source model, as defined in Eq. (1). It was estimated that about  $46\% \pm 5.6\%$  of the irrigated water was used as transpiration by crops after runoff as tailwater and drainage, while 54% was lost as direct evaporation from the soil (Table 5.1). Transpiration between May and October 2014 ranged from 0.59 to 6.08 mm/day, with a mean value of 3.04 mm/day (Figure 5.4). Both T/ET and LAI increased as the crop developed (Figure 5.5a) during the vegetation stage and the relationship between T/ET and LAI was  $T/ET=0.45 \times LAI^{0.19}$  (Figure 5.5b).

## **5.5 Discussion**

An increasing number of studies have used the stable isotope technique to separate ET components, and predict ET partitioning changes under both agricultural and natural settings. Here we present one of the first studies testing the field application of a chamber method to directly measure isotopic composition of all three components (E, T and ET), in an extreme agricultural production environment. By using this approach, we could also predict the patterns of plant water use based on the changes in the isotopic composition of transpired water. Particularly we monitored the plant water use pattern at

the vegetative stage. Water loss by evaporation can be much higher at the vegetative stage than during the later growing stages (Wang et al., 2014), so improvement in water management can be most beneficial at this stage.

Of particular interest was the examination of these evaporative processes under extremely hot and arid condition of southern California, with local conditions having a mean  $ET_0$  of more than 20 times the mean annual precipitation. Due to the extreme heat and aridity,  $\delta_E$  and  $\delta_T$  were very similar, which is rarely seen in the literature, underscoring the unique environmental conditions at the study site (see Figure 5.6). The small difference between  $\delta_T$  and  $\delta_E$  makes it challenging to accurately discriminate the isotopic compositions of these two fluxes, and ultimately to partition total ET into relative rates of E and T. Despite this complexity, our chamber method generally worked well for  $\delta_T$ ,  $\delta_E$ , and  $\delta_{ET}$  estimates, based on agreement between the Keeling plot and mass balance approaches.

Our results yield interesting insights into how isotopic signatures of T, E and ET can change with depletion of water within the irrigation cycles. Contrary to the expectation that the isotopic signatures of T, E, and ET would continuously become enriched as soils became drier, we have observed that the isotopic signatures of E, T and ET increased as water was depleted, but decreased at the end of each irrigation cycle. The observed pattern of depleted isotopic signatures of T, E, and ET in mid to late irrigation cycles might be caused by lateral roots accessing water from deeper soil depths when shallow water is reduced, redistributing the deeper water to shallower layers (Ahmed et

al., 2016; Stone et al., 2001). The root system of maize, a related  $C_4$  grass, consists of pre-embryonic primary and seminal roots formed during embryogenesis and lateral roots formed during post-embryonic development (Ahmed et al., 2016). A recent study using neutron radiography to examine the mechanism of maize root water uptake has found that the function of lateral roots is to uptake water from the soil while the function of primary and seminal roots is to axially transport water to the shoot (Ahmed et al., 2016). As sorghum has similar root water uptake dynamics to corn (Srayeddin and Doussan, 2009), this rooting mechanism might explain why the isotopic signatures of E, T, and ET increase but then decrease within an irrigation cycle. As sorghum roots grow steadily throughout the season, when the shallow water is depleted and soil dries out, the lateral roots could extract water from the subsoil and redistribute it to the surface layer for transpiration and evaporation, leading to isotopic depletion of E, T and ET.

Other factors such as soil properties and precipitation could also influence the amount and the isotopic composition of different components of ET. The small precipitation events occurring on August 2 and August 3, 2014 likely caused a higher value of  $\delta_E$  on August 4 and 6 (Figure 5.5) due to a strong evaporation of the rainwater on soil surface. The  $\delta_T$  is lower than  $\delta_E$  for these two cases because transpiration response is likely damped due to the crop water use from deeper soil layers, in addition to the use of limited surface rain- fall water. The daily average soil moisture varies between 0.17 and  $0.42 \text{ cm}^3 \text{ cm}^{-3}$  (Oikawa et al., 2014), and all samplings were conducted after irrigation when the field is still at field capacity. Transpiration values measured at our site were

comparable to those measured in other dryland agriculture sites. However, the ratio of transpiration to evapotranspiration ( $T/ET$ ) was considerably lower. For example, a study in China found that measured  $T$  ranged from 1.02 to 4.91mm/day, accounting for 60% to 83% of the total  $ET$  (Zhang et al., 2011). Based on this study, the ratio of transpiration to evapotranspiration ( $T/ET$ ) slightly increased with the increasing trend of leaf area index ( $LAI$ ) as crops develop (Figure 5.5). The relationship between  $T/ET$  and  $LAI$  from our study is well within the range reported in a previous study of early season water loss and  $LAI$  (Wang et al., 2014). We have estimated that the rate of evaporation could be as high as 54% at the vegetative stage, thus it may be possible to improve water use efficiency of sorghum at the early growing stage in such systems with extremely limited water resources. The vegetative stage may play a dominant role in seasonal  $T/ET$  (Kang et al., 2003; Wang et al., 2014), particularly in forage and lignocellulosic biofuel systems which remain in the vegetative stage. Our measurements from one vegetative harvest cycle may be representative of the water use dynamics of the entire growing season.

Like many crops in the Imperial Valley, the forage sorghum evaluated here was irrigated through flooding of furrows. Compared to the other irrigation systems such as drip and spray irrigation, flood irrigation exhibits some inefficiency due to surface runoff, deep percolation and unproductive evaporative losses (Cooley et al., 2009). However, flood systems have advantages such as simplicity of design, low capital investment, and low energy requirement. Deep drainage to the tile system is critical in this environment to leach salts that have accumulated from the irrigation water (Oikawa et al., 2015). The

Colorado River, at the point of interception of the All American Canal, has a salinity of 879 mg L<sup>-1</sup> TDS (Forum, 2011). It has been estimated that the potential irrigation efficiency (defined as the volume of water used by the plant divided by the volume of irrigation water applied to the field minus changes in surface and soil storage) for flood irrigation systems ranges from 60 to 85% (Cooley et al., 2009). Combining the current analysis and the typical efficiency of flood irrigation system, the amount of water used by the plant via transpiration relative to the amount of water delivered to the field in this case ranged from 28 to 39%. This indicates that although the production of biofuel feedstock is extremely high under the climate and soil conditions of this region (Oikawa et al., 2015), the water use and water use efficiency may need to be taken into consideration for the sake of sustainability.

## **5.6 Conclusions**

This study presents a novel application of the combined use of customized chambers and a laser-based isotope analyzer to directly quantify isotopic signatures of T, E and ET in situ and examine ET partitioning over a field of forage sorghum in an extreme field condition. As a consequence of strong evaporation under extreme heat and arid conditions, the studied system showed similar  $\delta_T$  and  $\delta_E$  values, which is rarely seen in the literature and increases the difficulty in discriminating isotopic signatures and to partition ET. The strong evaporative gradient in this ecosystem was supported by the fact of very low slopes of  $\delta D$  and  $\delta^{18}O$  relationship for both  $\delta_T$  and  $\delta_E$ .



The results revealed an interesting pattern of the isotopic signatures of E, T, and ET. All components increased as the soil dried, but decreased at the mid to end of each irrigation cycle. These changes were likely a result of the lateral roots extracting water from the subsoil and redistribution to the surface layer, so both crop and surface soil evaporation would access water from deeper layers when the shallow water is depleted. For the studied ecosystem, approximately 46% of the irrigated water delivered to the crops was transpired, with 54% lost via direct evaporation from the soil during the vegetative stage. Considering inherent irrigation inefficiencies, approximately 28 – 39% of the total source water was used by crops, suggesting potential for improved water use efficiency.

**Table 5.1** Evapotranspiration partitioning calculations at representative sampling dates.

<b>Date</b>	<b>%T</b>	<b>%E</b>
<b>7/24/2014</b>	40.2	59.8
<b>7/28/2014</b>	39.3	60.7
<b>7/30/2014</b>	51.8	48.2
<b>8/4/2014</b>	47.3	52.7
<b>8/6/2014</b>	52.3	47.7
<b>8/7/2014</b>	45.0	55.0
<b>Mean</b>	46.0	54.0
<b>SD</b>	5.6	5.6

Note: SD refers to standard deviation.

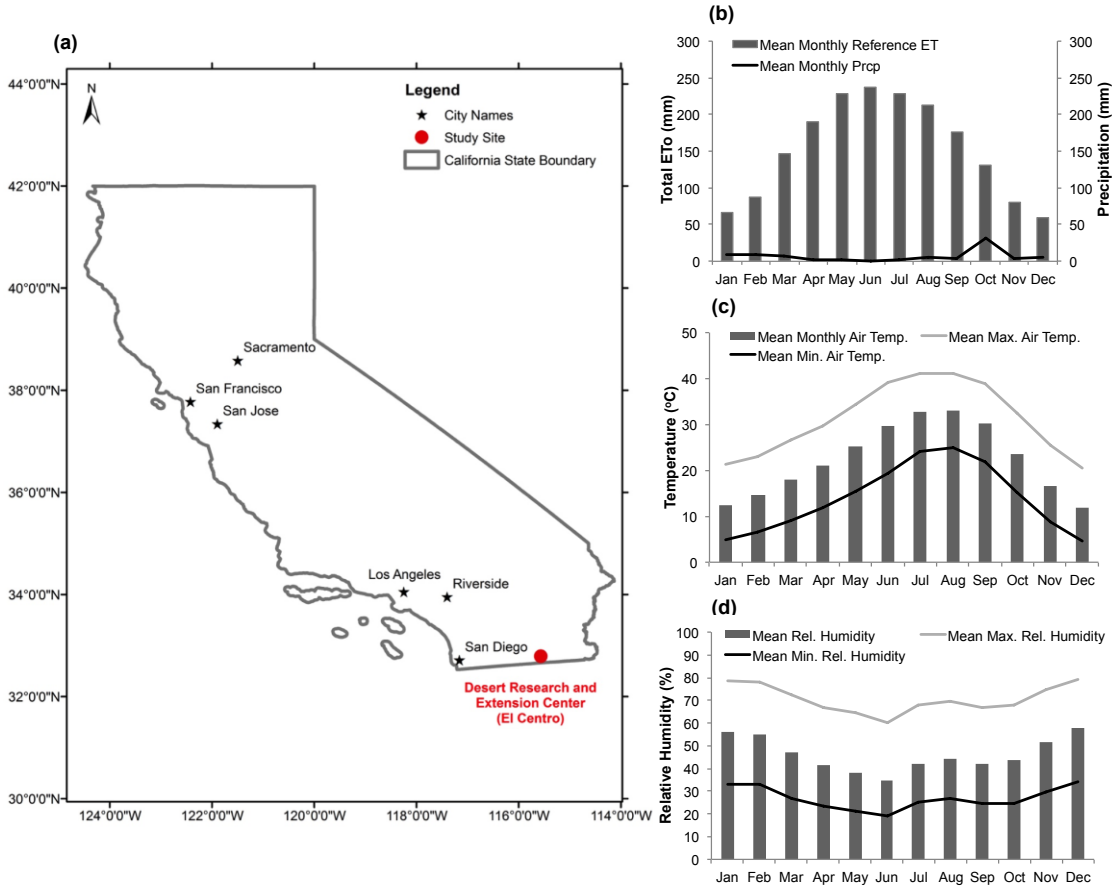


**Figure 5.1** Location of the University of California Desert Research and Extension Center (DREC). Monthly mean precipitation (mm), reference evapotranspiration (ET<sub>0</sub>) (mm), temperature and relative humidity over 1990 – 2015 for the Meloland station of the California Irrigation Management Information System (CIMIS), located within a few hundred meters of the experimental field.

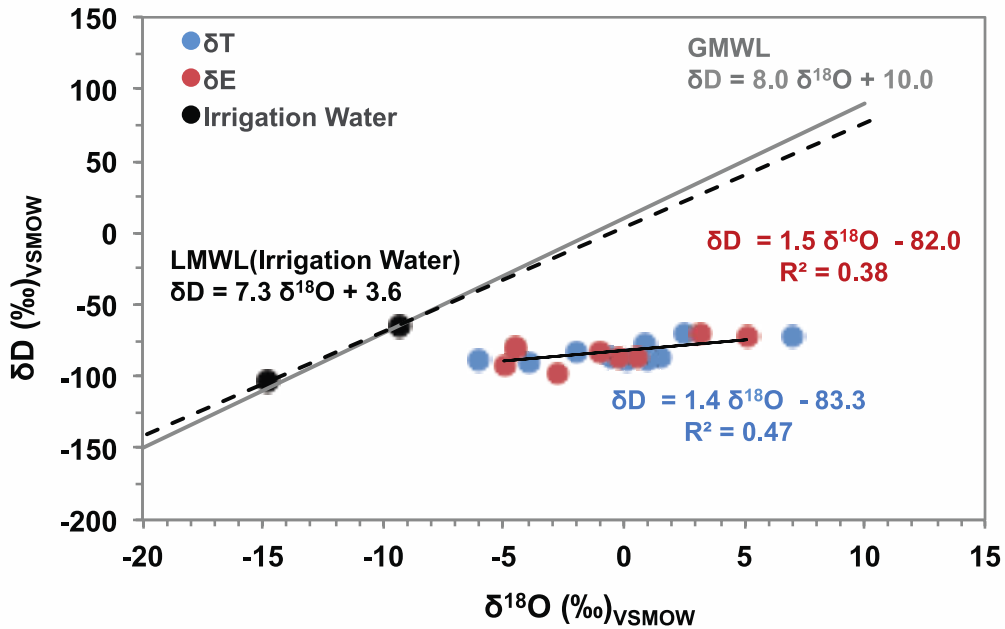


**Figure 5.2** The  $\delta D$ - $\delta^{18}O$  relationships of leaf transpiration ( $\delta_T$ , blue circles) and soil evaporation ( $\delta_E$ , red circles). Black circles depict the measured isotopic composition of the irrigation water. The dashed black line is the Local Meteoric Water Line, determined via least-squares fitting of the irrigated water isotope values. The solid gray line is the Global Meteoric Water Line (GMWL). VSMOW is Vienna Standard Mean Ocean Water.

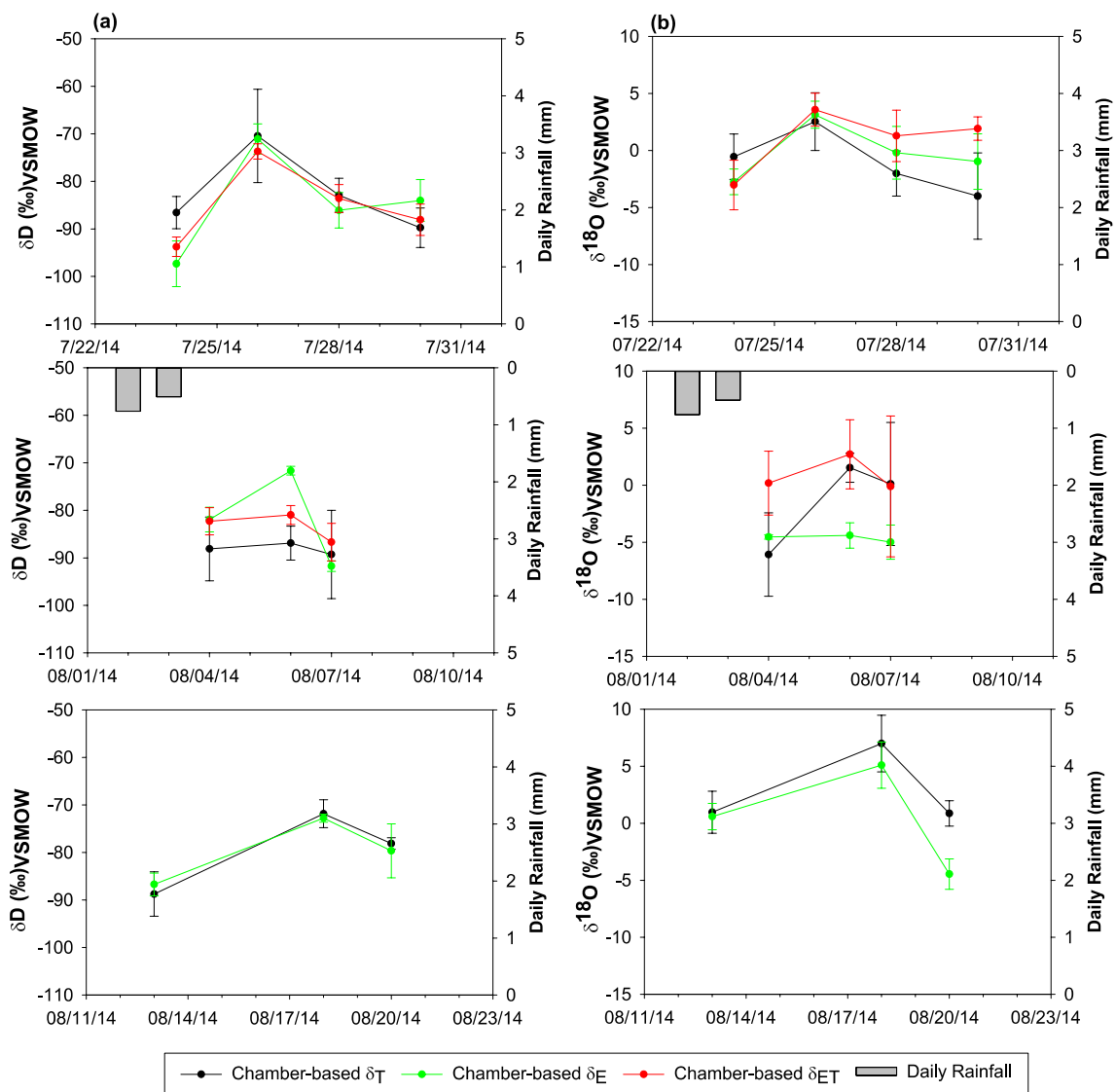


**Figure 5.3** Patterns of deuterium and oxygen isotope signatures for transpiration (T), evaporation (E) and evapotranspiration (ET) over the irrigation cycles. (a) observed pattern for deuterium ( $\delta D$ ), (b) observed pattern for oxygen ( $\delta^{18}O$ ). VSMOW stands for a standard of Vienna Standard Mean Ocean Water.

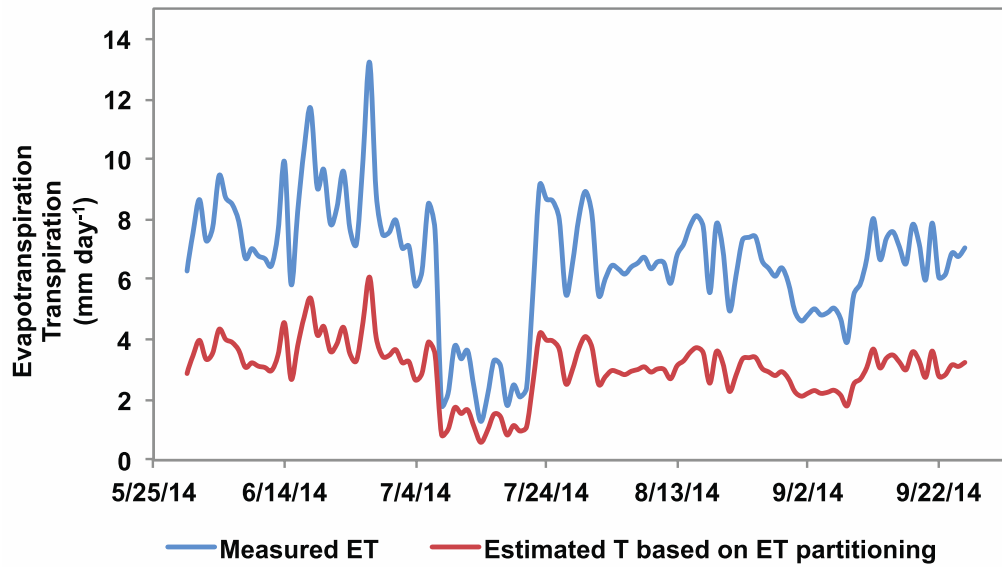


**Figure 5.4** Daily variation of transpiration (T) and evapotranspiration (ET) during the vegetative stage, calculated by combining isotope partitioning and total ET results obtained from concurrent eddy covariance measurements.

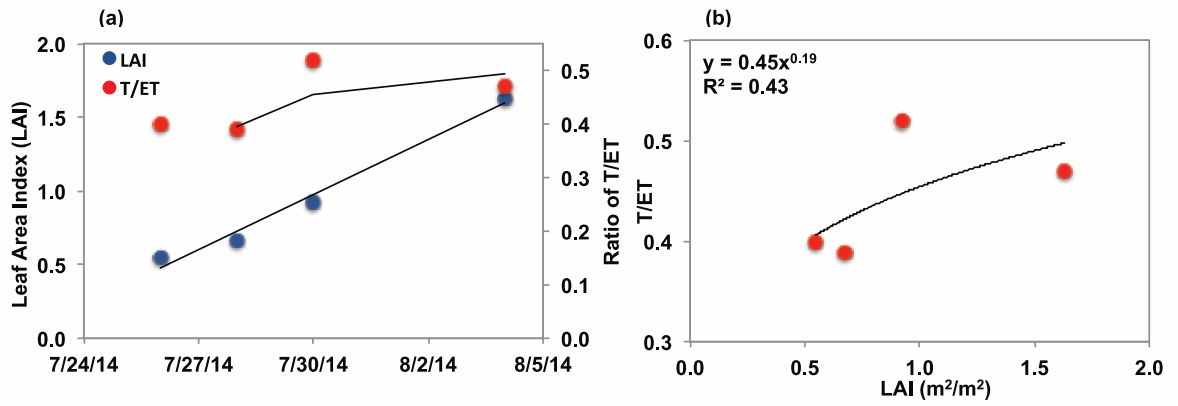


**Figure 5.5** Variations of leaf area index (LAI) during crop development (a) and the relationship between T/ET and LAI (b).

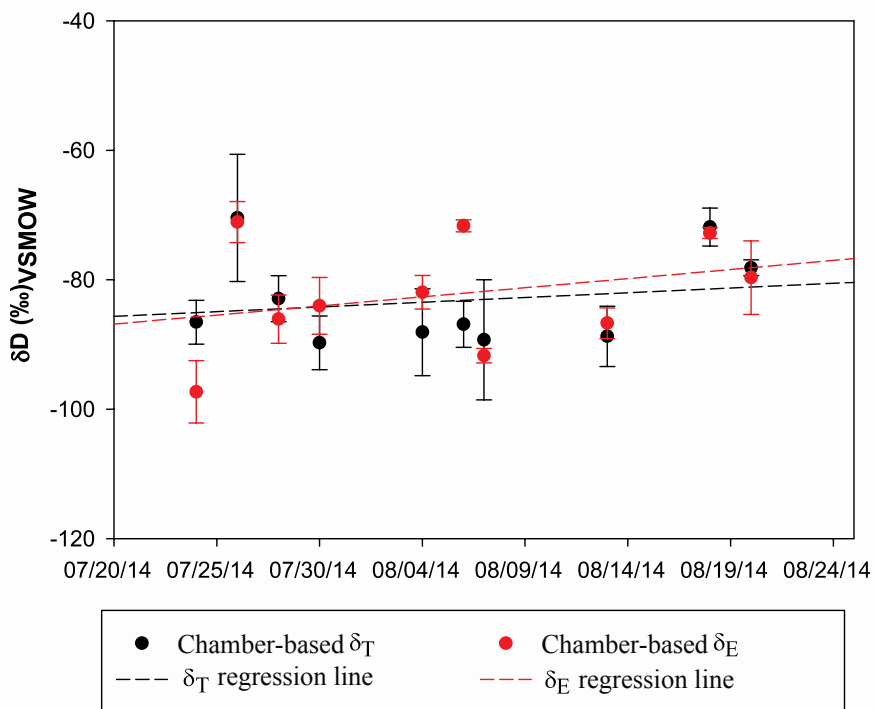


**Figure 5.6** Comparison of deuterium isotope signature of leaf transpiration ( $\delta_T$ ) and soil evaporation ( $\delta_E$ ) over the measurement period. VSMOW stands for a standard of Vienna Standard Mean Ocean Water.



## References

- Ahmed, M.A., Zarebanadkouki, M., Kroener, E., Kaestner, A., Carminati, A., 2016. Measurements of water uptake of maize roots: the key function of lateral roots. *Plant Soil*, 398: 59-77.
- Cai, M.Y., Wang, L., Parkes, S.D., Strauss, J., McCabe, M.F., Evans, J.P., Griffiths, A.D., 2015. Stable water isotope and surface heat flux simulation using ISOLSM: evaluation against in-situ measurements. *Journal of Hydrology*, 523: 67-78.
- Cohen, M., Christian-Smith, J., Berggren, J., 2013. *Water to Supply the Land*.
- Cooley, H., Christian-Smith, J., Gleick, P.H., 2009. *Sustaining California agriculture in an uncertain future*.
- Ding, R., Kang, S., Zhang, Y., Hao, X., Tong, L., Du, T., 2013. Partitioning evapotranspiration into soil evaporation and transpiration using a modified dual crop coefficient model in irrigated maize field with ground-mulching. *Agricultural water management*, 127: 85-96.
- Ershadi, A., McCabe, M.F., Evans, J.P., Chaney, N.W., Wood, E.F., 2014. Multi-site evaluation of terrestrial evaporation models using FLUXNET data. *Agriculture and Forest Meteorology*, 187: 46-61.
- Forum, C.R.B.S.C., 2011. *Water Quality Standards for Salinity Colorado River System*
- Hoekstra, A.Y., Mekonnen, M.M., 2012. The water footprint of humanity. *Proceedings of the National Academy of Sciences*, 109(9): 3232-3237.

- Hsieh, C.I., Katul, G., Chi, T.W., 2000. An approximate analytical model for footprint estimation of scalar fluxes in thermally stratified atmospheric flows. *Advances in Water Resources*, 23(7): 765-772.
- Kalma, J., McVicar, T., McCabe, M., 2008. Estimating land surface evaporation: A review of methods using remotely sensed surface temperature data. *Surveys in Geophysics* 29: 421-469.
- Kang, S., Gu, B., Du, T., Zhang, J., 2003. Crop coefficient and ratio of transpiration to evapotranspiration of winter wheat and maize in a semi-humid region. *Agricultural Water Management*, 59(3): 239-254.
- Kool, D., Agam, N., Lazarovitch, N., Heitman, J.L., Sauer, T.J., Ben-Gal, A., 2014. A review of approaches for evapotranspiration partitioning. *Agriculture and Forest Meteorology*, 184: 56-70.
- Medellín-Azuara, J., Vergati, J.A., Sumner, D.A., Howitt, R.E., Lund, J.R., 2012. Analysis of effects of reduced supply of water on agricultural production and irrigation water use in Southern California.
- Oikawa, P.Y., Gratz, D.A., Chatterjee, A., Eberwein, J.E., Allsman, L.A., Jenerette, G.D., 2014. Unifying soil respiration pulses, inhibition, and temperature hysteresis through dynamics of labile carbon and soil O<sub>2</sub>. *Journal of Geophysical Research: Biogeosciences*, 115: 521-536.

- Oikawa, P.Y., Jenerette, G.D., Grantz, D.A., 2015. Offsetting high water demands with high productivity: Sorghum as a biofuel crop in a high irradiance arid ecosystem. *GCB Bioenergy*, 7(5): 974-983.
- Parkes, S.D., McCabe, M.F., Griffiths, A.D., Wang, L., Chambers, S., Ershadi, A., Williams, A.G., Strauss, J., Element, A., 2016. Response of water vapour D-excess to land-atmosphere interactions in a semi-arid environment. *Hydrology and Earth System Sciences*.
- Reichstein, M., Falge, E., Baldocchi, D., Papale, D., Aubinet, M., Berbigier, P., Grünwald, T., 2005. On the separation of net ecosystem exchange into assimilation and ecosystem respiration: review and improved algorithm. *Global Change Biology*, 11(9): 1424-1439.
- Srayeddin, I., Doussan, C., 2009. Estimation of the spatial variability of root water uptake of maize and sorghum at the field scale by electrical resistivity tomography. *Plant Soil*, 319(1-2): 185-207.
- Stone, L.R., Goodrum, D.E., Jaafar, M.N., Khan, A.H., 2001. Rooting front and water depletion depths in grain sorghum and sunflower. *Agronomy Journal* 93(5): 1105-1110.
- Trenberth, K.E., Smith, L., Qian, T., Dai, A., Fasullo, J., 2007. Estimates of the global water budget and its annual cycle using observational and model data. *Journal of Hydrometeorology* 8: 758–769.

- Vörösmarty, C.J., Green, P., Salisbury, J., Lammers, R.B., 2000. Global water resources: vulnerability from climate change and population growth. *Science*, 289(5477): 284-288.
- Wada, Y., Wisser, D., Bierkens, M.F.P., 2014. Global modeling of withdrawal, allocation and consumptive use of surface water and groundwater resources. *Earth System Dynamics*, 5(1): 15-40.
- Wang, L., Caylor, K., Dragoni, D., 2009. On the calibration of continuous, high-precision  $\delta^{18}\text{O}$  and  $\delta^2\text{H}$  measurements using an off-axis integrated cavity output spectrometer *Rapid Communications in Mass Spectrometry*, 23: 530-536.
- Wang, L., Caylor, K.K., Villegas, J.C., Barron-Gafford, G.A., Breshears, D.D., Huxman, T.E., 2010. Evapotranspiration partitioning with woody plant cover: assessment of a stable isotope technique. *Geophysical Research Letters*, 37: L09401.
- Wang, L., D'Odorico, P., 2008. The limits of water pumps. *Science*, 321: 36-37.
- Wang, L., Good, S.P., Caylor, K.K., 2014. Global synthesis of vegetation control on evapotranspiration partitioning. *Geophysical Research Letters*, 41: 6753–6757.
- Wang, L., Good, S.P., Caylor, K.K., Cernusak, L.A., 2012. Direct quantification of leaf transpiration isotopic composition. *Agriculture and Forest Meteorology*, 154-155: 127-135.
- Wang, L., Niu, S., Good, S., Soderberg, K., Zhou, X., Xia, J., Sherry, R., Luo, Y., Caylor, K., McCabe, M., 2013. The effect of warming on grassland evapotranspiration

- partitioning using laser-based isotope monitoring techniques. *Geochimica et Cosmochimica Acta*, 111: 28-38.
- Wang, P., Yamanaka, T., Li, X.Y., Wei, Z., 2015. Partitioning evapotranspiration in a temperate grassland ecosystem: Numerical modeling with isotopic tracers. *Agriculture and Forest Meteorology*, 208: 16-31.
- Wilcox, B.P., Thurow, T.L., 2006. Emerging issues in rangeland ecohydrology: vegetation change and the water cycle. *Rangeland Ecology & Management*, 59: 220–224.
- Zhang, Y., Shen, Y., Sun, H., Gates, J.B., 2011. Evapotranspiration and its partitioning in an irrigated winter wheat field: A combined isotopic and micrometeorologic approach. *Journal of Hydrology*, 408(3): 203-211.
- Zhao, L., Wang, L., Liu, X., Xiao, H., Ruan, Y., Zhou, M., 2014. The patterns and implications of diurnal variations in the  $\delta$ -excess of plant water, shallow soil water and air moisture. *Hydrology and Earth System Sciences*, 18(10): 4129-4151.

## CHAPTER 6: CONCLUSIONS AND FUTURE WORK

### 6.1 Conclusions

This dissertation has filled some important knowledge gaps to understand and predict the climate change effects on hydrological cycles and soil-water-vegetation interactions in drylands. To address these knowledge gaps, I used some recent technical advances in terms of monitoring dryland water dynamics and vegetation water use, including remote sensing and stable isotopes. This dissertation has several important findings. The first part of this dissertation contributed to resolve a paradox in our intuitive understating of dryland greening. Results of the meta-analysis have supported a hypothesis that higher concentrations of atmospheric CO<sub>2</sub> induce plant water saving and that consequent available soil water increases are a likely driver of the observed greening phenomena. The study shows that an increase in atmospheric CO<sub>2</sub> to between 1.2 to 2.0 times the ambient CO<sub>2</sub> level has a positive effect on soil water content. A higher CO<sub>2</sub> levels results in an 11% increase in soil water content across all systems. Importantly, elevated CO<sub>2</sub> has significantly enhanced soil water levels in drylands than it has in non-drylands, with soil water content increasing by 9% in non-drylands compared to 17% in drylands. By identifying a new mechanism in global dryland greening, these findings provide important insights into plant-water interactions.

My hypothesis for greening mechanism is based on increasing atmospheric CO<sub>2</sub> inducing decreases in plant stomatal conductance ( $g_s$ ) and enhancing vegetation  $WUE$ , further work was conducted in the second part of this dissertation to evaluate three commonly used  $g_s$  models for their estimation of the stomatal response to environmental stimuli using *in-situ* measurements under different environmental conditions. This is the

first study to test these different  $g_s$  models under diverse conditions. The testing data were made under different environmental conditions, including the instantaneous measurements, semi-controlled measurements and the FACE experiments. The results show that Leuning's modified Ball-Berry model and RuBP limited optimization model generally provide good estimates of  $g_s$  for all the tested datasets. This finding supports the previous modeling analysis that has suggested RuBP regeneration limited model generally simulates more reasonable  $C_a$  response because the RuBP limited formulation could mimic a stomatal closure at rising  $C_a$  while the Rubisco limited formulation stimulates stomata to open at rising  $C_a$ . The variables such as functional groups (e.g.,  $C_3$  versus  $C_4$  species) and life form (e.g., annual versus perennial species) may play an important role in determining the stomatal response to changes in environmental factors, and therefore these variables need to be explicitly considered in the modeling framework.

Rainfall is another most critical factor determining the impact of climate change on the dynamics of water and vegetation in drylands. The third part of this dissertation has evaluated the feasibility of utilizing satellite-based rainfall estimates to examine the changes in rainfall patterns in data scarce dryland region. The TMPA rainfall estimates are used to assess the spatial variations and long-term rainfall variability from four locations across a rainfall gradient in Namibia. One of the most important findings from this study is the difference in trends of rainfall amount, frequency and intensity between drier and wetter regions. In a very arid and hot GRTC area, though the total rainfall amount does not change, there is a decrease (significant) in frequency ( $\lambda$ ) of storm accompanied by an increase (non-significant) in storm intensity ( $\alpha$ ). However, neither of these two indices

shows significant changes at Windhoek, a much wetter site. The Weltevrede Farm, as located in the transition zone from the dry Namib Desert to less arid highland (Windhoek), shows less significant results comparing to GRTC. The results also show increased rainfall variability for the driest location as indicated by the increases in coefficient of variation. The long-term rainfall pattern and late summer precipitation (FMA response) based on TMPA satellite derived rainfall dataset, are contrary to the IPCC predictions (with large uncertainties) of a drying trend in Namibia. The results have emphasized the spatial variability of dryland rainfall, as well as the necessity of obtaining ground observations in data scarce regions. This study provides a useful approach to help understand the temporal and spatial variations of precipitation in the areas of Africa where the *in situ* observations are scarce by using annual TMPA data to extend the data record with trend analysis.

Irrigation is the largest single consumer of fresh water on the planet. In the final part of this dissertation, I have presented a novel application to use the customized chambers and a laser-based isotope analyzer to directly quantify isotopic signatures of T, E and ET *in situ* and examine ET partitioning over a field of forage sorghum under an extreme environmental condition. An interesting pattern of plant water use for sorghum is observed, which implies that sorghum may use the lateral roots extracting water from the subsoil and redistribution to the surface layer, so both crop and surface soil evaporation would access water from deeper layers when the shallow water is depleted. Results also show for the studied ecosystem, approximately 46% of the irrigated water delivered to the crops is transpired, with 54% lost via direct evaporation from the soil during the vegetative



stage. Combining with the inherent irrigation inefficiencies, only 28 – 39% of the total source water is used by crops, therefore there could be a potential for improved water use efficiency.

## **6.2 Suggestions for Future Work**

The research that has been undertaken for this dissertation has highlighted a number of topics that would certainly merit further investigations.

The dryland greening has been a very interesting topic that presents something of a paradox in our intuitive understanding of plant-water-CO<sub>2</sub> interaction. A number of open issues are worth further investigations. For example, how long the observed trend of greening can last, and whether the greening would occur more preferably for C<sub>3</sub> or C<sub>4</sub> plant dominated systems? It is challenging to predict how an ecosystem will response to CO<sub>2</sub> enhancement since the indirect CO<sub>2</sub> feedback may lead to amplification or dampening of the direct leaf-level response to CO<sub>2</sub>. This idea was touched upon in our study, and led to the use of SEM approach to test the relative importance of direct versus indirect links between CO<sub>2</sub> enrichment and vegetation productivity. A further understanding of this complex feedback process is required. In addition, in the future work, it would be interesting to test the relative importance of regional drivers versus global driver (CO<sub>2</sub> enhancement) on vegetation greening. The time scale of the CO<sub>2</sub> enrichment effect may be the key in understanding these problems.

My current modeling framework has investigated how CO<sub>2</sub> changes can affect stomatal conductance, and linked the relative effect of a change in stomatal conductance

to the soil water status. It would be worthwhile to investigate if there is a possibility to link the changes of CO<sub>2</sub> to soil water status through stomatal conductance changes. Given the challenges in predicting the response of  $g_s$  in the mixed vegetation communities, it may require developing such models being species specific.

The result for the ET partitioning study shows that the isotopic signature is similar between E and T due to strong evaporative enrichment, which is rarely seen in the previous studies. My practical interest for the next step of this work would be to investigate the best management practices to control evaporation and improve the water use and water use efficiency in those harsh agricultural production systems.

**APPENDICES**

**Appendix A: Summary of soil water content data under CO<sub>2</sub> enhancement study**

Citation	Vegetation	Woody	System	Water	Soil Texture	Method	CO <sub>2</sub> enhancement ratio	Water content Amb_CO <sub>2</sub> (%)	Water content Elev_CO <sub>2</sub> (%)
Adair 2011	Grassland	Non-wood	natural	non-dryland	Sand	VSWC	1.5	9.28	9.72
Allard 2005	Grassland	Non-wood	natural	non-dryland	Sand	VSWC	1.3	17.83	17.93
Ambus 1999	Forest	Woody	natural	non-dryland	Sand	Others	2.0	10.55	12.1
Ambus 1999	Forest	Woody	natural	non-dryland	Sand	Others	2.0	29.03	30.8
Arnone III 1998	Grassland	Non-wood	natural	non-dryland	Loam	Others	1.7	34	37
Arnone III 1999	Grassland	Non-wood	natural	non-dryland	Loam	Others	1.7	25.6	29.5
Bader 2009	Forest	Woody	natural	non-dryland	Loam	VSWC	1.5	74.94	81.04
Baggs 2003	Grassland	Non-wood	natural	non-dryland	Loam	Others	1.7	28.66	31.22
Baggs 2004	Grassland	Non-wood	natural	non-dryland	Loam	Others	1.7	22.55	24.13
Burkart 2004	Cropland	Non-wood	managed	non-dryland	Sand	Others	1.7	9.39	9.57
Burkart 2004	Cropland	Non-wood	managed	non-dryland	Sand	Others	1.7	5.47	6.3
Carrillo 2011	Grassland	Non-wood	natural	Dryland	Loam	VSWC	1.7	12.23	14.63
Catovsky 1999	Forest	Woody	natural	non-dryland	No	Others	1.9	22.44	24.19
Conley 2001	Cropland	Non-wood	managed	non-dryland	loam	VSWC	1.5	20	18.68

Conley 2001	Cropland	Non-wood	managed	non-dryland	loam	VSWC	1.5	14.75	15.18
Craine 2001	Grassland	Non-wood	natural	non-dryland	Sand	Others	1.5	4.36	4.93
Decock 2012	Cropland	Non-wood	managed	non-dryland	Loam	Others	1.5	26.54	27.19
Deng 2010	Forest	Woody	natural	non-dryland	Loam	VSWC	1.9	23.48	25.52
Dijkstra 2010	Grassland	Non-wood	natural	Dryland	Loam	VSWC	1.5	14.75	15.4
Dijkstra 2013	Grassland	Non-wood	natural	Dryland	Loam	Others	1.5	14.47	16.91
Dubbs 2010	Forest	Woody	natural	non-dryland	Loam	VSWC	1.5	23.5	25.6
Edwards 2001	Grassland	Non-wood	natural	non-dryland	Sand	VSWC	1.3	20.4	20.32
Ellsworth 1999	Forest	Woody	natural	non-dryland	Loam	VSWC	1.5	19.75	22.34
Erbs 2009	Cropland	Non-wood	managed	non-dryland	Loam	VSWC	1.4	16.02	19.71
Erbs 2009	Cropland	Non-wood	managed	non-dryland	Loam	VSWC	1.4	25.81	29.05
Erbs 2009	Cropland	Non-wood	managed	non-dryland	Loam	VSWC	1.4	26.45	28.08
Fatichi 2013	Forest	Woody	natural	non-dryland	Loam	VSWC	1.6	34.14	40.54
Field 1997	Grassland	Non-wood	natural	Dryland	Sand	VSWC	2.0	16.47	19.51
Field 1997	Grassland	Non-wood	natural	Dryland	No	VSWC	2.0	19.25	20.29
Grunzweig 2001	Grassland	Non-wood	natural	Dryland	No	Others	1.6	5.4	6.18
Grunzweig 2001	Grassland	Non-wood	natural	Dryland	No	Others	1.4	6.18	6.35
Kettunen 2005	Cropland	Non-wood	managed	non-dryland	No	VSWC	2.0	45.48	47.9
Leakey 2006	Cropland	Non-wood	managed	non-dryland	Loam	VSWC	1.5	20.07	22.23

Lecain 2003	Grassland	Non-wood	natural	Dryland	Loam	VSWC	2.0	10.49	12.09
Lecain 2003	Grassland	Non-wood	natural	Dryland	Loam	VSWC	2.0	12.22	13.34
Lecain 2003	Grassland	Non-wood	natural	Dryland	Loam	VSWC	2.0	13.39	14.76
Lecain 2012	Grassland	Non-wood	natural	Dryland	Loam	VSWC	1.9	18.64	24.01
Lecain 2012	Grassland	Non-wood	natural	Dryland	Loam	VSWC	1.9	17.92	20.5
Leuzinger 2007	Forest	Woody	natural	non-dryland	Loam	VSWC	1.5	23.76	29.47
Leuzinger 2007	Forest	Woody	natural	non-dryland	Loam	VSWC	1.5	27.32	31.78
Liu 2008	Forest	Woody	natural	non-dryland	Loam	VSWC	1.9	22.82	23.12
Marthan 2010	Cropland	Non-wood	managed	non-dryland	Loam	VSWC	1.4	25.77	27.79
Matamala 2000	Forest	Woody	natural	non-dryland	Loam	VSWC	1.5	19.67	22.09
McCarthy 2010	Forest	Woody	natural	non-dryland	Loam	VSWC	1.5	23.6	24.94
McLain 2008	Forest	Woody	natural	non-dryland	Loam	VSWC	1.5	33.13	34.92
Morgan 2001	Grassland	Non-wood	natural	Dryland	Loam	VSWC	2.0	10.21	11.63
Morgan 2001	Grassland	Non-wood	natural	Dryland	Loam	VSWC	2.0	8.35	10.57
Mosier 2002	Grassland	Non-wood	natural	Dryland	Loam	VSWC	1.9	7.7	10.1
Nelson 2004	Grassland	Non-wood	natural	Dryland	Loam	VSWC	2.0	7.36	8.98
Nendel 2009	Cropland	Non-wood	managed	non-dryland	Sand	VSWC	1.5	58.6	69.7
Newton 2003	Grassland	Non-wood	natural	non-dryland	Sand	VSWC	1.3	17.88	18.02
Niklaus 1998	Grassland	Non-wood	natural	non-dryland	Loam	VSWC	1.7	23.2	25.7

Pataki 2000	Grassland	Non-wood	natural	Dryland	Sand	VSWC	1.9	5.99	7.73
Pendall 2003	Grassland	Non-wood	natural	Dryland	Loam	VSWC	2.0	8.38	10.92
Pregitzer 2006	Forest	Woody	natural	non-dryland	Loam	VSWC	1.5	21.31	22.74
Sindhoj 2000	Grassland	Non-wood	natural	non-dryland	Loam	VSWC	1.9	26.5	28.3
Volk 2000	Grassland	Non-wood	natural	non-dryland	Loam	Others	1.7	15.9	18.39
Wall 2001	Cropland	Non-wood	managed	non-dryland	loam	VSWC	1.5	14.54	15.06

### Appendix B: Summary of stomatal conductance data under environment different conditions

#### a. Instantaneous measurement data

Species	C <sub>3</sub> or C <sub>4</sub>	Annual or Perennial	Ca $\mu\text{mol mol}^{-1}$	D kpa	A $\mu\text{mol m}^{-2} \text{s}^{-1}$	g <sub>s</sub> $\text{mol m}^{-2} \text{s}^{-1}$
Wheat	C <sub>3</sub>	annual	207	2.1	9.68	0.263
Wheat	C <sub>3</sub>	annual	306	2.1	14.52	0.241
Wheat	C <sub>3</sub>	annual	404	2.1	16.02	0.161
Wheat	C <sub>3</sub>	annual	405	2.1	17.68	0.221
Wheat	C <sub>3</sub>	annual	511	2.1	20.09	0.210
Wheat	C <sub>3</sub>	annual	606	2.1	22.81	0.171
Wheat	C <sub>3</sub>	annual	709	2.1	24.91	0.161
Wheat	C <sub>3</sub>	annual	804	2.1	24.75	0.121

Wheat	C <sub>3</sub>	annual	911		2.1	25.95	0.111
Wheat	C <sub>3</sub>	annual	203		3.2	12.86	0.221
Wheat	C <sub>3</sub>	annual	298		3.2	16.75	0.201
Wheat	C <sub>3</sub>	annual	401		3.2	20.52	0.202
Wheat	C <sub>3</sub>	annual	497		3.2	22.28	0.220
Wheat	C <sub>3</sub>	annual	593		3.2	22.66	0.127
Wheat	C <sub>3</sub>	annual	700		3.2	25.80	0.139
Wheat	C <sub>3</sub>	annual	796		3.2	28.19	0.170
Wheat	C <sub>3</sub>	annual	895		3.2	27.68	0.168
Wheat	C <sub>3</sub>	annual	998		3.2	29.70	0.139
Wheat	C <sub>3</sub>	annual	205		2.6	14.20	0.298
Wheat	C <sub>3</sub>	annual	296		2.6	18.45	0.268
Wheat	C <sub>3</sub>	annual	399		2.6	22.27	0.254
Wheat	C <sub>3</sub>	annual	502		2.6	22.70	0.188
Wheat	C <sub>3</sub>	annual	605		2.6	24.96	0.165
Wheat	C <sub>3</sub>	annual	704		2.6	28.79	0.197
Wheat	C <sub>3</sub>	annual	807		2.6	28.22	0.131
Wheat	C <sub>3</sub>	annual	903		2.6	31.33	0.176
Wheat	C <sub>3</sub>	annual	297		2.0	19.33	0.322

Wheat	C <sub>3</sub>	annual	396	2.0	22.19	0.299
Wheat	C <sub>3</sub>	annual	400	2.0	23.48	0.252
Wheat	C <sub>3</sub>	annual	496	2.0	23.34	0.275
Wheat	C <sub>3</sub>	annual	595	2.0	25.20	0.165
Wheat	C <sub>3</sub>	annual	698	2.0	29.49	0.197
Wheat	C <sub>3</sub>	annual	798	2.0	31.35	0.184
Wheat	C <sub>3</sub>	annual	897	2.0	31.50	0.152

**b. Semi-controlled measurement data**

Species	C <sub>3</sub> or C <sub>4</sub>	Annual or Perennial	Ca μmol mol <sup>-1</sup>	D kpa	A μmol m <sup>-2</sup> s <sup>-1</sup>	g <sub>s</sub> mol m <sup>-2</sup> s <sup>-1</sup>
Rice	C <sub>3</sub>	annual	191	0.5	8.49	0.989
Rice	C <sub>3</sub>	annual	337	0.5	14.37	0.637
Rice	C <sub>3</sub>	annual	589	0.5	17.70	0.454
Rice	C <sub>3</sub>	annual	788	0.5	19.27	0.398
Rice	C <sub>3</sub>	annual	189	0.9	8.49	0.475
Rice	C <sub>3</sub>	annual	349	0.9	14.37	0.355
Rice	C <sub>3</sub>	annual	591	0.9	17.70	0.242
Rice	C <sub>3</sub>	annual	793	0.9	19.27	0.199



Rice	C <sub>3</sub>	annual	190	1.4	8.49	0.392
Rice	C <sub>3</sub>	annual	340	1.4	14.37	0.291
Rice	C <sub>3</sub>	annual	585	1.4	17.70	0.203
Rice	C <sub>3</sub>	annual	790	1.4	19.27	0.173
Rice	C <sub>3</sub>	annual	195	2	5.52	0.219
Rice	C <sub>3</sub>	annual	351	2	9.77	0.162
Rice	C <sub>3</sub>	annual	592	2	12.03	0.107
Rice	C <sub>3</sub>	annual	800	2	13.73	0.077
Phalaris	C <sub>3</sub>	perennial	179	0.5	8.15	1.806
Phalaris	C <sub>3</sub>	perennial	329	0.5	13.81	1.487
Phalaris	C <sub>3</sub>	perennial	572	0.5	16.82	0.899
Phalaris	C <sub>3</sub>	perennial	781	0.5	17.91	0.820
Phalaris	C <sub>3</sub>	perennial	184	0.9	8.15	0.830
Phalaris	C <sub>3</sub>	perennial	337	0.9	13.81	0.608
Phalaris	C <sub>3</sub>	perennial	579	0.9	16.82	0.376
Phalaris	C <sub>3</sub>	perennial	792	0.9	17.91	0.329
Phalaris	C <sub>3</sub>	perennial	190	1.4	8.15	0.546
Phalaris	C <sub>3</sub>	perennial	338	1.4	13.81	0.447
Phalaris	C <sub>3</sub>	perennial	577	1.4	16.82	0.330

Phalaris	C <sub>3</sub>	perennial	779	1.4	17.91	0.277
Phalaris	C <sub>3</sub>	perennial	188	2	6.26	0.391
Phalaris	C <sub>3</sub>	perennial	336	2	11.24	0.311
Phalaris	C <sub>3</sub>	perennial	584	2	13.99	0.208
Phalaris	C <sub>3</sub>	perennial	793	2	14.94	0.155
S. dimidiatum	C <sub>3</sub>	perennial	199	1	13.25	2.404
S. dimidiatum	C <sub>3</sub>	perennial	292	1	20.79	1.639
S. dimidiatum	C <sub>3</sub>	perennial	353	1	20.91	0.891
S. dimidiatum	C <sub>3</sub>	perennial	414	1	21.84	0.640
S. dimidiatum	C <sub>3</sub>	perennial	475	1	24.03	0.418
S. dimidiatum	C <sub>3</sub>	perennial	549	1	24.76	0.532
S. dimidiatum	C <sub>3</sub>	perennial	213	1	15.84	1.906
S. dimidiatum	C <sub>3</sub>	perennial	265	1	17.67	1.157
S. dimidiatum	C <sub>3</sub>	perennial	319	1	17.89	0.702
S. dimidiatum	C <sub>3</sub>	perennial	373	1	20.71	0.978
S. dimidiatum	C <sub>3</sub>	perennial	414	1	21.15	0.610
S. dimidiatum	C <sub>3</sub>	perennial	473	1	25.12	0.579
S. dimidiatum	C <sub>3</sub>	perennial	545	1	25.12	0.503
Br. japonicus	C <sub>3</sub>	annual	218	1	11.05	0.664

Br. japonicus	C <sub>3</sub>	annual	274	1	15.19	0.679
Br. japonicus	C <sub>3</sub>	annual	321	1	17.61	0.596
Br. japonicus	C <sub>3</sub>	annual	400	1	15.56	0.441
Br. japonicus	C <sub>3</sub>	annual	491	1	20.59	0.450
Br. japonicus	C <sub>3</sub>	annual	556	1	22.63	0.351
Br. japonicus	C <sub>3</sub>	annual	218	1.3	12.05	0.603
Br. japonicus	C <sub>3</sub>	annual	304	1.3	16.53	0.437
Br. japonicus	C <sub>3</sub>	annual	326	1.3	14.97	0.385
Br. japonicus	C <sub>3</sub>	annual	350	1.3	17.23	0.339
Br. japonicus	C <sub>3</sub>	annual	354	1.3	16.50	0.323
Br. japonicus	C <sub>3</sub>	annual	386	1.3	16.39	0.384
Br. japonicus	C <sub>3</sub>	annual	451	1.3	19.52	0.224
Br. japonicus	C <sub>3</sub>	annual	527	1.3	25.28	0.264
P. simithii	C <sub>3</sub>	perennial	100	0.45	1.84	0.606
P. simithii	C <sub>3</sub>	perennial	200	0.45	6.51	0.561
P. simithii	C <sub>3</sub>	perennial	360	0.45	13.13	0.501
P. simithii	C <sub>3</sub>	perennial	500	0.45	17.37	0.428
P. simithii	C <sub>3</sub>	perennial	720	0.45	21.84	0.342
P. simithii	C <sub>3</sub>	perennial	900	0.45	25.49	0.382

Maize	C <sub>4</sub>	annual	172	0.5	25.62	1.312
Maize	C <sub>4</sub>	annual	327	0.5	31.84	0.934
Maize	C <sub>4</sub>	annual	550	0.5	31.98	0.587
Maize	C <sub>4</sub>	annual	771	0.5	31.42	0.494
Maize	C <sub>4</sub>	annual	177	0.9	25.62	0.736
Maize	C <sub>4</sub>	annual	330	0.9	31.84	0.579
Maize	C <sub>4</sub>	annual	574	0.9	31.98	0.372
Maize	C <sub>4</sub>	annual	798	0.9	31.42	0.285
Maize	C <sub>4</sub>	annual	175	1.4	25.62	0.564
Maize	C <sub>4</sub>	annual	335	1.4	31.84	0.401
Maize	C <sub>4</sub>	annual	579	1.4	31.98	0.232
Maize	C <sub>4</sub>	annual	822	1.4	31.42	0.184
Maize	C <sub>4</sub>	annual	199	2	25.62	0.412
Maize	C <sub>4</sub>	annual	345	2	31.84	0.293
Maize	C <sub>4</sub>	annual	615	2	31.98	0.182
Maize	C <sub>4</sub>	annual	822	2	31.42	0.146
Paspalum	C <sub>4</sub>	perennial	172	0.5	20.91	1.987
Paspalum	C <sub>4</sub>	perennial	339	0.5	25.01	1.008
Paspalum	C <sub>4</sub>	perennial	583	0.5	25.09	0.787

Paspalum	C <sub>4</sub>	perennial	791	0.5	24.19	0.680
Paspalum	C <sub>4</sub>	perennial	175	0.9	20.91	0.875
Paspalum	C <sub>4</sub>	perennial	335	0.9	25.01	0.652
Paspalum	C <sub>4</sub>	perennial	575	0.9	25.09	0.469
Paspalum	C <sub>4</sub>	perennial	795	0.9	24.19	0.432
Paspalum	C <sub>4</sub>	perennial	180	1.4	20.91	0.589
Paspalum	C <sub>4</sub>	perennial	336	1.4	25.01	0.404
Paspalum	C <sub>4</sub>	perennial	579	1.4	25.09	0.291
Paspalum	C <sub>4</sub>	perennial	790	1.4	24.19	0.260
Paspalum	C <sub>4</sub>	perennial	184	2	20.91	0.437
Paspalum	C <sub>4</sub>	perennial	333	2	25.01	0.327
Paspalum	C <sub>4</sub>	perennial	586	2	25.09	0.222
Paspalum	C <sub>4</sub>	perennial	800	2	24.19	0.184
Bo. ischaemum	C <sub>4</sub>	perennial	200	1.5	8.44	0.158
Bo. ischaemum	C <sub>4</sub>	perennial	270	1.5	12.07	0.144
Bo. ischaemum	C <sub>4</sub>	perennial	300	1.5	14.03	0.149
Bo. ischaemum	C <sub>4</sub>	perennial	340	1.5	15.97	0.135
Bo. ischaemum	C <sub>4</sub>	perennial	381	1.5	16.21	0.130
Bo. ischaemum	C <sub>4</sub>	perennial	460	1.5	16.58	0.106

Bo. ischaemum	C <sub>4</sub>	perennial	553	1.5	20.55	0.102
Bo. ischaemum	C <sub>4</sub>	perennial	214	1.5	19.53	0.277
Bo. ischaemum	C <sub>4</sub>	perennial	268	1.5	18.39	0.235
Bo. ischaemum	C <sub>4</sub>	perennial	320	1.5	20.96	0.214
Bo. ischaemum	C <sub>4</sub>	perennial	399	1.5	25.49	0.195
Bo. ischaemum	C <sub>4</sub>	perennial	479	1.5	23.78	0.160
Bo. ischaemum	C <sub>4</sub>	perennial	538	1.5	28.42	0.152

**c. FACE measurement data**

Citation	Species	C <sub>3</sub> or C <sub>4</sub>	Annual or Perennial	Functional Group	Ca $\mu\text{mol mol}^{-1}$	A $\mu\text{mol m}^{-2} \text{s}^{-1}$	g <sub>s</sub> $\text{mol m}^{-2} \text{s}^{-1}$
Bernacchi_2006	Soybean	C <sub>3</sub>	annual	crops	375	23.69	0.562
Bernacchi_2006	Soybean	C <sub>3</sub>	annual	crops	550	29.97	0.396
Bhattacharya_1994	Cotton	C <sub>3</sub>	annual	crops	370		1.175
Bhattacharya_1994	Cotton	C <sub>3</sub>	annual	crops	550		0.863
Borjigidi_2006	Rice	C <sub>3</sub>	annual	crops	370	22.75	0.296
Borjigidi_2006	Rice	C <sub>3</sub>	annual	crops	570	27.63	0.254
Chen 2005	rice	C <sub>3</sub>	annual	crops	380	25.45	0.567
Chen 2005	rice	C <sub>3</sub>	annual	crops	580	30.36	0.439

Garcia_1998	Spring wheat	C <sub>3</sub>	annual	crops	370	21.19	0.525
Garcia_1998	Spring wheat	C <sub>3</sub>	annual	crops	550	27.00	0.371
Hileman_1992	cotton	C <sub>3</sub>	annual	crops	350	20.10	2.150
Hileman_1992	cotton	C <sub>3</sub>	annual	crops	550	20.40	2.160
Hileman_1992	cotton	C <sub>3</sub>	annual	crops	350	24.50	1.620
Hileman_1992	cotton	C <sub>3</sub>	annual	crops	600	32.50	1.600
Hileman_1994	cotton	C <sub>3</sub>	annual	crops	370	30.37	0.770
Hileman_1994	cotton	C <sub>3</sub>	annual	crops	550	38.97	0.614
Lee 2001	Legumes	C <sub>3</sub>	both	crops	368	16.10	0.340
Lee 2001	Legumes	C <sub>3</sub>	both	crops	560	17.33	0.261
Pozo 2005	Spring wheat	C <sub>3</sub>	annual	crops	376	36.7	0.317
Pozo 2005	Spring wheat	C <sub>3</sub>	annual	crops	757	28.6	0.196
Wall 2000	spring wheat	C <sub>3</sub>	annual	crops	370	15.92	0.342
Wall 2000	spring wheat	C <sub>3</sub>	annual	crops	570	19.77	0.187
Wall 2006	Spring wheat	C <sub>3</sub>	annual	crops	370	19.45	0.395
Wall 2006	Spring wheat	C <sub>3</sub>	annual	crops	550	24.45	0.265
Wechsung_2000	spring wheat	C <sub>3</sub>	annual	crops	370	7.65	0.212
Wechsung_2000	spring wheat	C <sub>3</sub>	annual	crops	550	8.76	0.180
Ainsworth_2003	Trifolium repens L.	C <sub>3</sub>	perennial	herbaceous	360	19.66	0.332

Ainsworth_2003	Trifolium repens L.	C <sub>3</sub>	perennial	herbaceous	600	27.39	0.248
Lee 2001	Forbs	C <sub>3</sub>	both	herbaceous	368	11.78	0.262
Lee 2001	Forbs	C <sub>3</sub>	both	herbaceous	560	13.08	0.209
Bryant_1998	A. vulneraria	C <sub>3</sub>	perennial	grass	355	10.45	0.408
Bryant_1998	A. vulneraria	C <sub>3</sub>	perennial	grass	600	16.35	0.322
Bryant_1998	S. minor	C <sub>3</sub>	perennial	grass	355	10.64	0.490
Bryant_1998	S. minor	C <sub>3</sub>	perennial	grass	600	16.3	0.527
Bryant_1998	B. erecta	C <sub>3</sub>	perennial	grass	355	10.74	0.373
Bryant_1998	B. erecta	C <sub>3</sub>	perennial	grass	600	19.95	0.275
Morgan_2001	Pascopyrum smithii	C <sub>3</sub>	perennial	grass	360	13.76	0.324
Morgan_2001	Pascopyrum smithii	C <sub>3</sub>	perennial	grass	720	17.21	0.225
Nijs 1997	Lolium perenne L.	C <sub>3</sub>	perennial	grass	350		0.412
Nijs 1997	Lolium perenne L.	C <sub>3</sub>	perennial	grass	600		0.319
Niklaus 1998	Bromus erectus	C <sub>3</sub>	perennial	grass	360		0.318
Niklaus 1998	Bromus erectus	C <sub>3</sub>	perennial	grass	600		0.149
Huxman 2001	Bromus	C <sub>3</sub>	annual	grass	350	6.72	0.173
Huxman 2001	Bromus	C <sub>3</sub>	annual	grass	550	11.40	0.142
Lee 2001	grass	C <sub>3</sub>	both	grass	368	9.94	0.238
Lee 2001	grass	C <sub>3</sub>	both	grass	560	11.60	0.179



Hamerlyncck_2000	Larrea tridentata	C <sub>3</sub>	perennial	shrub	360	4.79	0.065
Hamerlyncck_2000	Larrea tridentata	C <sub>3</sub>	perennial	shrub	550	8.81	0.064
Hamerlyncck_2002	Lycium andersonii	C <sub>3</sub>	perennial	shrub	360	14.18	0.364
Hamerlyncck_2002	Lycium andersonii	C <sub>3</sub>	perennial	shrub	550	13.66	0.266
Naumburg 2003	Larrea tridentata	C <sub>3</sub>	perennial	shrub	360	2.17	0.049
Naumburg 2003	Larrea tridentata	C <sub>3</sub>	perennial	shrub	550	2.77	0.037
Naumburg 2003	Krameria erecta	C <sub>3</sub>	perennial	shrub	360	2.00	0.062
Naumburg 2003	Krameria erecta	C <sub>3</sub>	perennial	shrub	550	3.42	0.066
Naumburg 2003	Ambrosia dumosa	C <sub>3</sub>	perennial	shrub	360	3.95	0.166
Naumburg 2003	Ambrosia dumosa	C <sub>3</sub>	perennial	shrub	550	6.00	0.131
Pataki 2000	Larrea tridentata	C <sub>3</sub>	perennial	shrub	360		0.081
Pataki 2000	Larrea tridentata	C <sub>3</sub>	perennial	shrub	550		0.071
Pataki 2000	Larrea tridentata	C <sub>3</sub>	perennial	shrub	700		0.069
Bernacchi_2003	P. alba	C <sub>3</sub>	perennial	tree	370	18.16	0.372
Bernacchi_2003	P. alba	C <sub>3</sub>	perennial	tree	550	24.51	0.363
Bernacchi_2003	P. nigra	C <sub>3</sub>	perennial	tree	370	18.94	0.420
Bernacchi_2003	P. nigra	C <sub>3</sub>	perennial	tree	550	25.74	0.369
Bernacchi_2003	P. eura	C <sub>3</sub>	perennial	tree	370	20.65	0.494
Bernacchi_2003	P. eura	C <sub>3</sub>	perennial	tree	550	26.00	0.510

Calfapietra_2005	poplar	C <sub>3</sub>	perennial	tree	400	13.95	0.569
Calfapietra_2005	poplar	C <sub>3</sub>	perennial	tree	600	21.45	0.441
Catovsky_1999	birch	C <sub>3</sub>	perennial	tree	375	8.92	0.295
Catovsky_1999	birch	C <sub>3</sub>	perennial	tree	700	13.48	0.185
Ellsworth_1995	Pinus taeda	C <sub>3</sub>	annual	tree	360	11.30	0.117
Ellsworth_1995	Pinus taeda	C <sub>3</sub>	annual	tree	560	13.80	0.116
Ellsworth_1999	Pinus taeda	C <sub>3</sub>	annual	tree	350	5.67	0.069
Ellsworth_1999	Pinus taeda	C <sub>3</sub>	annual	tree	550	8.49	0.061
Fatichi_2013	fagus sylvatica	C <sub>3</sub>	annual	tree	370		0.120
Fatichi_2013	fagus sylvatica	C <sub>3</sub>	annual	tree	550		0.095
Gunderson_2002	sweetgum	C <sub>3</sub>	perennial	tree	360	9.95	0.210
Gunderson_2002	sweetgum	C <sub>3</sub>	perennial	tree	560	14.50	0.165
Herrick_2003	sweetgum	C <sub>3</sub>	perennial	tree	376		0.253
Herrick_2003	sweetgum	C <sub>3</sub>	perennial	tree	572		0.185
Herrick_2004	sweetgum	C <sub>3</sub>	perennial	tree	379	4.76	0.117
Herrick_2004	sweetgum	C <sub>3</sub>	perennial	tree	574	7.66	0.115
Naumburg_2000	pinus taeda L.	C <sub>3</sub>	perennial	tree	365	5.91	0.100
Naumburg_2000	pinus taeda L.	C <sub>3</sub>	perennial	tree	565	9.18	0.094
Noormets_2001	Aspen	C <sub>3</sub>	perennial	tree	360	15.53	0.394

Noormets 2001	Aspen	C <sub>3</sub>	perennial	tree	560	22.18	0.310
Singsaas 2000	3 tree spp	C <sub>3</sub>	perennial	tree	360		0.049
Singsaas 2000	3 tree spp	C <sub>3</sub>	perennial	tree	560		0.048
Tricker 2005	P. euramericana	C <sub>3</sub>	perennial	tree	360	8.63	0.321
Tricker 2005	P. euramericana	C <sub>3</sub>	perennial	tree	550	11.44	0.179
Wullschleger_2002	sweetgum	C <sub>3</sub>	perennial	tree	394		0.242
Wullschleger_2002	sweetgum	C <sub>3</sub>	perennial	tree	538		0.177
McElrone 2005	Acer rubrum	C <sub>3</sub>	perennial	tree	360		0.071
McElrone 2005	Acer rubrum	C <sub>3</sub>	perennial	tree	560		0.051
Leakey 2004	Maize	C <sub>4</sub>	annual	crops	370	29.40	0.209
Leakey 2004	Maize	C <sub>4</sub>	annual	crops	550	35.00	0.163
Wall 2001	sorghum	C <sub>4</sub>	annual	crops	370	32.80	0.480
Wall 2001	sorghum	C <sub>4</sub>	annual	crops	570	37.57	0.310
Leakey 2006	Maize	C <sub>4</sub>	annual	crops	370	30.18	0.248
Leakey 2006	Maize	C <sub>4</sub>	annual	crops	550	30.48	0.164
Huxman 2001	Eriogonum inflatum	C <sub>4</sub>	perennial	herbaceous	350	16.93	0.610
Huxman 2001	Eriogonum inflatum	C <sub>4</sub>	perennial	herbaceous	550	18.43	0.423
Knapp_1993	Andropogon gerardii	C <sub>4</sub>	perennial	grass	350	19.39	0.202

Knapp_1993	Andropogon gerardii	C <sub>4</sub>	perennial	grass	700	19.97	0.102
Lee 2001	grass	C <sub>4</sub>	both	grass	368	16.07	0.170
Lee 2001	grass	C <sub>4</sub>	both	grass	560	15.86	0.126
Morgan_2001	Bouteloua gracilis	C <sub>4</sub>	perennial	grass	360	15.71	0.233
Morgan_2001	Bouteloua gracilis	C <sub>4</sub>	perennial	grass	720	20.15	0.166
Pearson 1995	R. obtusifolius	C <sub>4</sub>	perennial	weed	350	12.0	0.200
Pearson 1995	R. obtusifolius	C <sub>4</sub>	perennial	weed	600	19.0	0.150
Knapp_1996	10 grass spp	mix	both	grass	330		0.239
Knapp_1996	10 grass spp	mix	both	grass	660		0.196

## Appendix C: Stomatal conductance and soil water model framework

In Gao's water-limited conductance sub-model, the relation between soil water potential  $\psi_s$  and stomatal conductance  $g_s$  can be expressed as:

$$g_s = \frac{g_{0m} + k_\psi \psi_s + k_{\alpha\beta} I_p}{1 + k_{\beta g} d_{vp}}, \quad (1)$$

where  $g_{0m}$  is the maximum residual stomatal conductance at saturated soil conditions,  $I_p$  is photosynthetic active radiation (PAR), and  $k_\psi$ ,  $k_{\alpha\beta}$ , and  $k_{\beta g}$  are model-specific parameters,  $d_{vp}$  is  $D$  normalized by atmospheric pressure.

By re-arranging the equation (1), it can find that

$$\psi_s = \frac{g_s (1 + k_{\beta g} d_{vp}) - g_{0m} - k_{\alpha\beta} I_p}{k_\psi}, \quad (2)$$

In the next step, by taking derivatives, the relative effect of a change in  $g_s$  on  $\psi_s$  is given by

$$\frac{d\psi_s}{\psi_s} = \frac{1}{k_\psi} \frac{dg_s}{g_s} + \frac{k_{\beta g}}{k_\psi} \left( \frac{dg_s}{g_s} + \frac{dD_v}{D_v} \right) - \frac{k_{\alpha\beta}}{k_\psi} \frac{dI_p}{I_p}, \quad (3)$$

Next, it can find some relation between  $g_s$  and  $D_v$ , and  $g_s$  and  $I_p$ . The dependence of  $g_s$  on  $D_v$  can be observed and modeled by taking  $\frac{dg_s}{g_s}$  as being proportional to  $\frac{dD_v^{-0.5}}{D_v^{-0.5}}$ . Similarly, the relation between  $g_s$  and  $I_p$  can be approximated by a hyperbola with a form  $f(I_p) = 1/(1 + \frac{\beta}{I_p})$ , where  $\beta$  is model specific parameter, so the changes in  $I_p$  can be modeled by taking  $\frac{dg_s}{g_s}$  as being proportional to  $\frac{d(1+\beta/I_p)^{-1}}{(1+\beta/I_p)^{-1}}$ . With these two approximations, equation (3) becomes:

$$\frac{d\psi_s}{\psi_s} = \frac{dg_s}{g_s} \left( \frac{1}{k_\psi} - \frac{k_{\beta g}}{101.3 \times k_\psi} - \frac{k_{\alpha\beta}}{k_\psi} \right), \quad (4)$$

The soil water potential is then converted to the volumetric water content using water retention curves generated from pressure plate analysis in soil cores, and it follows an exponential relationship:

$$\psi_s = k \times \theta^{-a}, \quad (5)$$

where  $a$  is a model specific parameter related to soil type. So the relation between soil water potential and water content can be modeled by taking  $\frac{d\psi_s}{\psi_s}$  as being proportional to  $\frac{d(\theta)^{-a}}{(\theta)^{-a}}$ .

By combining this approximation with equation (4), we can find that

$$\frac{d\theta}{\theta} = \frac{\left( -\frac{1}{k_\psi} + \frac{k_{\beta g}}{101.3 \times k_\psi} + \frac{k_{\alpha\beta}}{k_\psi} \right) dg_s}{k \times a} \frac{dg_s}{g_s}, \quad (6)$$

where  $k_\psi$ ,  $k_{\alpha\beta}$ ,  $k_{\beta g}$ ,  $\beta$  and  $a$  are model-specific parameters.

**Appendix D: TMPA satellite rainfall estimates for the 4 locations across a rainfall gradient in Namibia**

**a. Annual rainfall P, average rain depth per storm  $\alpha$ , and the average storm arrival rate  $\lambda$  for Weltevrede Farm 1**

Year	Days	Total P (mm)	# of storm	P frequency (day)	$\lambda$ (day <sup>-1</sup> )	$\alpha$ (mm)
1998	365	52.53	24	15.2	0.066	2.19
1999	365	149.10	41	8.9	0.112	3.64
2000	366	200.08	20	18.3	0.055	10.00
2001	365	166.15	27	13.5	0.074	6.15
2002	365	165.95	42	8.7	0.115	3.95
2003	365	112.56	29	12.6	0.079	3.88
2004	366	116.36	31	11.8	0.085	3.75
2005	365	106.99	31	11.8	0.085	3.45
2006	365	357.03	50	7.3	0.137	7.14
2007	365	86.32	16	22.8	0.044	5.40
2008	366	394.45	44	8.3	0.120	8.96
2009	365	255.01	35	10.4	0.096	7.29
2010	365	76.10	18	20.3	0.049	4.23
2011	365	327.88	53	6.9	0.145	6.19
2012	366	98.29	28	13.1	0.077	3.51

2013	365	108.40	21	17.4	0.058	5.16
2014	365	119.69	20	18.3	0.055	5.98
2015	365	56.31	20	18.3	0.055	2.82

**b. Seasonal rainfall P, average rain depth per storm  $\alpha$ , and the average storm arrival rate  $\lambda$  for Weltevrede Farm 1**

Year	Days	Total P (mm)	# of storm	P frequency (day)	$\lambda$ (day <sup>-1</sup> )	$\alpha$ (mm)
1998-1999	212	121.44	25	8.5	0.118	4.86
1999-2000	213	214.90	24	8.9	0.113	8.95
2000-2001	212	142.04	15	14.1	0.071	9.47
2001-2002	212	158.03	28	7.6	0.132	5.64
2002-2003	212	102.91	22	9.6	0.104	4.68
2003-2004	213	63.44	14	15.2	0.066	4.53
2004-2005	212	156.88	27	7.9	0.127	5.81
2005-2006	212	336.39	34	6.2	0.160	9.89
2006-2007	212	106.45	23	9.2	0.108	4.63
2007-2008	213	287.94	35	6.1	0.164	8.23
2008-2009	212	356.90	37	5.7	0.175	9.65
2009-2010	212	55.58	16	13.3	0.075	3.47



2010-2011	212	283.86	48	4.4	0.226	5.91
2011-2012	213	95.40	19	11.2	0.089	5.02
2012-2013	212	67.61	15	14.1	0.071	4.51
2013-2014	212	146.43	21	10.1	0.099	6.97
2014-2015	212	34.70	11	19.3	0.052	3.15

**c. Annual rainfall P, average rain depth per storm  $\alpha$ , and the average storm arrival rate  $\lambda$  for Weltevrede Farm 2**

Year	Days	Total P (mm)	# of storm	P frequency (day)	$\lambda$ (day <sup>-1</sup> )	$\alpha$ (mm)
1998	365	34.21	15	24.3	0.041	2.28
1999	365	216.83	39	9.4	0.107	5.56
2000	366	281.07	26	14.1	0.071	10.81
2001	365	187.28	29	12.6	0.079	6.46
2002	365	189.82	45	8.1	0.123	4.22
2003	365	144.55	35	10.4	0.096	4.13
2004	366	242.87	30	12.2	0.082	8.10
2005	365	171.81	29	12.6	0.079	5.92
2006	365	484.86	59	6.2	0.162	8.22
2007	365	73.09	19	19.2	0.052	3.85

2008	366	473.47	68	5.4	0.186	6.96
2009	365	352.36	48	7.6	0.132	7.34
2010	365	138.96	37	9.9	0.101	3.76
2011	365	370.12	76	4.8	0.208	4.87
2012	366	169.67	40	9.2	0.109	4.24
2013	365	166.76	32	11.4	0.088	5.21
2014	365	175.49	31	11.8	0.1	5.7
2015	365	93.07	28	13.0	0.1	3.3

**d. Seasonal rainfall P, average rain depth per storm  $\alpha$ , and the average storm arrival rate  $\lambda$  for Weltevrede Farm 2**

Year	Days	Total P (mm)	# of storm	P frequency (day)	$\lambda$ (day <sup>-1</sup> )	$\alpha$ (mm)
1998-1999	212	142.77	27	7.9	0.127	5.29
1999-2000	213	336.69	30	7.1	0.141	11.22
2000-2001	212	170.96	22	9.6	0.104	7.77
2001-2002	212	183.52	37	5.7	0.175	4.96
2002-2003	212	129.33	29	7.3	0.137	4.46
2003-2004	213	182.08	25	8.5	0.117	7.28
2004-2005	212	223.08	28	7.6	0.132	7.97

2005-2006	212	468.65	51	4.2	0.241	9.19
2006-2007	212	106.80	24	8.8	0.113	4.45
2007-2008	213	364.34	55	3.9	0.258	6.62
2008-2009	212	444.13	54	3.9	0.255	8.22
2009-2010	212	120.36	33	6.4	0.156	3.65
2010-2011	212	363.16	69	3.1	0.325	5.26
2011-2012	213	164.07	35	6.1	0.164	4.69
2012-2013	212	95.34	22	9.6	0.104	4.33
2013-2014	212	214.14	35	6.1	0.165	6.12
2014-2015	212	67.04	19	11.16	0.09	3.53

e. Annual rainfall P, average rain depth per storm  $\alpha$ , and the average storm arrival rate  $\lambda$  for GRTC

Year	Days	Total P (mm)	# of storm	P frequency (day)	$\lambda$ (day <sup>-1</sup> )	$\alpha$ (mm)
1998	365	30.93	25	14.6	0.068	1.24
1999	365	60.53	36	10.1	0.099	1.68
2000	366	43.80	28	13.1	0.077	1.56
2001	365	46.63	25	14.6	0.068	1.87
2002	365	62.35	31	11.8	0.085	2.01

2003	365	39.92	26	14.0	0.071	1.54
2004	366	67.02	41	8.9	0.112	1.63
2005	365	40.11	33	11.1	0.090	1.22
2006	365	138.46	32	11.4	0.088	4.33
2007	365	16.56	12	30.4	0.033	1.38
2008	366	92.23	33	11.1	0.090	2.79
2009	365	38.77	24	15.2	0.066	1.62
2010	365	17.38	13	28.1	0.036	1.34
2011	365	145.78	25	14.6	0.068	5.83
2012	366	15.26	10	36.6	0.027	1.53
2013	365	41.38	7	52.1	0.019	5.91
2014	365	13.90	10	36.5	0.027	1.39
2015	365	14.20	8	45.6	0.022	1.77

f. Seasonal rainfall P, average rain depth per storm  $\alpha$ , and the average storm arrival rate  $\lambda$  for GRTC

Year	Days	Total P (mm)	# of storm	P frequency (day)	$\lambda$ (day <sup>-1</sup> )	$\alpha$ (mm)
1998-1999	212	47.95	20	10.6	0.094	2.40
1999-2000	213	46.73	19	11.2	0.089	2.46

2000-2001	212	38.22	17	12.5	0.080	2.25
2001-2002	212	54.18	15	14.1	0.071	3.61
2002-2003	212	38.41	17	12.5	0.080	2.26
2003-2004	213	27.45	13	16.4	0.061	2.11
2004-2005	212	62.42	25	8.5	0.118	2.50
2005-2006	212	130.61	18	11.8	0.085	7.26
2006-2007	212	20.90	13	16.3	0.061	1.61
2007-2008	213	70.92	15	14.2	0.070	4.73
2008-2009	212	53.39	19	11.2	0.090	2.81
2009-2010	212	2.78	8	26.5	0.038	0.35
2010-2011	212	134.30	24	8.8	0.113	5.60
2011-2012	213	13.46	7	30.4	0.033	1.92
2012-2013	212	23.41	6	35.3	0.028	3.90
2013-2014	212	14.48	6	35.3	0.028	2.41
2014-2015	212	5.06	4	53.0	0.019	1.26
1998-1999	212	47.95	20	10.6	0.094	2.40

**g. Annual rainfall  $P$ , average rain depth per storm  $\alpha$ , and the average storm arrival rate  $\lambda$  for WDH**

Year	Days	Total P (mm)	# of storm	P frequency (day)	$\lambda$ (day <sup>-1</sup> )	$\alpha$ (mm)
1998	365	203.38	121	3.0	0.332	1.68
1999	365	424.86	164	2.2	0.449	2.59
2000	366	540.65	189	1.9	0.516	2.86
2001	365	442.78	209	1.7	0.573	2.12
2002	365	343.07	195	1.9	0.534	1.76
2003	365	326.64	181	2.0	0.496	1.80
2004	366	555.93	236	1.6	0.645	2.36
2005	365	385.78	240	1.5	0.658	1.61
2006	365	781.52	228	1.6	0.625	3.43
2007	365	228.37	206	1.8	0.564	1.11
2008	366	624.70	236	1.6	0.645	2.65
2009	365	433.32	249	1.5	0.682	1.74
2010	365	351.13	200	1.8	0.548	1.76
2011	365	791.72	181	2.0	0.496	4.37
2012	366	396.45	168	2.2	0.459	2.36
2013	365	301.11	150	2.4	0.411	2.01
2014	365	480.63	184	1.98	0.504	2.61

2015	365	274.21	125	2.92	0.342	2.19
------	-----	--------	-----	------	-------	------

**h. Seasonal rainfall P, average rain depth per storm  $\alpha$ , and the average storm arrival rate  $\lambda$  for WDH**

Year	Days	Total P (mm)	# of storm	P frequency (day)	$\lambda$ (day <sup>-1</sup> )	$\alpha$ (mm)
1998-1999	212	295.06	105	2.0	0.495	2.81
1999-2000	213	646.25	134	1.6	0.629	4.82
2000-2001	212	436.63	149	1.4	0.703	2.93
2001-2002	212	323.89	154	1.4	0.726	2.10
2002-2003	212	265.29	156	1.4	0.736	1.70
2003-2004	213	488.83	142	1.5	0.667	3.44
2004-2005	212	464.14	174	1.2	0.821	2.67
2005-2006	212	727.09	157	1.4	0.741	4.63
2006-2007	212	286.37	192	1.1	0.906	1.49
2007-2008	213	514.85	153	1.4	0.718	3.37
2008-2009	212	517.73	185	1.1	0.873	2.80
2009-2010	212	282.96	174	1.2	0.821	1.63
2010-2011	212	824.23	164	1.3	0.774	5.03
2011-2012	213	383.50	138	1.5	0.648	2.78

2012-2013	212	170.24	130	1.6	0.613	1.31
2013-2014	212	597.00	148	1.4	0.698	4.03
2014-2015	212	234.54	158	1.3	0.745	1.48

**Appendix E: Deuterium and oxygen isotope signatures for transpiration ( $T$ ), evaporation ( $E$ ) and evapotranspiration ( $ET$ ) over 3 irrigation cycles for Sorghum bicolor at the University of California's Desert Research and Extension Center (DREC)**

**a. Oxygen isotope data**

Date	$\delta_T$ (‰)	$\delta_E$ (‰)	$\delta_{ET}$ (‰)	std ( $\delta_T$ ) (‰)	std ( $\delta_E$ ) (‰)	std ( $\delta_{ET}$ ) (‰)
7/24/14	-0.5	-2.8	-3.0	2.0	1.1	2.2
7/26/14	2.5	3.1	3.6	2.5	1.2	1.4
7/28/14	-2.0	-0.2	1.3	2.0	2.3	2.3
7/30/14	-4.0	-1.0	1.9	3.8	2.4	1.0
8/4/14	-6.1	-4.5	0.2	3.7	0.2	2.8
8/6/14	1.5	-4.4	2.7	1.3	1.1	3.0
8/7/14	0.1	-5.0	-0.1	5.4	1.5	6.2
8/13/14	1.0	0.6		1.8	1.1	
8/18/14	7.0	5.1		2.5	2.0	



8/20/14	0.9	-4.5	1.1	1.3
---------	-----	------	-----	-----

**b. Deuterium isotope data**

Date	$\delta_T$ (‰)	$\delta_E$ (‰)	$\delta_{ET}$ (‰)	std ( $\delta_T$ ) (‰)	std ( $\delta_E$ ) (‰)	std ( $\delta_{ET}$ ) (‰)
7/24/14	-86.6	-97.3	-93.7	3.4	4.8	2.0
7/26/14	-70.4	-71.1	-73.7	9.8	3.2	1.6
7/28/14	-82.9	-86.1	-83.6	3.6	3.7	2.9
7/30/14	-89.8	-84.0	-88.1	4.2	4.4	3.3
8/4/14	-88.1	-81.9	-82.3	6.7	2.6	2.9
8/6/14	-86.9	-71.7	-81.0	3.6	0.9	2.0
8/7/14	-89.3	-91.7	-86.7	9.3	1.1	4.0
8/13/14	-88.7	-86.7		4.7	2.4	
8/18/14	-71.8	-72.8		2.9	0.8	
8/20/14	-78.1	-79.7		1.2	5.7	

# CURRICULUM VITAE

Xuefei Lu

## Education:

- *Ph.D.* in Applied Earth Sciences, **Indiana University Purdue University – Indianapolis (IUPUI)**, USA, 2018. Advisor: Dr. Lixin Wang
- *M.S.* in Environmental Engineering, **Michigan Technological University**, USA, 2003
- *M.E.* in Environmental Engineering, **Tongji University**, China, 2001
- *B.E.* in Polymer Engineering, **Nanjing University of Technology**, China, 1995

## Honors, Awards & Fellowship:

- University Fellowship, Indiana University, 2014-2015
- The President's Diversity Fellowship, Indiana University, Summer 2017

## Research Experience:

- *Research Assistant*, Department of Earth Sciences, IUPUI, Indianapolis, USA  
May 2013 – May 2017
- *Research Assistant*, Department of Civil and Environmental Engineering,  
Michigan Technological University, Houghton, USA  
August 2001 – December 2003

## Professional Experience:

- *Water Resources Engineer*, SCS Consulting Group Ltd., Markham, Canada,  
September 2010 - July 2011
- *Environmental/Water Resources Analyst*, Greenland International Consulting  
Inc., Caledon East, Canada  
February 2006 – December 2008

## Conference Presentations:

- A Multi-Scale Analysis of Namibian Rainfall: Comparing TRMM Satellite Data and Ground Observations. Poster session presented at AGU annual fall meeting, December 2014, San Francisco, CA

- Partitioning of Evapotranspiration Using a Stable Water Isotope Technique in a High Temperature Agricultural Production System. Poster session presented at AGU annual fall meeting, December 2015, San Francisco, CA

**Journal Publications:**

- **Lu, X.**, Liang, L.L., Wang, L., Jenerette, G.D., McCabe, M.F. and Grantz, D.A., 2017. Partitioning of evapotranspiration using a stable isotope technique in an arid and high temperature agricultural production system. *Agricultural Water Management*, 179: 103–109
- **Lu, X.**, Wang, L. and McCabe, M.F., 2016. Elevated CO<sub>2</sub> as a driver of global dryland greening. *Scientific Reports*, 6 Article number 20716
- **Lu, X.**, Wang, L., Pan, M., Kaseke, K.F. and Li, B., 2016. A multi-scale analysis of Namibian rainfall over the recent decade—comparing TMPA satellite estimates and ground observations. *Journal of Hydrology: Regional Studies*, 8, 59-68.
- Urban, N.R., Auer, M.T., Green, S.A., **Lu, X.**, Apul, D.S., Powell, K.D. and Bub, L., 2005. Carbon cycling in Lake Superior. *Journal of Geophysical Research: Oceans*, 110 article number C6
- Urban, N.R., **Lu, X.**, Chai, Y. and Apul, D.S., 2004. Sediment trap studies in Lake Superior: Insights into resuspension, cross-margin transport, and carbon cycling. *Journal of Great Lakes Research*, 30: 147-161